ABSTRACT

Title of dissertation: PHOTODETECTION USING ULTRATHIN METAL FILMS

Lisa J. Krayer
Doctor of Philosophy, 2019

Dissertation directed by: Professor Jeremy N. Munday
Department of Electrical Engineering

Silicon is the most widely used material for visible photodetection, with extensive applications in both consumer and industrial products. Further, its excellent optoelectronic properties and natural abundance have made it nearly ideal for microelectronic devices and solar cells. However, silicon's lack of absorption in the infrared limits its use in infrared detectors and imaging sensors, severely constraining its implementation in telecommunications for low–cost integrated optical circuitry. In this thesis, we show that this limitation can be overcome by exploiting resonant absorption in ultrathin metal films (< 20 nm). Our approach paves the way to implement scalable, lithography–free, and low–cost silicon–based optoelectronics beyond the material bandgap.

Light absorption in metal films can excite hot carriers, which are useful for photodetection, solar energy conversion, and many other applications. However, metals are highly reflective, and therefore, careful optical design is required to achieve high absorption in these films. Through appropriate optical design, we achieved a Fabry-Pérot–like resonance in ultrathin metal films deposited on a semiconductor enabling

$> 70\%$ light absorption below the bandgap of the semiconductor. We experimentally demonstrate this phenomenon with four ultrathin planar metal films: Pt, Fe, Cr, and Ti. These metals were chosen to satisfy the resonant condition for high absorption over a wide range of wavelengths, and with these designs we realize a near–infrared imaging detector.

In addition, we utilize an index–near–zero (INZ) substrate to further improve the absorption to near–unity. By employing aluminum–doped zinc oxide (AZO) as the INZ medium in the near–infrared range, we enhance the metal film absorption by nearly a factor of 2. To exploit this absorption enhancement in an optoelectronic device, we fabricate a Schottky photodiode with a Pt film on Si and find that the photocurrent generated in the photodiode is enhanced by $> 80\%$ with the INZ substrate. The enhancement arises from a combination of improved carrier generation and carrier transport resulting from the addition of the AZO film.

Finally, we explore the tunability of material properties through alloying metals. Alloying of metals provides a vast parameter space for tuning of material, chemical, and mechanical properties, impacting disciplines ranging from photonics and catalysis to aerospace. We demonstrate that AgAu alloys provide an ideal model system for controlling the optical and electrical responses in ultrathin metal films for hot carrier photodetectors with improved performance. While pure Ag and Au have long hot carrier attenuation lengths > 20 nm, their optical absorption is insufficient for high efficiency devices. We find that alloying Ag and Au enhances the absorption by $\sim 50\%$ while maintaining attenuation lengths > 15 nm, currently limited by grain boundary scattering. Further, our density functional theory anal-

ysis shows that the addition of small amounts of Au to the Ag lattice significantly enhances the hot hole generation rate.

PHOTODETECTION USING ULTRATHIN METAL FILMS

by

Lisa J. Krayer

Dissertation submitted to the Faculty of the Graduate School of the
University of Maryland, College Park in partial fulfillment
of the requirements for the degree of
Doctor of Philosophy
2019

Advisory Committee:
Professor Jeremy N. Munday, Chair/Advisor
Professor Neil Goldsman, Co-Chair
Professor Kevin Daniels
Professor Thomas E. Murphy
Professor Lourdes G. Salamanca-Riba

Dedication

To Dr. Dorothe M. Krayer for being part of the change that made this possible.

Acknowledgments

There are many people that I want to thank for both ensuring that I had the opportunity to complete this work and assisting me along the way.

First, I would like to thank Professor Jeremy Munday for allowing me to work on many interesting projects while providing mentorship and guidance. I would also like to thank all the members of Professor Munday's research lab, including Joseph Murray, Joseph Garrett, David Somers, Tao Gong, Kevin Palm, Jongbum Kim and Sarvenaz Memarzadeh, for all their help and camaraderie through the years. I also want to thank Professor Marina Leite and the members of her lab, specifically Chen Gong and Elizabeth Tennyson, for working with me on many of my research projects. I especially want to thank all the members of my committee for taking the time to read my thesis and attend my dissertation defense: Thomas Murphy, Neil Goldsman, Kevin Daniels, Lourdes Salamanca–Riba.

I owe a large debt of gratitude to Dr. Paige Smith for offering me a Graduate Assistantship with the Women in Engineering (WIE) program less than a month before I started the graduate program at UMD. Without her support, I would not be here, and I would not have had the opportunity to complete this thesis. In addition, I would like to thank all the WIE Program staff, including Tamara Fuller, Bria Barry, Candice Staples, Elizabeth Kurban and Greg Stinson. Their unending friendship and support made moving to Maryland truly enjoyable.

This research was only possible thanks to the Maryland Nanocenter staff for both providing training and general guidance throughout my research projects.

Specifically, I want to thank Tom Loughran, Jonathan Hummel, John Abrahams and Mark Lecates for not only helping with equipment but also for the fun conversations that made working in the FabLab an incredibly enjoyable experience.

There are several faculty and staff on campus who have been an additional source of support throughout my time at UMD. Thank you to Professor Mary Bowden for being a source of inspiration and guidance as I navigate my career options. I also want to thank Professor André Tits for all the helpful conversations in determining my career and for all the assistance with the ECE Graduate Student Association (ECEGSA). Special thank you to Melanie Prange for always being ready to answer my questions even when I drop by unannounced! In addition, I want to thank all the members of Women in ECE and the ECEGSA. Your efforts to make UMD an enjoyable experience for all graduate students has paid off, and I enjoyed working with and getting to know all of you.

I want to thank all my friends and family who have stood by me and supported me through these years. Thank you to Joshua Tuttle for all your love, support and encouragement. Thank you to my mom and dad, and to Kristen, Elliot, Cheryllyne, Andrew, Ya'el, and, most recently, Noah. Even from afar they have been a strong source of love and encouragement throughout my education. I want to especially thank Kate Hargrove who is the best friend anyone could ask for and without whom completing this thesis would have been impossible. I additionally want to thank Caley, Anne and Lucian for accepting me into their family. Finally, I want to thank Adrienne McCloud, Katrina Wozniak and Gurpreet Singh for being such wonderful friends and keeping me sane.

I would not have made it to graduate school if it were not for the support, mentorship and guidance of Stephanie Moyerman, Brian Keating, Brian Kirby and Daniel Pajerowski. Thank you for teaching me how to do research and for mentoring me through my undergraduate education.

Finally, thank you to the many, whom I have not mentioned here, that have both helped and befriended me along this journey. This material is based upon work supported by the NSF CAREER Grant No. ECCS-1554503, and the Office of Naval Research YIP Award under Grant No. N00014-16-1-2540. I was personally supported by a NSF Graduate Research Fellowship (DGE 1322106, ECCS-1554503) and an Ann G. Wylie Dissertation Fellowship.

Table of Contents

List of Tables

List of Figures

List of Publications

This thesis is based in part on the following publications:

Lisa J. Krayer, Kevin J. Palm, Chen Gong, Alberto Torres, Cesar E.P Villegas, Alexandre R. Rocha, Marina S. Leite, and Jeremy N. Munday, Enhanced near–infrared photoresponse from nanoscale AgAu alloyed films *Manuscript in Preparation.*

Jongbum Kim, **Lisa J. Krayer**, Joseph L. Garrett, Jeremy N. Munday, Interfacial defects mediated near–infrared silicon photodetection with metal oxides. *Accepted in ACS Applied Materials & Interfaces.* DOI: 10.1021/acsami.9b14953

Lisa J. Krayer, Jongbum Kim, Joseph L. Garrett, and Jeremy N. Munday, Optoelectronic devices on index–near–zero substrates. *ACS Photonics* **2019** 6 (9), pp 2238-2244.

Lisa J. Krayer, Jongbum Kim, and Jeremy N. Munday, Near–perfect absorption throughout the visible using ultrathin metal films on index–near–zero substrates [Invited]. *Opt. Mat. Exp.* 9, 330-338 (2019).

Lisa J. Krayer, Elizabeth M. Tennyson, Marina S. Leite, and Jeremy N. Munday, Near–IR Imaging Based on Hot Carrier Generation in Nanometer–Scale Optical Coatings. *ACS Photonics*, **2018**, 5 (2), pp 306-311.

Joseph L. Garrett, **Lisa J. Krayer**, Kevin J. Palm, and Jeremy N. Munday, Effect of lateral tip motion on multi–frequency atomic force microscopy. *Appl. Phys. Lett.* **111**, 43105 (2017).

Tao Gong, **Lisa J. Krayer**, and Jeremy N. Munday, Design concepts for hot carrier–based detectors and energy converters in the near ultraviolet and infrared. *J. of Photonics for Energy* **6**, 42510 (2016).

Tao Gong, **Lisa J. Krayer**, and Jeremy N. Munday, Hot electron detectors and energy conversion in the UV and IR. *Proc. SPIR 9608*, Infrared Remote Sensing and Instrumentation XXIII, 96081C (2015).

List of Abbreviations and Variables

CMOS	Complementary Metal-Oxide-Semiconductor
EDOS	Electron Density of States
EQE	External Quantum Efficiency
FP	Fabry Pérot
INZ	Index-Near-Zero
IQE	Internal Quantum Efficiency
IR	Infrared
NEP	Noise equivalent power
NIR	Near-Infrared
NUV	Near-Ultraviolet
SB	Schottky Barrier
VLSI	Very Large Scale Integration

A_{eff}	Effective area of a device
A^{**}	Richardson constant
A	Absorption
C_f	Device dependent constant in Fowlers equation
D^*	Detectivity
d_{ARC}	Thickness of anti–reflection coating
E_c	Conduction band energy minimum in a semiconductor
E_f	Fermi energy
E_g	Bandgap energy of a semiconductor
E_v	Valence band energy maximum in a semiconductor
h	Planck's constant
I	Current
J	Current density (current / area)
k	Boltzmann's constant
L_e	Hot electron mean free path
m	Schottky diode ideality factor
n	Refractive index of a material
n_j	Refractive index of material j
$\tilde{n}_j$	Complex refractive index of material j
R	Reflectivity
R_s	Series resistance
T	Transmittivity
T_a	Absolute temperature
d	Metal film thickness
V	Voltage
Y_f	Modified Fowler's equation for internal quantum efficiency

Δf	Electrical bandwidth for detectivity measurements
η_t	Transport probability that a hot carrier will reach the Schottky interface
λ_g	Wavelength with energy equal to the bandgap energy of a semiconductor
λ_0	Optical wavelength in vacuum or air
$h\nu$	Energy of a photon (Planck's constant times optical frequency)
ν	Optical frequency
Φ_B	Schottky barrier height

Chapter 1: Introduction

1.1 A brief introduction to Schottky–barrier photodetection

Since Hersche's discovery of infrared (IR) radiation in 1800, the applications of IR detection have expanded dramatically from their original use only by the military for missile detection and night vision. The development of fiber optic communication systems in the late 1960s made IR signal generation and detection essential for everyday modern life. Long distance optical fiber transmission requires low–cost fabrication with attenuation >1dB/km; this result was achieved in 1970s–1980s using vapor axial deposition to fabricate optical fibers with minimum attenuation of 0.2dB/km at 1500 nm, which determined the optical bandwidth for commercial telecommunications[1]. This invention introduced the need for high–quality integrated systems with hybrid optical and electrical components on a single chip in order to facilitate efficient communication[1, 2].

Silicon is the most widely used material for commercial electrical and optical devices because of its natural abundance, low–cost, and beneficial electrical performance, but, unfortunately, its optical bandgap, E_g, of 1.1 eV precludes its use for IR photodetection. In 1973, Shephard and Yang introduced metal–silicide/silicon Schottky barrier (SB) photon detectors, which generate sub–bandgap photocurrent

in the metal–silicide through internal photoemission, marking the first IR photodetector that was compatible with very–large–scale integration (VLSI) technology[3]. A Schottky barrier (SB) diode consists of a metal–semiconductor junction where a potential barrier forms at the interface between the two materials as a result of a mismatch in their work functions. SB detectors transitioned IR cameras from first generation, single pixel, scan–to–image detectors to second generation focal plane arrays with on chip read out[4]. Unfortunately, metal–silicide SB detectors have low absorption, low quantum efficiency and require cryogenic temperatures for operation because of their high dark current due to small barrier heights.

In this thesis, methods of increasing absorption and quantum efficiency are introduced to enhance silicon–based, near–IR (NIR) photodetection at room temperature. Prior to this, silicon–based NIR device performance enhancement relied on complicated device structures and expensive, unscalable nanofabrication techniques that are often difficult to integrate into VLSI technology. The more straightforward methods shown here, involve tailoring the optical and electrical properties of a metal contact by either choosing metals with ideal properties or through alloying. While the performance is heavily dependent on the properties of the metal, this thesis also explores how the surrounding media have a surprisingly significant impact on device performance.

1.2 What is internal photoemission?

In general terms, internal photoemission is the photo-excitation of electrons or holes in a material to a large enough energy for injection into an adjacent material. It is common to refer to the excited electrons or holes as "hot electrons" or "hot holes" respectively, or as "hot carriers" when referring to either excited particle. Figure 1.1 shows the internal photoemission process for an n–type SB detector: (i) a photon with energy $h\nu$ (*i.e.* Planck's constant times the optical frequency) is absorbed in the metal, (ii) the absorbed photon excites a hot electron, (iii) the hot electron then travels to the interface, and (iv) is injected into the semiconductor provided that its energy is greater than the Schottky barrier, Φ_B. The process of internal photoemission for a p–type SB detector is identical except that the band bending in the semiconductor is reversed, and the hot carriers emitted over the barrier are holes, instead of electrons.

In 1967, Cohen *et. al.* modified Fowler's theory for external photoemission (hot electron injection into vacuum) to Schottky photodiodes[5, 6]. A general form of Cohen's modified Fowler equation is now widely used to model the internal quantum efficiency (IQE) of SB detectors[4, 7–10]. The IQE is defined as the ratio of the number of collected hot carriers to the number of absorbed photons, and the IQE as determined by the modified Fowler theory, Y_f, is given by:

$$Y_f = C_f \frac{(h\nu - \Phi_B)^2}{h\nu}, \tag{1.1}$$

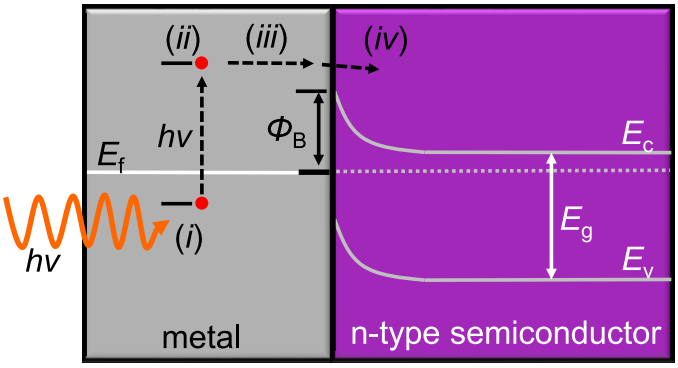

Figure 1.1: Internal photoemission in a Schottky photodiode with light absorbed in the metal contact to an n–type semiconductor. Internal photoemission is a four step process: (i) Light is absorbed in the metal contact, (ii) the absorbed photon excites a hot electron, (iii) the hot electron travels to the metal–semiconductor interface (*i.e.* Schottky interface), and (iv) the hot electron is injected into the semiconductor to be collected as photocurrent.

where C_f is a device dependent constant, h is Planck's constant, ν is the optical frequency of the incident photon, and Φ_B is the Schottky barrier height. This equation was derived assuming the momentum of hot carriers is isotropic and all hot carriers with momentum in the direction of the Schottky barrier will reach the interface. Therefore, the modified Fowler equation is simply the probability that a hot carrier will have a momentum pointed in the direction of the Schottky barrier and enough energy in order to be injected into the semiconductor.

While the assumption that hot carriers are isotropic is generally accepted to be reasonable, the assumption that all excited carriers will reach the interface is dependent on factors such as the direction of illumination, the metal film thickness, d, and electron mean free path, L_e[7, 11]. For example, if $d \gg L_e$ and the metal is illuminated from air, the majority of the hot carriers will be generated far from the metal–semiconductor interface and will thermalize to an energy below the barrier height before reaching the interface, decreasing the IQE. Alternatively, if $d \ll L_e$

then the hot electrons can reflect off each interface multiple times before being injected, increasing the internal quantum efficiency[11]. Therefore, a more complete equation for IQE is given by:

$$IQE(h\nu) = \eta_t(h\nu)Y_f(h\nu), \tag{1.2}$$

where η_t is the probability that a hot carrier will reach the interface with energy greater than the Φ_B. Dalal derived fairly complex equations for the IQE considering front (from air) and back (from the semiconductor) illumination and carrier mean free paths[7]. In addition, Vickers developed a model that considers hot carrier collisions with phonons and impurities in the metal[10]. However, general practice is to use η_t as a fitting parameter because it is challenging to accurately calculate in a real system.

1.3 Methods for light absorption in metals

The first step of internal photoemission in a SB detector requires light absorption in a metal film, which poses a challenge because metals are highly reflective and therefore have low absorption. The first SB detectors illuminated thin metal–silicide films through a silicon substrate (see Figure 1.2a), which resulted in less than 30% absorption of sub–bandgap photons[3, 12]. Early attempts to enhance the absorption in the metal film involved creating a dielectric optical cavity in which the incident light forms a standing wave (see Figure 1.2b), increasing the light interactions with the metal film[12–14]. This method can enhance the absorption in the

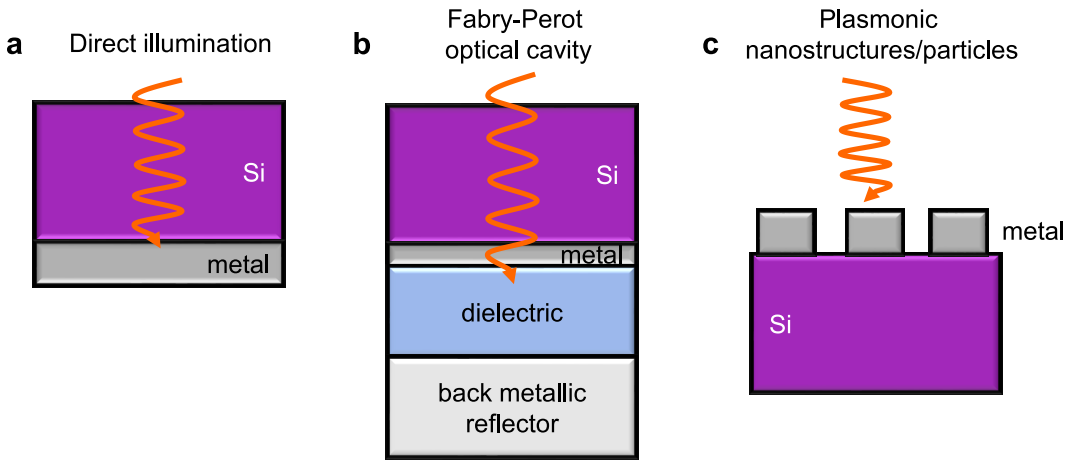

Figure 1.2: Three methods of absorbing light in metal films are: (a) direct illumination through a silicon substrate, (b) using a Fabry–Pérot optical cavity that utilizes a transparent dielectric and metallic reflector layer to create a standing wave in the dielectric to increase light interactions with the thin metal film, (c) using nanostructures or nanoparticles to excite plasmonic resonances for near perfect absorption.

metal to ~40%; however, this amount of absorption is still relatively low. In spite of this result, the early SB diode designs had two primary benefits: (i) they are compatible with VLSI technology and (ii) they extend the detectable bandwidth of a silicon detector without inhibiting the detector's performance above the bandgap.

A more recent approach of enhancing absorption in metals involves exciting surface plasmon resonances using nanoantennas[8, 15] or an array of nanostructures[9, 16] (see Figure 1.2c). Surface plasmons are coherent oscillations of electrons in a metal film that are excited when the momentum of incident light matches the momentum of the electron oscillations. Geometric nanostructures enable momentum matching between normal incident light and the electron oscillations[17]. After excitation, the surface plasmons decay to excite hot electrons, which can then be injected into a semiconductor substrate through the internal photoemission process. While plasmonic resonances generally have a narrow absorption bandwidth,

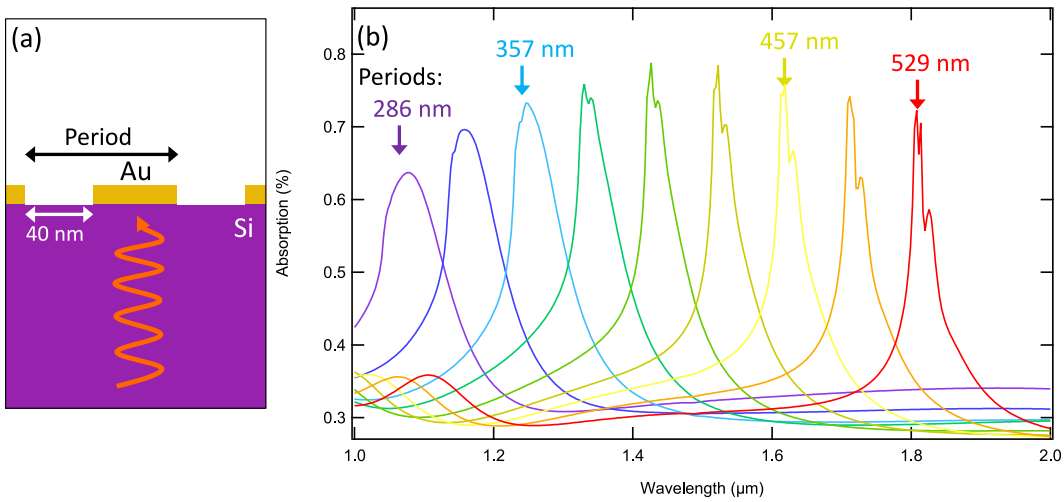

Figure 1.3: Plasmonic resonant structures with high absorption when illuminated through the silicon substrate. (a) Schematic showing Si/Au plasmonic photodetector consisting of 15 nm thick Au bars forming a grid with a 40 nm gap between bars. (b) As the periodicity of the nano–grid is increased with a fixed gap at 40 nm, the absorption peaks are red shifted.

multidimensional 3D arrays can be used for broadband absorption[9].

The benefit of using plasmonic resonances for absorption is that near–unity absorption is achievable within the metal. However, the metal nanostructures typically are fabricated on the top surface of the silicon substrate causing reduced device performance for above–bandgap detection. This effect can be mitigated by illuminating the nanostructures through the silicon substrate as shown in Figure 1.3. This figure is modified from reference [18]. Here a Au nano–grid can be used for >60% absorption over a narrow bandwidth determined by the periodicity of the grid. Unfortunately, most plasmonic devices require nanotexturing, which is both costly to fabricate and difficult to scale to large area devices, and therefore, plasmonic photodetectors are generally not compatible with VLSI technology.

1.4 Outline of this thesis

It was recently found that thin, planar, and lossy semiconducting films can achieve high absorption without nanotexturing due to a Fabry–Pérot (FP)–like cavity effect[19]. This thesis explores how the FP–like cavity effect can be expanded to metal optical coatings for increasing the absorption and quantum efficiency in the original SB photodiode device structure of direct illumination of a planar metal film through a silicon substrate, Figure 1.2a. This device structure does not require costly and unscalable nanotexturing and has been proven to be compatible with VLSI technology.

Chapter 2 of this thesis is a proof–of–concept demonstrating that the FP–like cavity effect can be used with metal films to achieve >70% broadband absorption in a planar metal film. That chapter explores the theoretical material requirements for high absorption and experimentally verifies the theory through the realization of a silicon–based NIR photodetector that can take images at room temperature. That chapter is based on the published manuscript L.J. Krayer, E.M. Tennyson, M.S. Leite, & J.N. Munday, "Near–IR Imaging Based on Hot Carrier Generation in Nanometer–Scale Optical Coatings." *ACS Photonics* **2018**, 5, 2, 306-311.

Chapter 3 takes a closer look at the theory for the FP–like cavity effect, considering not only the optical properties of the metal film, but also of the surrounding media. We present design considerations for achieving near–perfect, broadband absorption in planar metal films. We find that index–near–zero (INZ) substrates can be used to obtain near–unity absorption in metal films even without a silicon su-

perstrate. That chapter is based on the published work L.J. Krayer, J. Kim, and J.N. Munday, "Near–perfect absorption throughout the visible using ultrathin metal films on index–near–zero substrates [Invited]." *Opt. Mat. Exp.* 9, 330-338 (2019).

Chapter 4 experimentally verifies the theory presented in Chapter 3. We find that INZ substrates not only enhance the absorption in the metal film, but also improve the carrier dynamics for enhanced IQE of a silicon–based SB photodiode. That chapter is based on the recently published manuscript L.J. Krayer, J. Kim, J.L. Garrett, and J.N. Munday, "Optoelectronic devices on index–near–zero Substrates." *ACS Photonics* **2019** 6 (9), pp 2238-2244.

Chapter 5 considers the electrical properties of the absorbing metal and explores metal alloys that can be used for increased absorption and tunable carrier transport properties. Specifically, we explore AgAu alloys and find that the alloys improve the absorption in the metal; however, we find that pure Au still has the highest IQE because of its superior hot electron mean free path. That chapter is based on the recently submitted manuscript L.J. Krayer, C. Cong, K.J. Palm, A. Torres, C.E.P Villegas, A.R. Rocha, M.S. Leite, and J.N. Munday, "Near–infrared photoresponse from ultrathin AgAu alloyed films".

Finally, Chapter 6 concludes this thesis with future considerations and closing remarks.

Chapter 2: Near–IR imaging based on hot carrier generation in nanometer–scale metal films

Silicon (Si) has emerged as an important material for telecommunications, enabling hybrid optical and electrical components to be combined onto a single integrated chip[20–22]. It is a mature, low–cost technology that is dominant throughout the microelectronics industry. However, the bandgap of Si ($E_g = 1.1$ eV; $\lambda_g = 1100$ nm) severely constrains its use for generation and detection of light throughout the telecommunications band (1260-1625 nm). To circumvent this limitation, a second semiconducting material is often introduced, such as Ge to produce telecom lasers[23] and photodetectors[24, 25], III-V materials[26], or GeSn alloys[27, 28]; nevertheless, Si–only approaches are desirable because they can easily be incorporated with traditional fabrication methods. Options for Si–only sub–bandgap photodetection include increased absorption from intrinsic defect states within the Si bandgap[29], induced defect states by ion implantation[30], or photon absorption and internal electron emission from a metal film (typically metal silicides such as PtSi or pure metals such as Au or Cu) across a Schottky barrier[8, 9, 12, 31]. However, one of the key drawbacks of internal electron emission is that it requires significant absorption within a thin metal film, which is usually highly reflective

in the near-infrared (NIR) spectrum[12, 32]. For example, metal silicides generally have little absorption and require low temperature operation because of high dark current due to small barrier heights. Nanostructured films and antennas can be used to increase the absorption but suffer from significant wavelength, polarization, and angle of incidence dependence.

Recently, it has been shown that ultrathin (∼10 nm) dielectric and semiconducting films can become nearly perfect absorbers based on nontrivial phase accumulation in lossy materials[19, 33–36]. This phenomenon occurs by exciting Fabry-Pérot–like (FP) resonances in cavities 10-100× smaller than the incident wavelength of light. Such films have been used to construct ultrathin color filters[19, 35], enhance photochemical water splitting efficiency[37], and create near–unity perfect absorbers[38, 39]. Despite these successes based on dielectric and semiconducting materials, expanding this concept to ultrathin metal films could enable near perfect NIR photon absorption for Schottky barrier photodetectors and allow for seamless integration to CMOS telecommunication applications.

In this chapter, we demonstrate a Si–based photodetector that operates in the NIR, beyond the semiconductor bandgap, by exploiting a zeroth–order FP–like resonance in ultrathin metal films. The devices are composed of a Si/metal layer stack, where the lithography–free, ultrathin metallic layer generates photocurrent at room temperature in the NIR due to hot carrier (electron) generation. The devices absorb nearly 80% of the incident radiation beyond the Si bandgap and are broadband. We identify four metals that satisfy this resonance condition in the telecom band: Pt, Fe, Ti, and Cr. As a proof–of–concept, we fabricate and test

Si/Pt photodetectors that outperform commercial Si devices in the NIR (>1.2 μm) and demonstrate their imaging capability. We foresee the development of low–cost, Si IR and NIR detectors for next–generation Si photonics based on our findings.

2.1 Calculated absorption in ultrathin metal films

Our device geometry, presented in Figure 2.1a, consists of an n–type Si substrate (368 μm thickness) and an ultrathin film metal (16 nm thick Pt) absorbing layer. In addition to providing optical absorption and hot carrier generation, the metal film acts as a Schottky contact for carrier injection. Al is used for the top Ohmic contact, and a SiN_x coating is added to the top of the Si layer to reduce reflection of the incident light. Figure 2.1b shows the device band diagram, where NIR photons with energy $\hbar\omega$ are resonantly absorbed within the metal before exciting hot carriers. These hot carriers are then directly injected into Si, if their excitation energy is greater than the barrier height, Φ_B. We analytically determine the absorption of ultrathin metal films in contact with Si using Fresnel equations for a single stack of Si/metal/air varying the metal's refractive index ($\tilde{n}_2 = n + i\kappa$) and layer thickness ($d$) at a wavelength of 1.2 μm (see Appendix A, eqs A.1 – A.6, for calculation details). While the Fresnel equations are used for all quantitative analyses, additional insight can be gained by considering the following special case: (i) the surrounding layers are optically thick and nonabsorbing, (ii) the real (n) and imaginary (κ) parts of the metal's refractive index are large and approximately equal to each other (i.e., $n \approx \kappa \gg 0$), (iii) the refractive index of the top layer (n_{top}, here

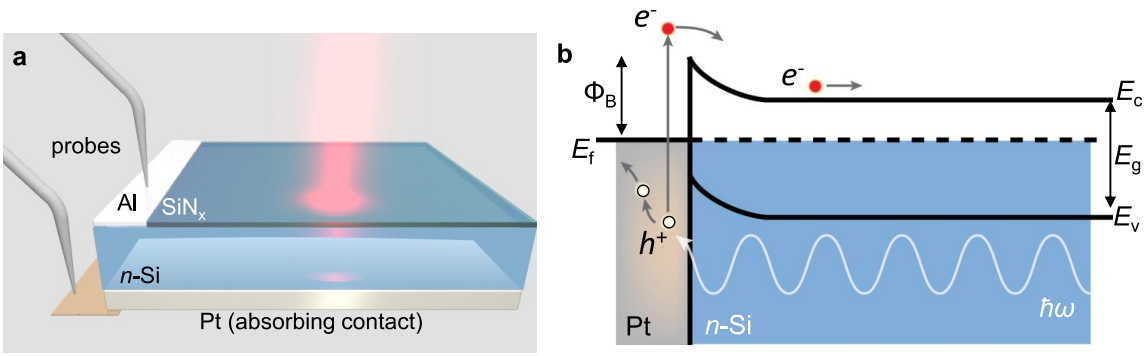

Figure 2.1: Hot carriers for Si photodetection beyond the material's bandgap. (a) Illustration of device structure, out of scale for clarity. From top to bottom: Al top Ohmic contact (left side only), antireflection coating (SiN_x), n–type Si layer, ultrathin Pt absorbing contact layer. Sub–bandgap light passes through the device to be absorbed in the thin back contact. Electrical connections are made to the top and bottom contacts. (b) Energy band diagram showing the hot carrier absorption concept: light with energy below the Si bandgap ($\hbar\omega < E_g$) is absorbed by the back metal contact (Pt), which generates hot electrons (e^-) that are injected into the semiconductor when their energy is greater than the barrier height Φ_B.

corresponding to Si) is greater than or equal to that of the bottom layer (n_{bot}, which corresponds to air in our case), and (iv) the optical path length in the metal film is significantly shorter than the wavelength of incident light (i.e., $d \ll \lambda_0/2\pi$, where λ_0 is the wavelength in air). Under these criteria, the maximum possible absorption in a metal film is determined by the optical properties of the surrounding layers[33]:

$$A_{max} \approx \frac{n_{top}}{n_{top} + n_{bottom}}. \tag{2.1}$$

When the top layer is Si and the bottom layer is air, it is possible to obtain significant light absorption (77.8%) in a metallic film 2 orders of magnitude thinner than the excitation wavelength.

The specific real and imaginary parts of the refractive indices that satisfy the requirements for maximum absorption shift to larger values along the $n = \kappa$ line as

the film thickness decreases (see Figure 2.2). Note that 77.8% absorption can be achieved even in a film thickness of 1 nm, see Figure 2.2a. For this thickness, the optical indices of the material needs to satisfy $n \sim \kappa \sim 20$, for which there are no common metals. However, for larger thicknesses, still in the nanoscale regime, many common materials can meet the resonance condition. For example, at $d = 20$ nm, platinum (Pt), iron (Fe), chromium (Cr), and titanium (Ti) lie near the absorption peak (Figure 2.2e).

Analytical calculations for these materials show broadband absorption >70% for films as thin as 10 nm over a range of wavelengths throughout the NIR, see Figure 2.3. The refractive indices for these calculations are taken from refs [40] and [41], and the refractive index of air is set to be 1. The FP resonance is possible for these metals as long as $d \ll \lambda_0/2\pi$. Therefore, high absorption is maintained across a broadband of wavelengths because the metal film thicknesses are $\sim 100\times$ smaller than the incident light. Note that Pt maintains the highest absorption for the thinnest film.

2.2 Experimental demonstration of high absorption and photocurrent in ultrathin metal films.

We measure the absorption in the four thin metal films with optimized thicknesses, as determined by the calculations in Figure 2.3. Each sample is fabricated with an antireflection coating of 170 ± 5 nm of SiN_x on the top surface of a double sided polished Si wafer to reduce the incident light reflection from the Si, resulting

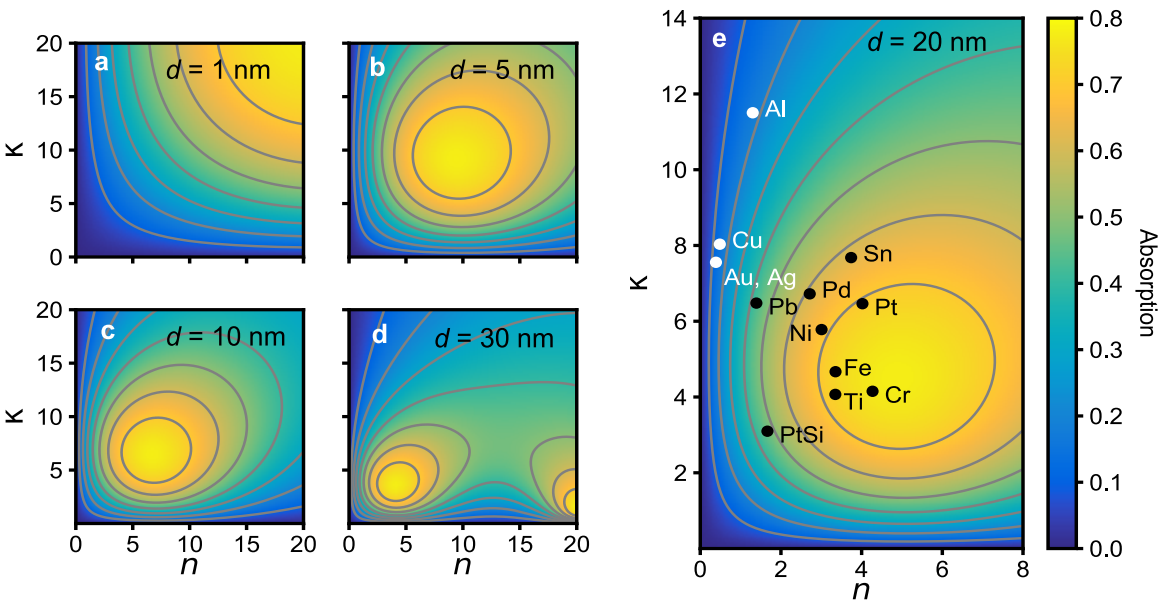

Figure 2.2: Light absorption in metallic ultrathin films. (a – d) Absorption contour plots as a function of $n = n_m + i\kappa_m$ for thin metal films with variable thicknesses (d = 1-30 nm) on the backside of bulk Si. Illumination ($\lambda = 1.2$ μm) is from free space through the SiN_x/Si layers. (e) Absorption contour plot for metal thin films with thickness $d = 20$ nm. Black and white dots denote refractive indices for common metals at $\lambda = 1.2$ μm, showing high absorption of selected metals.

in a minimum at a wavelength of 1.35 μm (see section 2.4.2). The metal is deposited on the Si surface opposite of the SiN_x coating, forming a back Schottky contact, as depicted in Figure 2.1. Figure 2.4a-d presents the comparison of the experimental and analytical absorption in all four metals after accounting for the loss due to reflection from the SiN_x. Each sample is illuminated from the SiN_x side. Cr has the highest absorption with an average value of 73.7%; however, the thickness required is double that of Pt, which has an average absorption of 71.5% in a thickness of merely 16 nm.

Pt is the most promising material for a hot carrier photodetector from the four options we investigated. The electron mean free paths of Pt and Fe are reported to be ~10 nm[42] and 2-8 nm[42, 43], respectively, and are comparable to

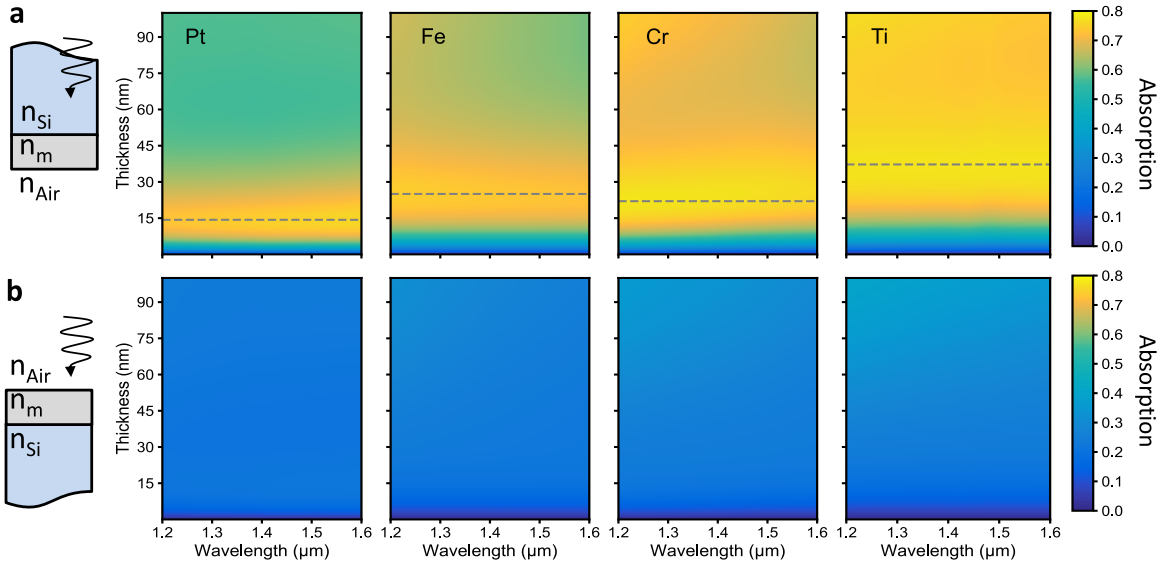

Figure 2.3: Light absorption as a function of film thickness in Pt, Fe, Cr, and Ti, respectively. The dotted lines are a guide to the eye indicating the thickness for maximum absorption. (a) When illuminating the thin film through a silicon substrate (*i*.e. $\tilde{n}_{top} = \tilde{n}_{Si}$ and $\tilde{n}_{bottom} = 1$), Pt, Fe, Cr and Ti achieve 75.9%, 74.4%, 77.8% and 77.5% at 14.3 nm, 25.0 nm, 22.0 nm, and 37.2 nm thicknesses, respectively. (b) When illuminating the thin film through air (*i*.e. $\tilde{n}_{top} = 1$ and $\tilde{n}_{bottom} = \tilde{n}_{Si}$), the absorption no longer displays a thin film resonance and the absorption maximum is greater than the film thickness displayed here. For the same film thickness that maximize absorption in (a) each metal absorbs only 22.2%, 23.1%, 23.7%, and 25.3% respectively.

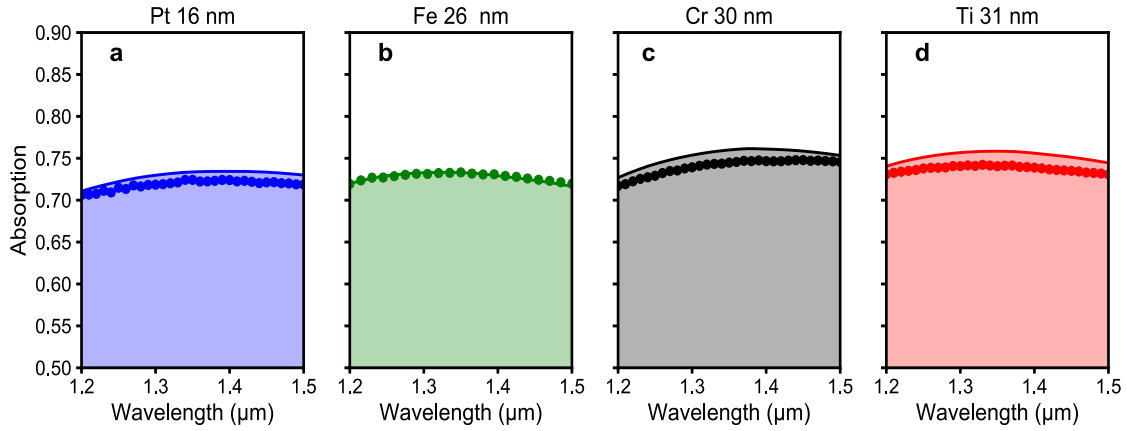

Figure 2.4: High optical absorption in metals due to a Fabry-Pérot resonance. Measured (circles) and calculated (lines) absorption for (a) 16 nm of Pt, (b) 26 nm of Fe, (c) 30 nm of Cr, and (d) 31 nm of Ti in a Si/metal stack. Film thicknesses were chosen for maximum absorption.

the thickness of the ultrathin absorbers, whereas the electron mean free paths for Cr and Ti are expected to be < 1 nm[44]. However, the expected barrier height for Fe in contact with n–Si is 0.45 eV, significantly lower than Pt, which leads to a large increase in dark current, thus reducing the photoresponse of the device at room temperature[32]. Because Pt achieves maximum absorption for thinner layers, the probability for internal photoemission is potentially larger due to the increased likelihood of hot carrier reflection from the back surface[7]. Pt also has a larger Schottky barrier height to n–Si, which reduces the overall dark current, enabling room temperature detection[32]. In Figure 2.5a,b, we show measured and calculated absorption for various thicknesses of Pt to verify the optimal layer thickness for maximum absorption. A thickness of 16 nm results in a maximum, and changing the thickness by 5 nm reduces the absorption by only ∼2-5%, in excellent agreement with theory. To efficiently generate hot electron photocurrent, the absorbed radiation should excite electrons to energy levels above Φ_B for injection into the Si. Φ_B for each Pt device varied between 0.69 and 0.72 eV, as determined from dark IV measurements (see section A.3 and Figure 2.11). To demonstrate the effect of the higher absorption on photoresponse, Figure 2.5c shows the measured photoresponse for devices with Pt thicknesses of 0, 16, and 36 nm. The 16 nm device has 2-3× larger photocurrent compared to the 36 nm one because of its higher absorption and greater probability of internal photoemission. The hot carrier devices are further compared with the photoresponse of bare Si, where the 10^{-6}-10^{-8} A/W photoresponse is likely due to trap states or two photon absorption; therefore, the hot carrier effect in Pt produces a 100× increase in photocurrent compared to the

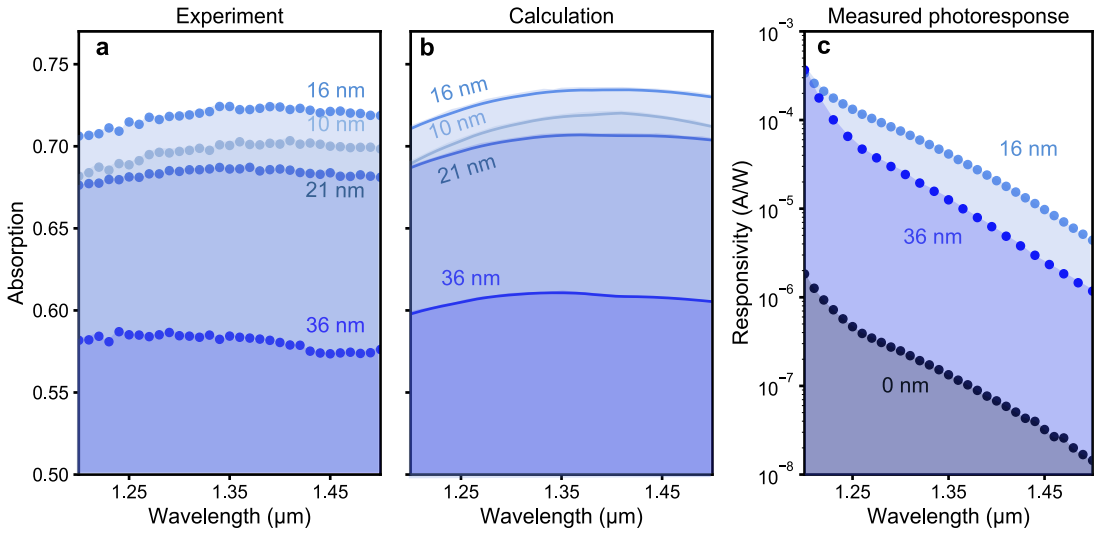

Figure 2.5: Ultrathin Pt layer leads to Si photodetection in the NIR. (a) Measured and (b) calculated absorption for 10, 16, 21, and 36 nm of Pt. Maximum absorption occurs for a Pt thickness of 16 nm. (c) Device photoresponse using 0, 16, and 36 nm of Pt. As expected, the 16 nm thick layer yields the highest photoresponse.

bare Si device. We also note that while the overall shape of the responsivity curve is similar for both the bare–Si device and the Pt devices, they result from different effects. The decrease in responsivity as a function of wavelength for the bare–Si device results from the continued decrease in the residual absorption beyond the bandgap. For the Pt devices, the absorption is nearly constant (Figure 2.5a,b); however, the internal quantum efficiency decreases as lower energy carriers are less likely to traverse the barrier[45].

As expected, if the sample orientation is reversed so that the metal is illuminated from the air rather than Si, the maximum absorption and photoresponse is reduced by nearly 3×, in agreement with eq 2.1 for $n_{top} \sim 1$ (air) and $n_{bottom} \sim 3.5$ (Si) (see Figure 2.6).

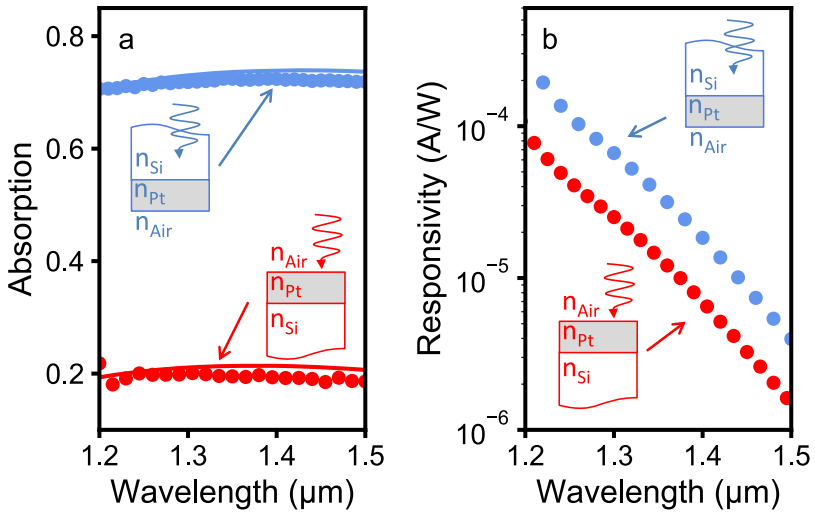

Figure 2.6: Effect of illumination direction on device operation. (a) Absorption in the 16 nm Pt hot carrier device illuminated from the Si (blue) and from the air (red) sides. The circles are experimental data and the lines are from calculations. (b) Responsivity under illumination from Si (blue) and from air (red).

2.3 Near-infrared photodetector

We realize a NIR imaging photodetector based on the Pt hot carrier concept discussed in the previous paragraphs, which outperforms commercial Si devices. Figure 2.7a shows a backside-illuminated optical image of the object used to test our Si-based Pt photodetector, formed by an optically thick layer of Au in a spiral shape on top of a quartz substrate. The quartz is transparent for all incident wavelengths while the Au is opaque. Thus, it is expected that the regions coated by Au will appear dark to the photodetector, while the quartz appears bright. We compare the performance of our hot carrier device (Figure 2.7b-e) with a standard commercial Si detector (Figure 2.7f–i) for illumination near and below the bandgap of Si. Here, we use identical experimental conditions and place the detectors after an objective lens

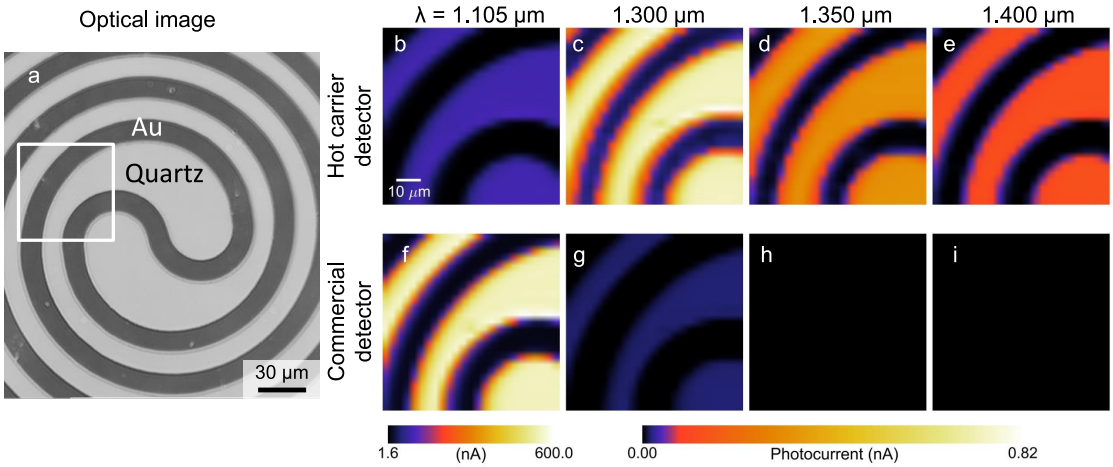

Figure 2.7: NIR imaging with the ultrathin film hot carrier photodetector. (a) Optical image of Au/Quartz structure, acquired using a 20× objective lens (NA = 0.4). The boxed region indicates the area imaged in (b)-(i). Images obtained by (b-e) the hot carrier photodetector consisting of 16 nm of Pt and (f-i) a commercial Si device. Beyond the Si bandgap, the hot carrier device outperforms the conventional Si photodetector.

used to collect all transmitted light (for a detailed description of the experimental setup, see Figure 2.13). The hot carrier device produces a detectable and reliable current signal for $\lambda > 1.25\mu$m, while the signal of the commercial detector fades dramatically as the wavelength of illumination increases beyond 1.1 μm. Note that this commercial Si detector generates very little current at $\lambda \sim 1.30$ μm (below Si bandgap energy, see Figure 2.7g), likely resulting from the presence of trap states within the semiconductor. These states subsequently increase the device dark cur-

rent, which is detrimental to its performance. The commercial detector produces greater photoresponse near the bandgap (see Figure 2.7b,f for comparison), as expected because the hot carrier detector demonstrated in this paper is not optimized for wavelengths at or above the bandgap of Si. One strategy to further increase the performance of the Pt hot carrier device consists of heavily doping the Si layer at the metalsemiconductor interface to reduce the barrier height (Φ_B in Figure 2.1b) and increase both the bandwidth and responsivity due to improved collection of photoexcited carriers from *d*-band states[46]. In this case, there is a trade-off because the increase in dark current must also be considered. Additionally, shrinking the overall device area can decrease the capacitance, which in turn, increases carrier collection efficiency[47]. Concerning alternative materials, metallic alloys could be used to tune the optical and electrical properties of the metal layer for greater light absorption and hot carrier collection in thin films[31, 48, 49]. Nevertheless, here we show a facile approach based on hot carrier generation that surpasses current commercial Si technology for room temperature, zero–bias, NIR detectors.

2.4 Fabrication methods and experimental details

This section contains additional device characterization and information on fabrication methods and experimental design.

2.4.1 Sample fabrication

All devices were fabricated on 368 μm thick, double side polished, $< 100 >$ n–type silicon wafers (1-10 Ω·cm). Wafers were cleaned in a piranha etch (3:1 sulfuric acid (H_2SO_4) and hydrogen peroxide (H_2O_2)) to remove all organic material. A buffered oxide etch (BOE) was used to remove the native oxide, and dried under an N_2 stream. Immediately after the cleaning procedure, ohmic contacts were formed by depositing aluminum (Al) through a shadow mask in a thin strip along the top surface of each device, which was annealed at 425 °C in a forming gas of 96% Ar and 4% H_2. Then a ∼170 nm SiN_x antireflection coating was deposited using an Oxford plasma enhanced chemical vapor deposition (PECVD) system through a shadow mask, keeping the Al uncoated to enable electrical connection to the device. Finally, the native oxide was removed from the back surface of the Si with BOE, and the absorbing ultrathin metal contacts were deposited using an Angstrom e-beam evaporator at a deposition rate of $\sim 1\mathring{A}$ s^{-1} at a pressure of $\sim 2 \times 10^{-6}$ Torr through a shadow mask, allowing for multiple metal thicknesses to be deposited on the same device.

2.4.2 Calculated reflection from the antireflection coating

Silicon nitride is a common antireflection coating for Si devices because its index of refraction is close to ideal for minimizing the reflection from a polished silicon surface. The thickness, d_{ARC}, for minimum reflection is determined by the quarter-wavelength condition within the SiN_x for destructive interference of the

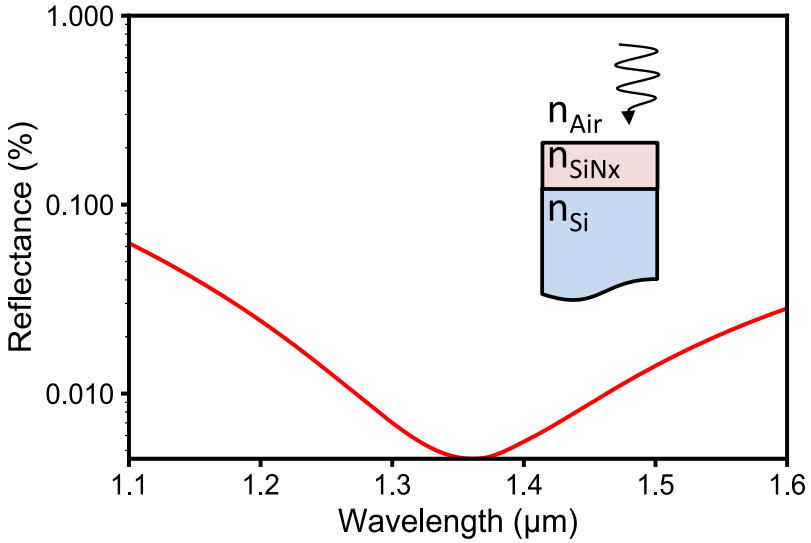

Figure 2.8: Anti-reflection coating. Analytically calculated reflectance with illumination from the Si side with a 170 nm thick SiN_x antireflection coating (using optical data of Si_3N_4).

reflected wave:

$$d_{ARC} = \frac{\lambda_0}{4n}, \tag{2.2}$$

where λ_0 is the wavelength in air, and n is the index of refraction of the SiN_x. A thickness of 170 nm gives a minimum reflection at $\sim$ 1.35 μm. We calculate the analytical reflectance with the Fresnel equations, as used for determining the absorption in the thin metal films. Figure 2.8 shows the reflectance calculated with optical data for Si_3N_4 taken from ref [50]. Because the reflectance over the wavelength range 1.1 – 1.6 μm remains below 6%, 170 nm of SiN_x was chosen for the fabricated devices.

2.4.3 Optical and electrical measurements of Pt/n–Si photodetector

Specific wavelengths were selected from a supercontinuum source (Fianium WhiteLase) using an acousto-optic tunable filter (AOTF). Absorption measurements were performed using a 6 in. integrating sphere (Labsphere RTC–060) with illumination at near-normal incidence of 12°. One Ge photodiode was used to measure the light intensity inside the integrating sphere, and a second was used to monitor power fluctuations of the incident beam.

All electrical and photocurrent measurements were performed using probe connections to the top (Al ohmic contact) and bottom (Pt Schottky contact). The signal from each photodiode and the photocurrent from the hot carrier detectors were measured using a SR830 lock-in amplifier. The power incident on the sample was measured using a calibrated Ge photodiode to calculate the responsivity. All photocurrent measurements were taken at zero applied bias.

The photocurrent was measured at four positions along the 16 nm thick Pt device to verify that the photocurrent was uniform and generated within the Pt thin film (2.9). The first two positions (3.0 mm and 4.5 mm) correspond to illumination of the Si with a 16 nm Pt layer underneath, which generated 10^{-3}-10^{-6} A/W from wavelengths 1.15 - 1.55 μm. The second two positions correspond to illumination of only the Si (no Pt deposited in this region), which resulted in three orders of magnitude lower responsivity. The presence of any photocurrent in the pure Si demonstrates the existence of trap states within the material.

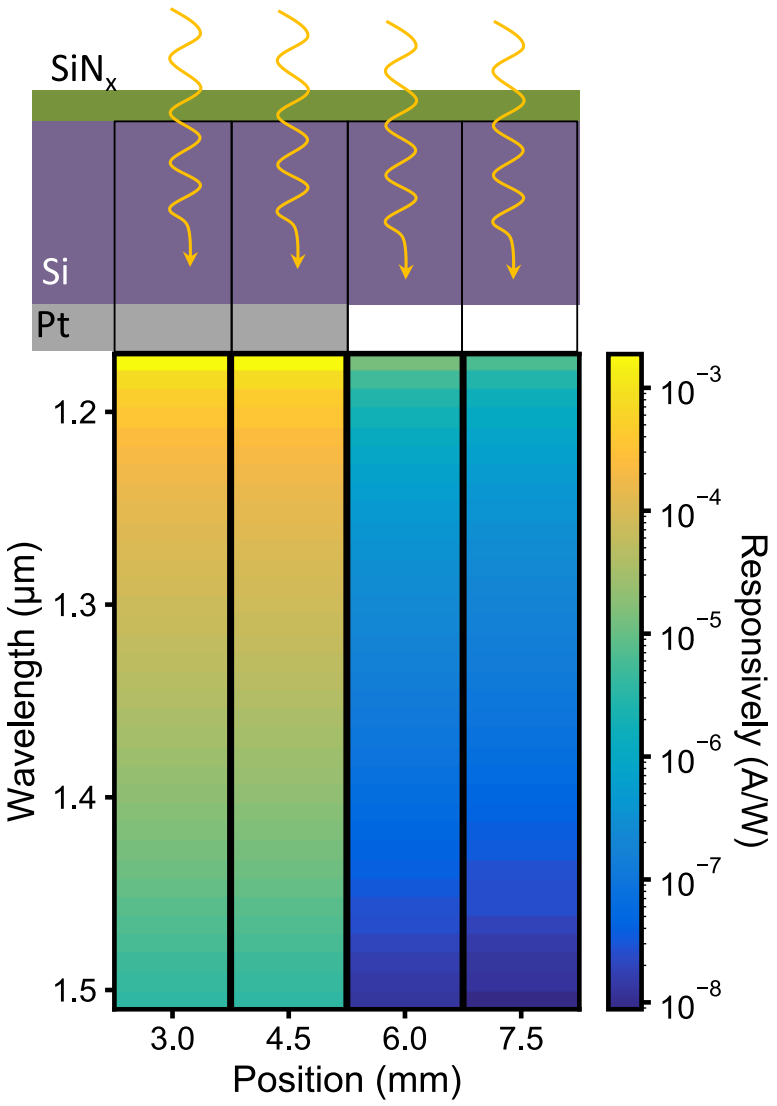

Figure 2.9: Responsivity at four positions along the hot carrier device. At 3.0 and 4.5 mm positions, light illuminates the device and is absorbed by the Pt. However, at 6.0 mm and 7.5 mm, there is no Pt and only Si is illuminated, resulting in a three orders of magnitude decrease in the response.

Figure 2.10a shows the measured photocurrent of the 16 nm Pt device over a range of incident powers from 140 – 800 μW at a wavelength of 1.25 μm demonstrating that the photocurrent generation is a linear process. Figure 2.10b shows the dark I–V characteristics of the same diode measured with a Keithley 2400 source meter (the current and voltage was recorded using a custom-built LabVIEW script)

demonstrating that the device behaves as a Schottky diode.

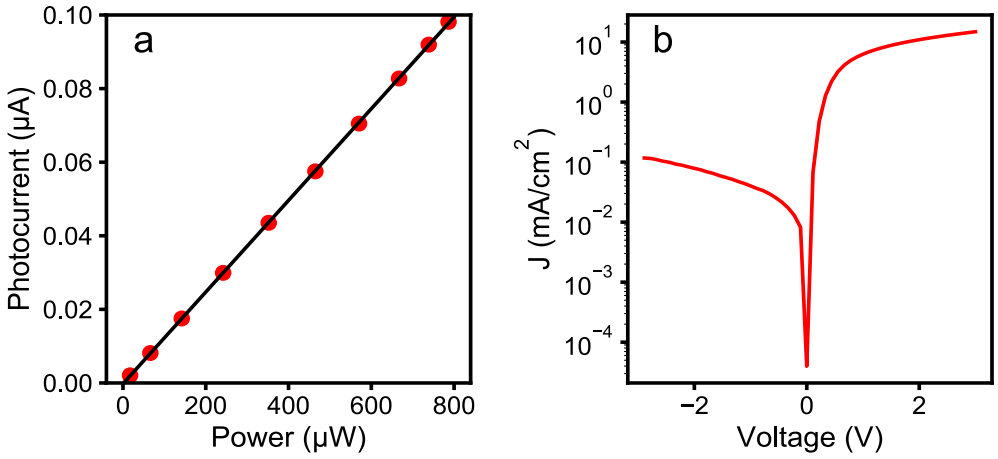

Figure 2.10: Electrical characteristics of the 16 nm Pt hot carrier device. (a) Photocurrent for incident wavelength of 1.25 μm verifying a linear relationship with input power. (b) Dark current density and voltage relationship of the Pt 16 nm hot carrier device.

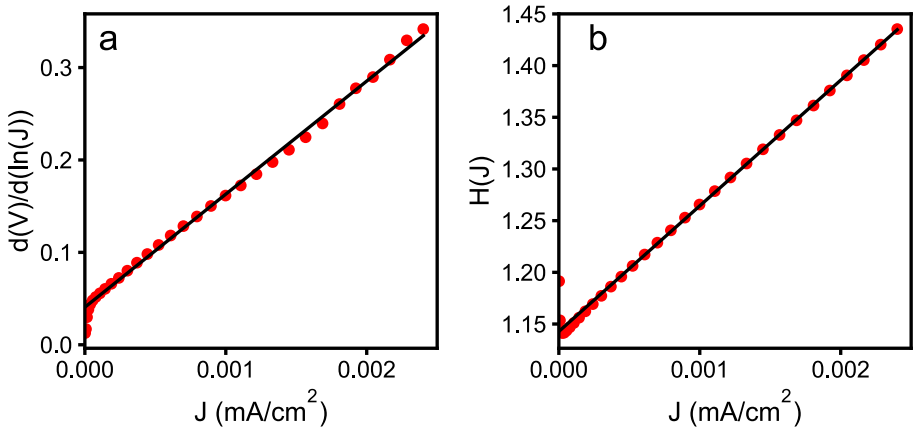

Figure 2.11: Thermionic emission fit. The experimental dark I–V data from the 16 nm Pt device are fit to (a) Eq. A.15 and (b) Eq. A.17 to determine the ideality factor and the barrier height, respectively.

The Schottky barrier height, Φ_B, of each device can be extracted from the forward biased dark I–V curve (Figure 2.10b) using the thermionic emission model. Cheung, *et al*, demonstrated that the thermionic emission equation can be broken

into two linear relationships, $\frac{d(V)}{d(lnJ)}$ (Eq. A.15) and $H(J)$ (Eq. A.17), which can be used to determine Φ_B, the ideality factor (m), and series resistance (R_s) of the device (see Appendix A section A.3). Figure 2.11 shows the fits for the 16 nm Pt hot carrier device. From the fit to $\frac{d(V)}{d(lnJ)}$, a resistance of $R_s = 211\ \Omega$ and an ideality factor of $m = 1.49$ was extracted. This high ideality factor suggests that there is a small layer of Pt diffusion at the Schottky interface. From the fit to $H(J)$, a resistance of $R_s = 209\ \Omega$ and a barrier height of $\Phi_B = 0.72$ eV was extracted. The similarity of the resistances between the two fits shows good agreement of the fit parameters between the two equations.

Specific detectivity, D^*, defined as the minimum signal a photodetector is able to measure normalized with respect to the active area and electrical bandwidth, is determined[4]:

$$D^*(\lambda) = \frac{(A_{eff}\Delta f)^{1/2}}{NEP} = \frac{R(\lambda)}{I_n}(A_{eff}\Delta f)^{1/2}, \tag{2.3}$$

where A_{eff} is the active area of the device, Δf is the electrical bandwidth, and NEP is the noise equivalent power calculated by the ratio of dark current, I_n, to spectral responsivity, $R(\lambda)$. The calculated detectivity is shown in Figure 2.12. The device's spectral detectivity ranges from 2120 cm $Hz^{1/2}$ W^{-1} at 1250 nm to 575 cm $Hz^{1/2}$ W^{-1} at 1350 nm. These values are low compared to commercial InGaAs detectors but are several orders of magnitude higher than other Si devices in this wavelength range.

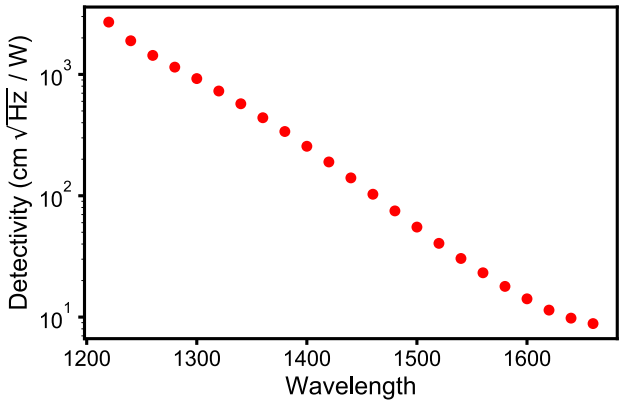

Figure 2.12: Detectivity as a function of wavelength for the 16 nm Pt device.

2.4.4 Imaging detector

The microscope setup for the transmission images in Figure 2.7 of the thesis are shown in Figure 2.13. Light from a Fianium supercontinuum source laser was fiber coupled to an acousto-optic tunable filter (AOTF), allowing for wavelength selection. The light was then reflected into a 60× objective lens (NA = 0.7) to focus the beam on the Au/quartz sample, which was mounted on a movable piezo scan stage. Transmitted light was collected by a 20× objective lens (NA = 0.4) and sent to the photodetector. The current generated by the photodetector was measured using an SR830 lock–in amplifier. The transmission maps were acquired with our 16 nm photodetector and compared under identical circumstances with a commercial silicon detector (Thorlabs SM1PD1A).

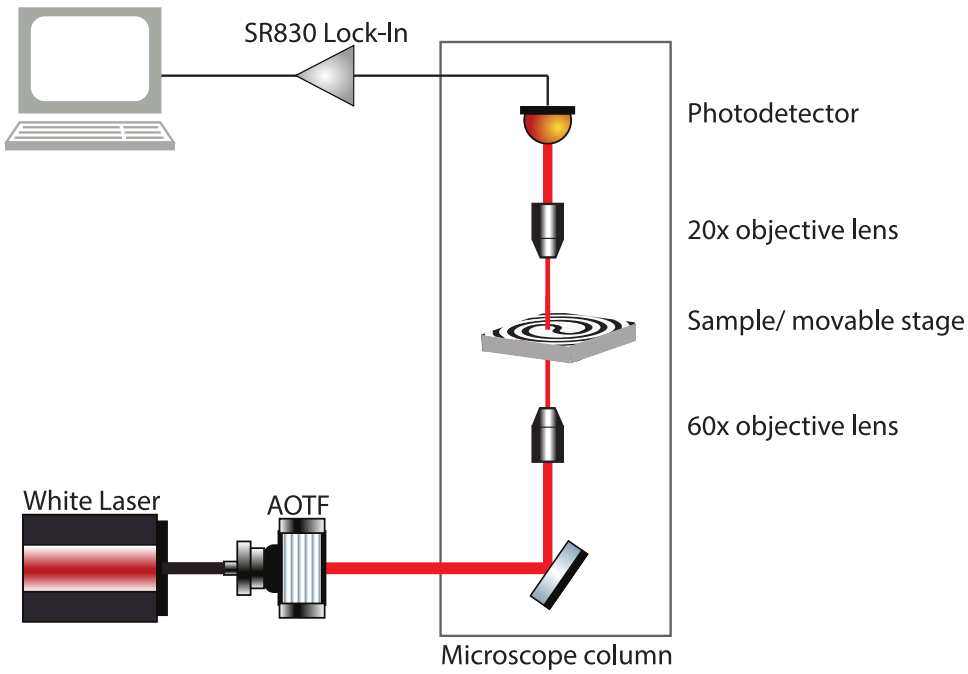

Figure 2.13: Microscope setup for images taken with imaging detectors.

2.5 Conclusions

In summary, we demonstrated hot carrier generation from NIR photon absorption (below the semiconductor bandgap) in ultrathin metal films, which represents an effective and low-cost solution to extend the bandwidth of semiconductor photodetectors and other optoelectronic devices. We have shown that by selecting materials with approximately equal real and imaginary parts of the refractive indices, such as Pt, Fe, Cr, and Ti, we can obtain nearly 80% absorption of broadband NIR light in a nanometer-scale planar metallic contact to Si. By contrast, traditional metals used for plasmonics and nanophotonics (e.g., Au, Ag, Cu, and Al) only allow for $\sim$ 20% optical absorption. We fabricated hot carrier near–IR photodetectors by depositing Pt on Si and obtained a 10^{-4} – 10^{-6} A/ W photore-

sponse at zero applied bias for wavelengths of 1.2 - 1.5 μm, respectively, based on 16 nm of metal. Further, we have demonstrated its room temperature operation as an imaging detector with superior performance (operation below the semiconductor bandgap) compared to commercial Si detectors. The simplicity of the geometry and fabrication makes this hot carrier device concept straightforward for incorporation into current commercial fabrication methods. These concepts could also be expanded to metal-insulator-metal hot carrier systems to improve visible and ultraviolet performance[51–53]. Further, the development of a Si–based NIR detector for on–chip applications will likely have a significant impact on both Si photonics and telecommunications devices, where NIR detection is difficult to achieve using a single semiconductor platform.

Chapter 3: Near-perfect absorption throughout the visible using ultrathin metal films on index-near-zero substrates

Generating optical interference in thin films is a versatile method of controlling light absorption, reflection, and transmission in materials. Such interference is responsible for the rainbow colors seen in oil on water and is incorporated into many devices for anti-reflection coatings[54, 55], optical filters[55–57], thin film solar energy conversion[58], and even lasers[59–61]. Traditional interference effects use a lossless material that is a half or a quarter of the thickness of the incident wavelength within the material for constructive or destructive interference, respectively. However, it was recently shown that lossy, reflecting materials can achieve destructive interference in film thicknesses much less than the quarter wavelength requirement as a result of accumulated phase shifts upon reflection from each interface[19, 62]. This resonance is a subwavelength Fabry–Pérot–like resonance and is unlike tradition Fabry–Pérot (FP) resonances because it requires the optical cavity to be both highly attenuating and 10–100× thinner than the wavelength of light to allow multiple reflections for destructive interference. This effect is unique because highly attenuating materials typically are also highly reflective and therefore are generally not considered useful as an optical cavity. This resonance has been applied to obtain

high absorption in ultrathin semiconductors on metal substrates such as silicon (Si) and germanium (Ge) on gold (Au) or silver (Ag)[19, 63], but can also be applied to metals with large refractive index, such as platinum (Pt) and chromium (Cr) on dielectric substrates (see Chapter 2).

Significant research has gone into design considerations for the absorption resonance in thin semiconductors on metal substrates[19, 35, 37, 63–66]; however, absorption resonances in planar, thin metal films has not been thoroughly investigated. Metals are more reflecting than semiconductors and are therefore commonly overlooked for efficient absorption. Rensberg et. al. [65] demonstrated that reflection can be suppressed in thin films when their substrates have a refractive index less than unity (*i.e.* $\tilde{n}_{substrate} = n_s + i\kappa_s < 1$). Low loss, index–near–zero (INZ) materials offer high optical contrast to most media, including air and therefore enhance the FP like resonance in the thin absorbing films. In this chapter, we present design considerations for obtaining near–perfect absorption in planar, thin metal films by varying the optical properties of nearly–ideal INZ substrates and incident optical wavelengths from near–ultraviolet (NUV) to near–infrared (NIR). As expected, we find that the absorption in the metal film decreases with increasing n_s, but we find that the absorption does not significantly decrease with increasing loss (κ_s). In addition, we find that metals commonly used for plasmonics, such as Au and Ag, can be used to obtain high absorption in NUV and visible wavelengths, while lower conductive metals such as Pt and Cr have high absorption over a broader range of wavelengths from visible to NIR.

3.1 Absorption resonance with an ideal INZ substrate

It was previously shown that the absorption in an ultrathin metal film can be estimated by the optical contrast of the media surrounding the film[33, 38, 67, 68]. If the surrounding media are optically thick and non–absorbing, the optical path length in the film is very small (*i.e.* $\delta = 2\pi d/\lambda \ll 1$, where d is the film thickness and λ is the wavelength in air), and the real and imaginary parts of the thin film's refractive index are approximately equal (i.e. $n_f \gg \kappa_f$, where n_f and κ_f are the real and imaginary parts of the refractive index of the metal film, respectively), then the maximum absorption attainable in a thin film is determined by:

$$A_{max} \approx \frac{n_{top}}{n_{top} + n_{bottom}}, \tag{3.1}$$

where n_{top} and n_{bot} are the real parts of the refractive indices of the media above and below the metal film respectively. From this approximation there are two methods of obtaining near–perfect absorption in a thin metal film. The first is to ensure that $n_{top} \gg n_{bot}$ (as shown in Chapter 2), and the second is to reduce n_{bot} to zero. In this chapter, we consider this second case.

Figure 3.1 shows the absorption resonance within the metal film at four wavelengths incident from air on a 5 nm thick film with refractive indices $n_f + \mathrm{i}\kappa_f$ on a nearly ideal INZ substrate (*i.e.* $n_{top} = n_{air} = 1$ and $\tilde{n}_{bot} = 0.01 + 0.01\mathrm{i}$). The absorption maximum for all wavelengths is 99%, which is correctly estimated by Eq. 3.1. While the value of the absorption maximum is independent of wavelength

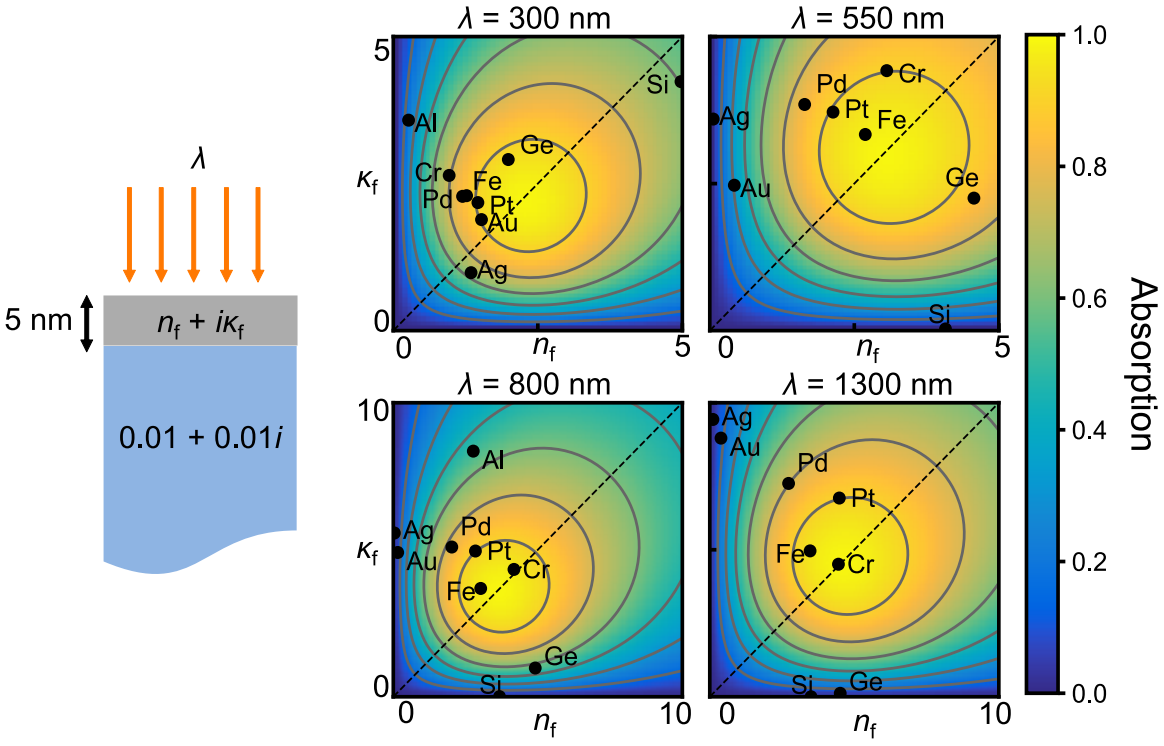

Figure 3.1: Absorption resonance in a 5 nm metal film varying the refractive index, n_f + iκ_f, for wavelengths 300, 550, 800 and 1300 nm. The black dots show the optical properties of various materials. The dotted line shows $n_f = \kappa_f$. The n_f and κ_f axes extend from 0 to 5 for wavelengths 300 and 550 nm and are increased from 0 to 10 for wavelengths 800 to 1300 nm due to the increased size of the resonance. Some metals do not show up in all plots because their refractive indices lie outside of the values shown.

and film thickness, the optical properties of the thin films that achieve the maximum absorption is dependent on these parameters. In Fig. 3.1, we see that the range of n_f and κ_f values that achieve ultra–high absorption decreases and moves closer to the origin with decreasing wavelength. Note that in the previous chapter we demonstrated that the resonance decreases in this same manner with increasing film thickness at a fixed wavelength (see Figure 2.2)[33]. The optical properties of various metals as well as Si and Ge are shown to determine what common materials will satisfy the absorption resonance. The optical properties were taken from references[40, 69–72].

Pt and Fe remain in the absorption resonance corresponding to $> 90\%$ absorption at all wavelengths, while Pd remains just outside the resonance maxima at $\sim$80% absorption. Cr lies in the absorption maxima for all but the shortest wavelengths, whereas Au and Ag only show high absorption for short wavelengths. At 300 nm, Ag lies outside the resonance but is close to the $n_f = \kappa_f$ line suggesting that it would lie at the center for the resonance for film thickness larger than 5 nm. Ge and Si are both close to the absorption resonance at 300 nm and Ge remains close to the absorption maxima at 550 nm. While Si is outside the resonance at 300 nm, it is close to the $n_f = \kappa_f$ line, suggesting that Si will lie at the center of the absorption resonance for films thinner than 5 nm. This behavior is because Si has higher loss and therefore higher dampening of the incident light compared to the other materials listed at $\lambda = 300$ nm. Therefore, to obtain multiple reflections within the film for destructive interference, the Si film must be thinner than the other materials (see Figure 3.2).

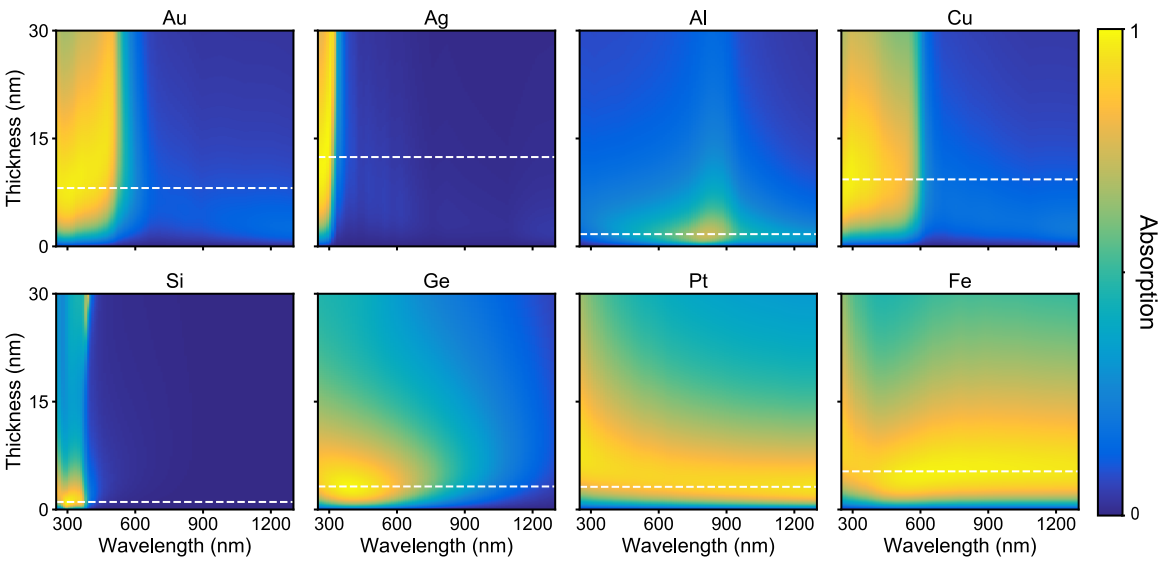

Figure 3.2: Contour plots of absorption as a function of wavelength and thickness for various materials on a nearly ideal INZ substrate ($\tilde{n}_{bot} = 0.01 + 0.01i$). The white dashed lines show the thickness where the absorption is maximized in each material. Al and Si achieve maximum absorption at 1–2 nm film thicknesses. Ge and Pt achieve maximum at 3 nm. All other metals achieve maximum absorption between 5 and 15 nm film thicknesses. Pt and Fe maintain high absorption across all wavelengths.

We verify the absorption resonance on a nearly ideal INZ substrate as a function of film thickness in eight materials in Figure 3.2. As expected, Ag achieves maximum absorption at a film thickness larger than that required for Au. The maximum absorption for each material is 97% for Au, 99% for Ag, 74% for Al, 98% for Cu, 99% Si, 99% for Ge, 96% for Pt and 98% for Fe. The film thicknesses and wavelengths at maximum absorption are, respectively, 8 nm and 320 nm for Au, 12 nm and 282 nm for Ag, 2 nm and 816 nm for Al, 9 nm and 284 nm for Cu, 1 nm and 295 nm for Si, 3 nm and 377 nm for Ge, 3 nm and 1300 nm for Pt and finally 5 nm and 653 nm for Fe.

3.2 Effect of non-ideal INZ optical properties

While Figure 3.1 shows the absorption resonance in thin films on a nearly ideal INZ substrate, real INZ materials generally have higher optical loss because of the free carrier dampening required to obtain a low refractive index. Therefore, it is important to understand how the resonance shifts with the varied optical properties of INZ substrates with optical loss. Figure 3.3 shows the changes in the location and value of the absorption maxima in n_f–κ_f space varying the INZ complex refractive index, $n_{INZ} + i\kappa_{INZ}$, for three values of the effective optical path length, $\delta = 2\pi d/\lambda$. Each data point was calculated numerically using the transfer matrix method. As expected, with decreasing δ, either due to decreasing thickness or increasing wavelength, the maximum absorption occurs at larger values of n_f and κ_f.

We find that the maximum absorption is predominately determined by the real part of the INZ material's refractive index, n_{INZ}, and remains relatively constant as the optical loss, κ_{INZ}, increases for constant n_{INZ}. The absorption maxima calculated using Eq. 3.1 for n_{INZ} values of 0.01, 0.4 and 0.8 are 99.0%, 71.4% and 55.6%, respectively, and the exact numerically calculated values in Figure 3.3 agree with these values within ± 4%. This result demonstrates that Eq. 3.1 can be used to estimate the value of the absorption maximum even in the presence of optical loss in the substrate. However, the values of n_f and κ_f that correspond to maximum absorption change significantly with the optical properties of the INZ substrate. As n_{INZ} increases, the maximum absorption occurs at larger values of n_f and κ_f, and

as κ_{INZ} increases, the location of the absorption maximum moves away from the $n_f = \kappa_f$ line and instead requires $n_f > \kappa_f$ (Figure 3.3).

As the absorption in the INZ substrate increases, *i.e.* as κ_{INZ} increases, the peak of the absorption resonance shifts to larger values of n_f and smaller values of κ_f, moving the high absorption region away from the optical properties of common metals as shown in Figure 3.1. However, metals that lie closer to the $n_f = \kappa_f$ line are likely to remain in the absorption resonance, provided that $\kappa_{INZ} < 1$. For example, at 300 nm incident wavelength, Au, Ag, and Pt will all remain in the absorption resonance for $\kappa_{INZ} < 1$, allowing them to obtain >90% absorption if $n_{INZ} \leq 0.11$ and their film thicknesses are optimized (i.e. $d \sim$5nm).

Currently, INZ materials with the lowest refractive index reported in literature have minimum $n_{INZ} \sim 0.2$, and it is important to note that there is only a small optical bandwidth where both n_{INZ} and κ_{INZ} remain low[73–78]. Due to the dispersive properties of INZ materials, at short wavelengths n_{INZ} is too large for high absorption while κ_{INZ} is approximately 0. At long wavelengths, n_{INZ} will decrease, but κ_{INZ} will increase and move the absorption resonance away from all common materials. Therefore, the optical bandwidth useful for maximizing absorption in thin metal films is around the wavelength where $n_{INZ} = \kappa_{INZ}$, or $\lambda_{n=\kappa}$. INZ materials such as Al:ZnO or In:SnO have recently been of great interest because of the ability to tune $\lambda_{n=\kappa}$ by varying deposition parameters such as doping and annealing temperatures[74, 75, 79, 80]. These materials have previously reported tunable $\lambda_{n=\kappa}$ in mid–IR wavelengths, but recently they have achieved $\lambda_{n=\kappa}$ in the NIR. For example, Kim *et al.* in ref [75] reports INZ optical properties in 2 wt%

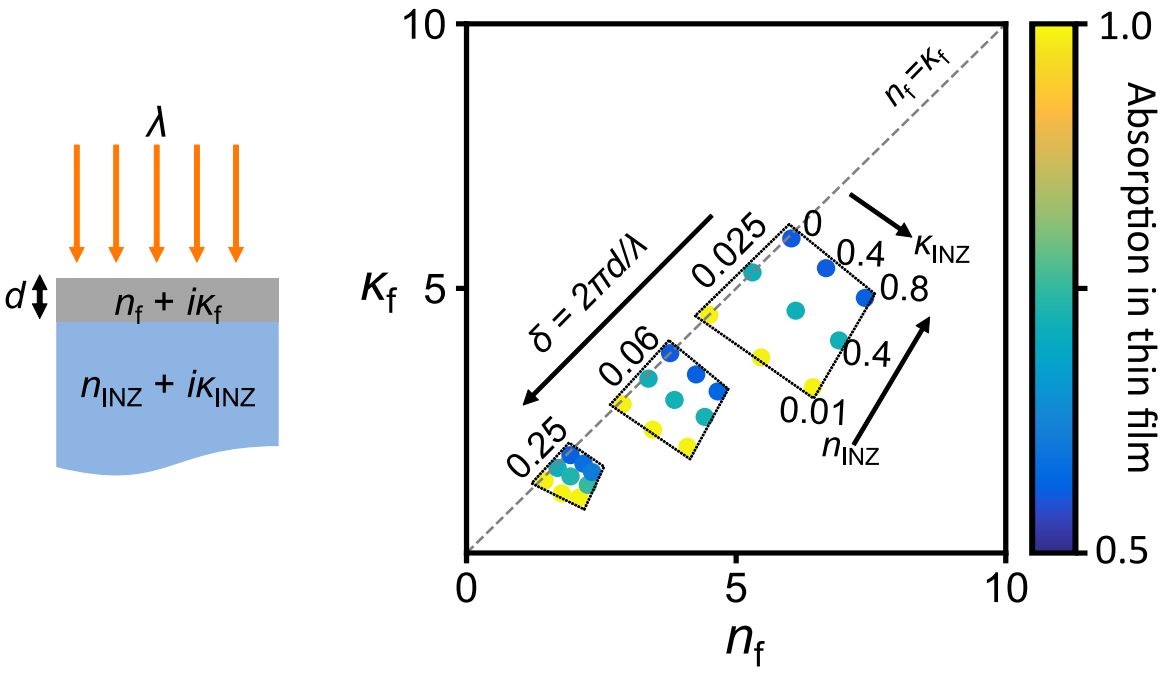

Figure 3.3: Absorption maxima in thin films are shown as a function of their optical properties (n_f + iκ_f), the optical properties of the INZ substrate (n_{INZ} + iκ_{INZ}), and of the effective optical path length, $\delta = 2\pi d/\lambda$. The color of the dots represents the value of the absorption maxima in the thin film as determined by the color bar. The dashed grey line corresponds to $n_f = \kappa_f$. The three boxed regions represent calculated values for δ = 0.25, 0.06, and 0.025 varying n_{INZ} and κ_{INZ}. The boxed region at $\delta = 0.025$ shows the values for n_{INZ} and κ_{INZ}, and this trend is consistent for all δ regions, but not shown for simplicity.

Al:ZnO with $\lambda_{n=\kappa}$ at 1290.5 nm. The optical properties at this wavelength are n_{INZ} = $\kappa_{INZ} \sim 0.39$. However, n_{INZ} reaches a minimum of ~ 0.2 with $\kappa_{INZ} > 1$ for $\lambda > 1435$ nm. Therefore, a thin metal film deposited on this substrate would reach an absorption maximum of 70-80% absorption for a narrow bandwidth between 1290 and 1435 nm.

3.3 Ultra-high absorption in common thin metal films

Figures 3.1 and 3.3 show that it is necessary for the INZ substrate to have small real and imaginary parts of its refractive index to enhance absorption in common metals. There are currently no reported INZ materials in visible wavelengths; however, designing materials to have INZ behavior in this region has been a topic of considerable interest in recent years. Assuming it will be possible to find an INZ material with low refractive index that is tunable to any wavelength, it would be useful to look at which common metals will benefit from the enhanced absorption resonance. The results in Chapter 2 show that Pt, Cr, Fe and Ti obtain high absorption from 1100 - 1600 nm. Here, we consider the absorption in various metals from 250 - 900 nm. Figure 3.4 shows the numerically calculated absorption in eight common metals on INZ substrates with nearly ideal INZ ($\tilde{n}_{bot}$ = 0.01 + 0.01i) and low loss values ($\tilde{n}_{bot}$ = 0.25 + 0.25i) for the optical properties assuming no dispersion in the INZ substrate. The film thicknesses are optimized at each wavelength. Because dispersion prevents real INZ materials from maintaining low loss and low refractive index over this large bandwidth, Figure 3.4 should be considered a refer-

ence for selecting materials with high absorption given an INZ substrate with $\lambda_{n=\kappa}$ between 250 and 900 nm. The absorption spectra for each metal on a real, dispersive INZ substrate would reach the maximum values plotted here only for a narrow bandwidth around $\lambda_{n=\kappa}$.

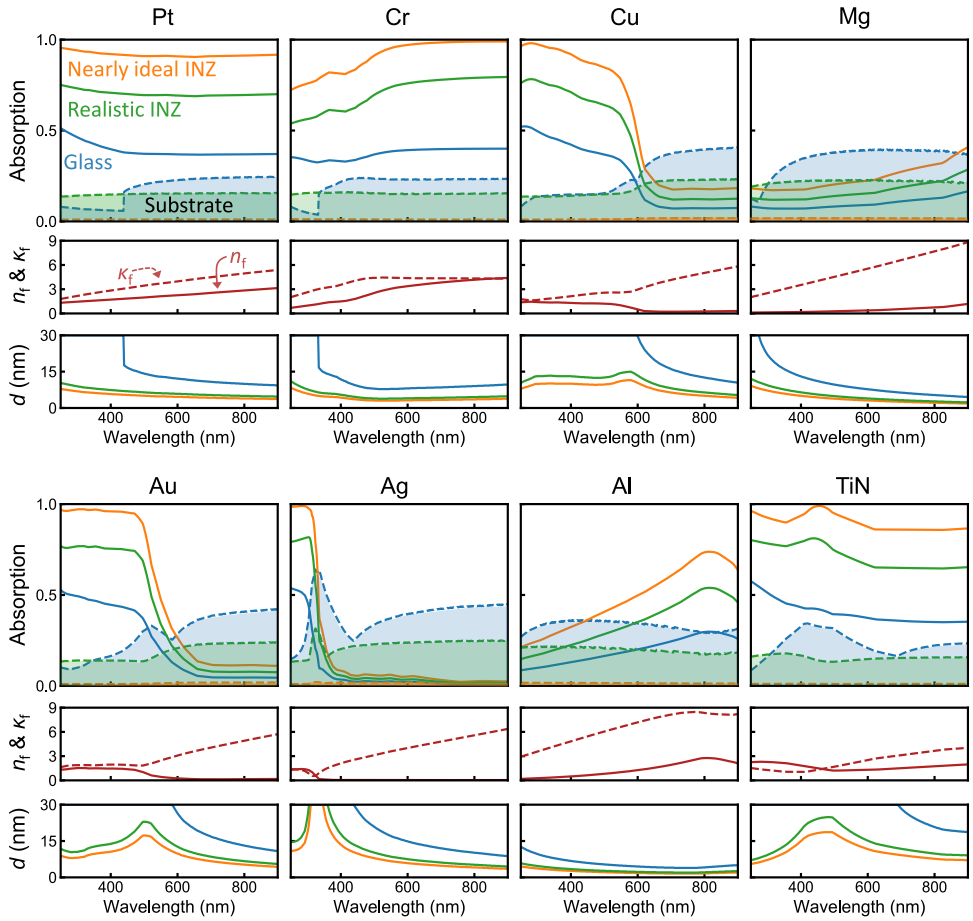

Figure 3.4: Maximized absorption in various thin film metals on a nearly ideal, non-dispersive INZ substrate (orange) with $\tilde{n}_{bot} = 0.01 + 0.01$i, a low loss, non-dispersive INZ substrate (green) with $\tilde{n}_{bot} = 0.25 + 0.25$i, and a glass substrate (blue). The refractive index, n_f (solid) + iκ_f (dashed), is plotted below the absorption. The transmission into the substrate is shown by the dashed lines and shaded regions. At each wavelength the film thickness, d, is optimized, and the optimized values are plotted.

Because Pt, Pd and TiN remain close to the $n_f = \kappa_f$ line, these metals are useful for high absorption throughout the NUV to NIR spectrum. Note that in-

creasing the difference between n_f and κ_f reduces the absorption in the thin film. For example, Mg will never have absorption larger than 30% because $\kappa_{Mg} \gg n_{Mg}$ at all wavelengths. Similarly, the absorption in Cr decreases for visible wavelengths where $\kappa_{Cr} > n_{Cr}$. The only metal that does not follow this trend is Al. This result is because n_{Al} becomes relatively large at ~800 nm, allowing it to lie just outside the absorption resonance for > 50% absorption, which can also be seen in Figure 3.1.

When the optimized film thickness is > 30 nm, the absorption is no longer maximized by the thin film FP resonance and instead is maximized by the bulk material absorption. Note that for a glass substrate, the optimized absorption is often from the bulk rather than the thin film resonance because of the reduced optical contrast. The absorption in Ag at ~350 nm is not due to a thin film FP resonance either, because at this wavelength Ag behaves more like a dielectric instead of a metal, and n_{Ag} and κ_{Ag} are too small to lie within the thin film absorption resonance.

While there is negligible transmission into the ideal INZ substrate for all metals, the maximum transmission into the lossy INZ substrate is 31% at the crossover wavelength for Ag. Because the INZ substrate is optically thick, it can be assumed that all light transmitted into the substrate will eventually be absorbed. However, the BK7 glass substrate has no absorption beyond 400 nm, and therefore most of the transmitted light will eventually exit the substrate into free space. Finally, we find that illumination with TM polarized light enables near angular independence of enhanced absorption in the metal film. Figure 3.5 shows the absorption in Pt, Au,

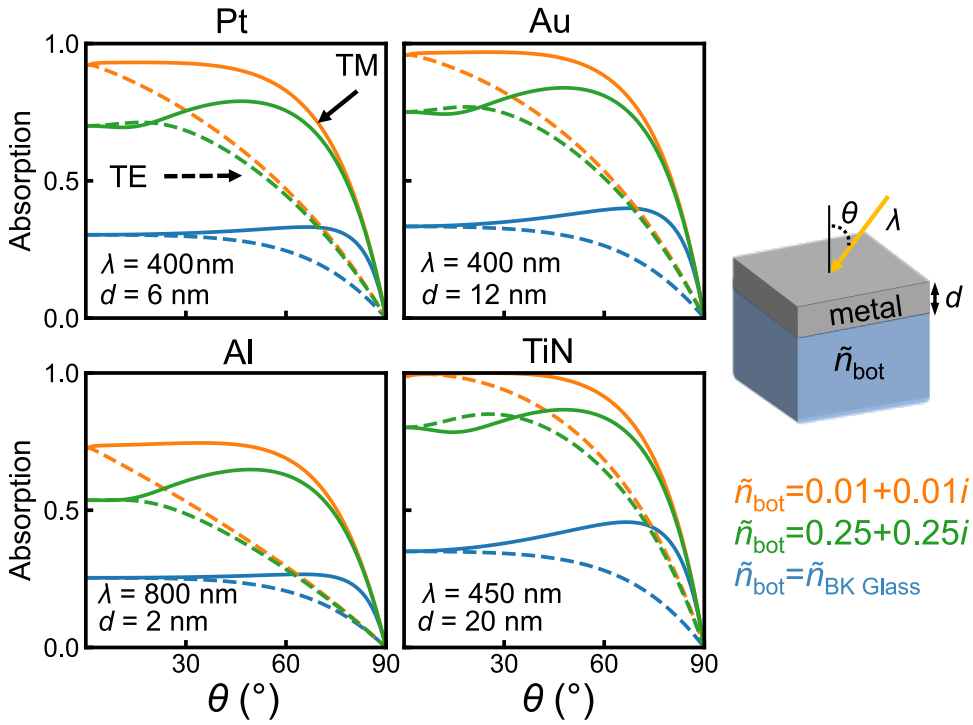

Figure 3.5: Absorption in four metals varying the incident angle for TM (solid) and TE (dashed) illumination. The absorption in each metal is compared when using a glass substrate (blue), a nearly ideal INZ substrate with $\tilde{n}_{bot}$ = 0.01 + 0.01i (orange), and a low loss INZ substrate with $\tilde{n}_{bot}$ = 0.25 + 0.25i (green). The absorption is calculated numerically using the transfer matrix method with the specified parameters for wavelength, λ, and film thickness, d, denoted within the plots. The film thickness and wavelengths were chosen to maximize the absorption.

Al and TiN, at wavelengths and film thicknesses chosen to maximize the absorption at normal incidence, varying the incident angle and polarization of illumination. For the nearly ideal INZ substrate with $\tilde{n}_{bot}$ = 0.01 + 0.01i and the glass substrate, the absorption with TM illumination remains constant until $\theta > 60°$. Interestingly, the metals on the INZ substrate with higher refractive index, $\tilde{n}_{bot}$ = 0.25 + 0.25i, increase in absorption for $\theta > 30°$ before decreasing at $\theta > 60°$. This is because the lossy INZ substrate will not have perfect reflection at the metal/INZ interface for normal incidence allowing some of the light to transmit into the INZ substrate. However, after the critical angle, the reflectivity at the metal/INZ interface will

increase and enhance the absorption within the thin metal film.

3.4 Conclusions

In conclusion, we have shown design considerations for obtaining nearly perfect absorption in ultrathin metal films on INZ substrates throughout the visible spectrum. Provided that the optical loss in the INZ substrate is low, the optimum thin film will have $n_f \sim \kappa_f$. However, as the optical loss in the INZ substrate increases, an optimum thin film would have $n_f > \kappa_f$. We find that while metals such as Pt, Cr, and Fe will have high absorption for NIR wavelengths, metals that are more commonly used for hot carrier and plasmonic devices such as Au and Ag can obtain high absorption in NUV and visible wavelengths. In addition, Al films as thin as 2 nm can have $> 50\%$ absorption on an INZ substrate at wavelengths near 800 nm. Presently, it is rare to find INZ materials in the visible to NIR wavelengths. Most INZ materials have INZ properties in NUV or mid–IR wavelengths. However, recently significant research has been done to fabricate bulk INZ materials or design metamaterials that act as effective INZ substrates in this wavelength region[75, 81, 82]. Further opportunities exist for tailoring the properties of the thin-film metals either through alloying[48] or dynamically switching their refractive indices in the visible[83]. Future work in materials design could enable ultra–high absorption throughout a wide spectral range for optoelectronic devices such as hot carrier detectors and energy convertors[49, 52], as well as color pixels and optical filters.

Chapter 4: Optoelectronic Devices on Index–near–Zero Substrates

Interest in materials with refractive index–near–zero (INZ) has exploded in the past few years as researchers have discovered novel applications for the semi–infinite wavelengths and phase velocities of electromagnetic waves within these materials. INZ materials allow electromagnetic waves to "squeeze" through narrow channels of arbitrary geometry[84, 85], funnel light through subwavelength apertures[86, 87], further metamaterial design parameters for cloaking technology[88], enhance optical nonlinear effects[73, 84, 89, 90], "pin" plasmonic resonances to a desired bandwidth[77], and enable coherent perfect absorption at nanoscale film thicknesses[91]. In particular, the unique optical properties of INZ materials may be useful for optoelectronic devices by increasing the absorption in quantum–well detectors[92], enhancing local electric fields for greater free carrier absorption for electro–optical modulation[93, 94], and coupling to metamaterial resonators for electrically tunable optical sensing[95]. While various optical effects of INZ materials have been explored, few optoelectronic devices have been fabricated to determine the combined optical and electrical impacts of INZ materials in the device design. In this chatper we experimentally demonstrate that INZ materials can enhance both optical and electrical performance in a hot carrier photodetector.

We designed a silicon–based, near–infrared (NIR) photodetector in which the photocurrent is generated within a thin metal film because of a Fabry–Pérot (FP)–like absorption resonance (see Chapter 2)[96], and we experimentally verify the absorption and photoresponse enhancement from an INZ substrate. To achieve INZ properties, a material must simultaneously be conductive and have low optical loss (*i.e.* low imaginary part of the permittivity)[65, 75]. INZ properties have been achieved in conductive materials where the real part of the permittivity transitions from positive to negative with low Drude damping. Feasible INZ materials include transparent conducting oxides whose carrier concentrations are suitable to achieve INZ behavior in NIR wavelengths by adjusting the metal doping concentration during deposition[73, 74, 77, 78]. For our device, we use Al:ZnO (AZO) as a low–loss INZ substrate.

A near–ideal INZ substrate with no loss (*i.e.* $n_{INZ} = 0.01$) allows for near–perfect absorption in FP–like resonant thin metal films, such as Pt (see Chapter 3 and reference [65]). Further, we find that low levels of optical loss in the INZ substrate do not significantly impact the maximum obtainable absorption allowing for high absorption using realistic materials. In this chapter, we experimentally determine both the absorption enhancement in ultrathin Pt films and the photoresponse enhancement in a Si/Pt Schottky photodiode resulting from the INZ properties of the AZO substrate.

4.1 Absorption in metal films using ideal and nonideal INZ substrates

In the previous chapters we demonstrated that a FP–like cavity can be made from planar absorbing films 10-100× thinner than the wavelength of incident light[19, 33]. The optical loss in the films gives rise to nontrivial interference allowing for broadband absorption determined by the optical properties of the surrounding media. This concept was applied to obtain high absorption in nanometer scale semiconductor films on metallic substrates[63, 66, 97] and in the previous chapters we showed that it can be adapted to metallic films on semiconducting substrates and exploited for hot carrier based photodetection[33, 98]. Provided that the real (n) and imaginary (κ) parts of a metal's refractive index are approximately equal (i.e., $n \sim \kappa$) and the optical path length within the thin film is significantly shorter than the optical wavelength in free space (*i.e.* $2\pi d/\lambda_0 \ll 1$, where d is the film thickness and λ_0 is the wavelength in free space), the absorption within a nanoscale metal film is determined by the optical properties of the surrounding materials[33]:

$$A_{max} \approx \frac{n_{top}}{n_{top} + n_{bot}}, \tag{4.1}$$

where n_{top} and n_{bot} are the real part of the refractive indices of the top and bottom layers, respectively.

According to eq 4.1, there are two methods of maximizing the absorption in a nanoscale metal film. The first is to ensure that $n_{top} \gg n_{bot}$. For example, when resonant films are illuminated with sub–bandgap light through silicon (*i.e.*

$n_{top} = n_{Si}$ and $n_{bot} = n_{air} = 1$), which has a refractive index of ∼3.5 in the NIR, it is possible to obtain ∼78% absorption in 15-30 nm films. The second method of maximizing absorption in a resonant film is to decrease the refractive index of the bottom material, such that n_{bot} approaches 0. In this case, A_{max} will approach 1 for any n_{top}. Here, we demonstrate this second method of maximizing absorption in a thin metal film with two examples of n_{top}: (i) $n_{top} = n_{air}$ and (ii) $n_{top} = n_{Si}$.

Figure 4.1 shows the FP–like absorption mechanism for both a traditional substrate ($n_{top} = n_{air}$) and one whose index approaches zero. The incident light undergoes multiple reflections within the thin film while being critically dampened, thus, requiring the film to be ultrathin. Upon partial reflection at each interface, the phase shifts accumulate to interfere with the initially reflected and transmitted waves, effectively reducing the overall reflectivity and transmittivity (Figure 4.1a). When an INZ substrate is used, the impedance mismatch at the metal/INZ interface increases. The high impedance mismatch both prevents any light from being transmitted into the INZ substrate and alters the phase accumulation of the partially reflected waves resulting in an increase of absorption within the metal film (Figure 4.1b). This absorption mechanism is the same for the case where $n_{top} = n_{Si}$; however, the initial reflection from the metal is reduced because of the lower impedance mismatch between silicon and the metal. Therefore, there is higher absorption for $n_{top} = n_{Si}$, even without the INZ substrate.

Pt, Cr, Ti, and Fe all satisfy the resonance conditions of eq 4.1 for high absorption (see Chapter 2), and thus, they are all good candidates for near–perfect absorption with an INZ substrate. Figure 4.1c,d shows that the calculated absorp-

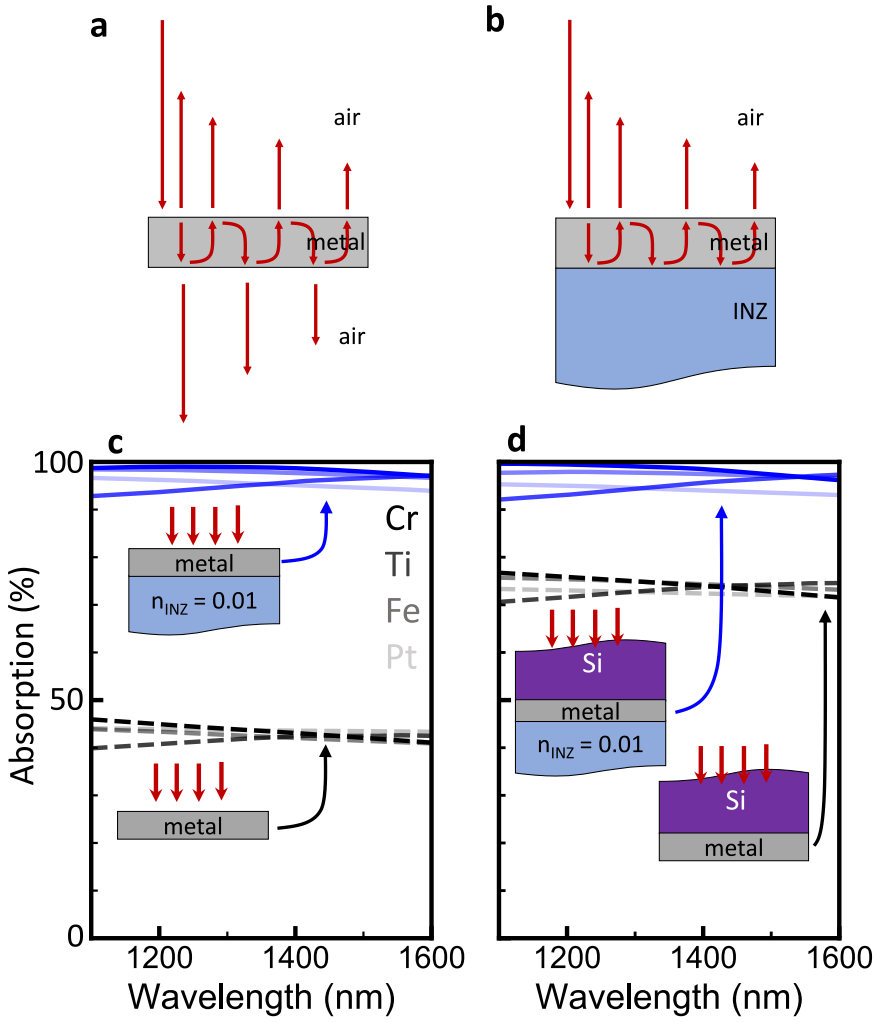

Figure 4.1: Near–perfect absorption in real metals on nearly ideal INZ substrates. (a) Absorption mechanism in a thin metal film suspended in air and (b) on an INZ substrate. The calculated absorption in thin film Cr, Ti, Fe and Pt illuminated from (c) air or (d) Si is near unity with an INZ substrate ($n = 0.01$). Solid and dashed lines are the absorption with and without the INZ substrate, respectively. The gradient in color depicts the different metals. The red arrows in the diagrams show illumination direction.

tion in these thin, resonant metals can be enhanced to near–perfect absorption with a no–loss INZ substrate ($n = 0.01 + 0\text{i}$). All absorption calculations in this manuscript were performed using the transfer matrix method[99], and the optical properties of the metals are obtained from refs [40, 41, 69] (see section A.2 for a description of the transfer matrix method). With light incident from free–space ($n_{top} = n_{air}$) and when an INZ substrate is used, the optimized metal film thicknesses for maximum absorption in Pt, Cr, Ti, and Fe are 3, 5, 6, and 6 nm, respectively. The INZ substrate enhances the absorption in the metal films by over a factor of 2 (Figure 4.1c). When light is incident from a higher index substrate ($n_{top} = n_{Si}$) rather than air, the ideal metal film thicknesses are slightly increased to 11, 16, 22, and 19 nm, respectively, and the absorption enhancement is ∼30% with the addition of the INZ substrate.

Even though we approach 100% absorption in metal thin films with a nearly ideal INZ substrate, there are few known low–loss materials that have a refractive index < 0.1. In addition, such low refractive index requires the presence of optical loss from free carrier dampening and, due to dispersion, there will only be a small spectral region where both the optical loss and the real part of the refractive index are relatively low. Therefore, for realistic device considerations, it is necessary to explore the absorption enhancement from physically relevant optical properties of more realistic INZ materials.

Figure 4.2 shows that the presence of optical loss in the INZ substrate does not significantly change the maximum absorption, but it does impact the thin film material properties that satisfy the resonance condition. The contour plots show the

numerically calculated absorption versus real and imaginary refractive indices of a 5 nm film on various INZ substrates (ranging from $\tilde{n}_{INZ} = 0.01 + 0.01$i to $\tilde{n}_{INZ} = 0.75 + 0.75$i), assuming illumination ($\lambda = 1300$ nm) through air (*i.e.* $n_{top} = n_{air}$). Both the thin film and INZ substrates have complex refractive indices labeled as $\tilde{n}_f = n_f + i\kappa_f$ and $\tilde{n}_{INZ} = n_{INZ} + i\kappa_{INZ}$, respectively.

For low n_{INZ} and κ_{INZ}, metals such as Cr, Fe, Ti, Pt, and V all lie within the absorption resonance. However, as κ_{INZ} increases (*i.e.* the INZ material becomes lossy) the absorption resonances move to larger n_f, shifting away from the metals listed. Interestingly, the value of the maximum absorption is independent of κ_{INZ}; instead, it is mainly dependent on n_{INZ}. As n_{INZ} increases, the maximum absorption decreases. When illumination is incident from a high index material, such as silicon, the effects of n_{INZ} and κ_{INZ} on absorption are similar (Figure 4.3). Further, using the optical properties of real metals (Cr, Fe, Ti, and Pt) and INZ materials (ITO, AZO, and GZO) from literature[73–78], we calculate that the thin film absorption can surpass ∼75% when illuminated through air and ∼90% when illuminated through silicon (see Figures 4.4 and 4.5).

4.2 Measured absorption in metal films on INZ substrates

We experimentally demonstrate the absorption enhancement in thin Pt films using a thick (>500 nm) AZO INZ substrate that was deposited using pulsed laser deposition both on glass and silicon substrates. A 2 cm × 2 cm silicon substrate was prepared with Al ohmic contacts and a 190 ± 5 nm Al_2O_3 antireflection coating on

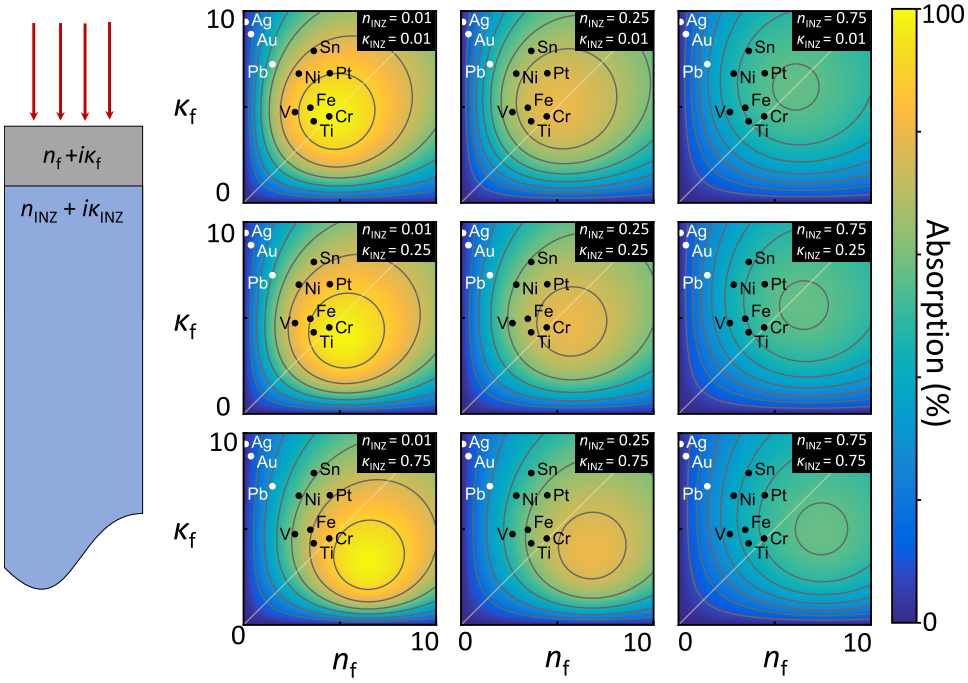

Figure 4.2: Effect of nonideal INZ on the absorption resonance. Numerically calculated absorption in a thin film ($n_f + i\kappa_f$) on an INZ substrate with $n_{INZ} + i\kappa_{INZ}$. The film is illuminated from air (see schematic). The diagonal line in each plot is the $n_f = \kappa_f$ line. Absorption is calculated for normal incidence at $\lambda = 1300$ nm for 5 nm thick films. Maximum absorption moves to higher n_f as κ_{INZ} increases, and the value of maximum absorption decreases with increasing n_{INZ}. The closed circles depict the optical indices of real materials, showing that the absorption peak moves away from common metals (toward higher n_f and lower κ_f) when there is high optical loss in the INZ material.

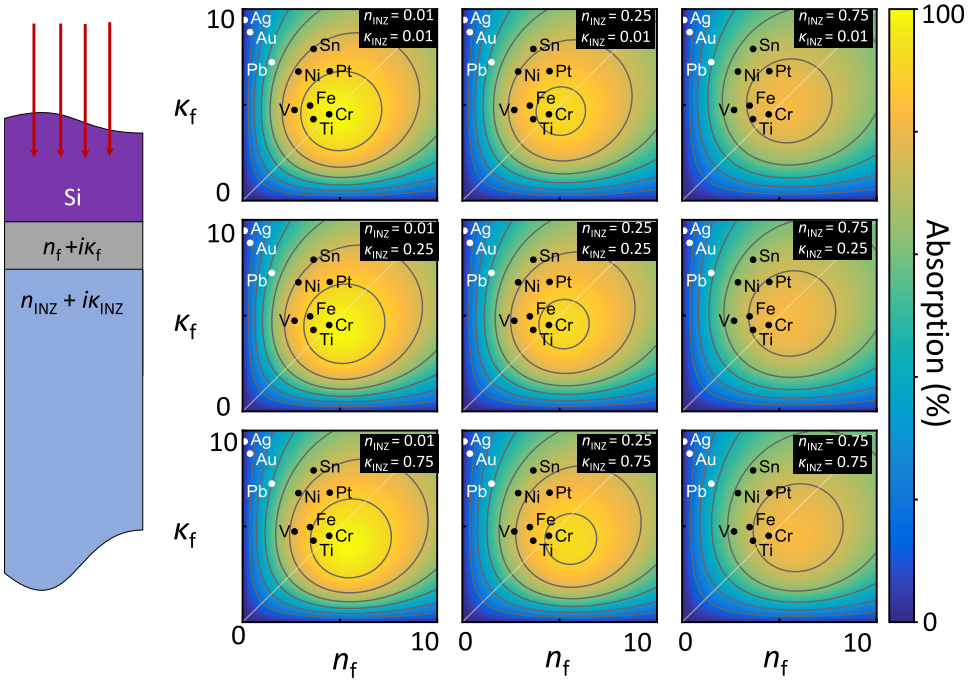

Figure 4.3: Effect of nonideal INZ on the absorption resonance when $n_{top} = n_{Si}$. The metal film ($n_f + i\kappa_f$) on an INZ substrate ($n_{INZ} + i\kappa_{INZ}$) is illuminated through silicon, and the absorption is determined within the thin film. The diagonal line in each contour plot corresponds to $n_f = \kappa_f$. Absorption is calculated for 17 nm thick films at normal incidence with $\lambda = 1300$ nm. The maximum absorption moves to higher n_f as κ_{INZ} increases, and the value of maximum absorption decreases with increasing n_{INZ}. The dots represent the optical indices of real materials showing that the absorption peak moves away from common materials for high optical loss in the INZ material.

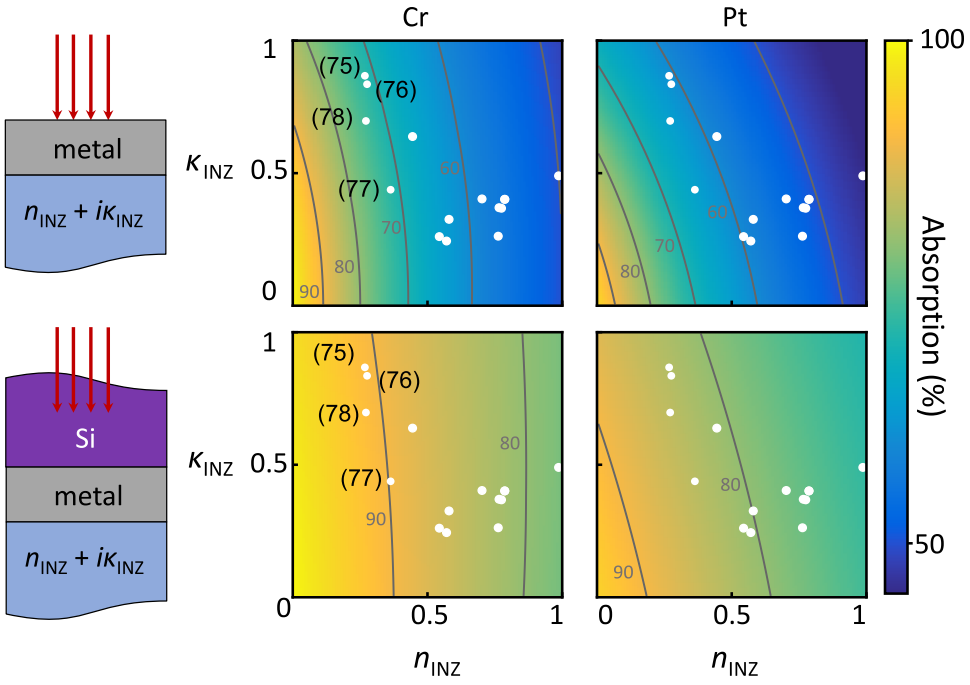

Figure 4.4: Optical design considerations for INZ materials to enhance absorption in Pt and Cr. The grey contour lines show increments of 10% absorption with the line closest to the origin showing 90% absorption. Refractive indices of INZ materials at $\lambda = 1300$ nm from literature are shown by the white dots[73–78]. Of these materials, the absorption at $\lambda = 1300$ nm is maximized by ITO from reference [78], GZO from reference [76], AZO from reference [77] and GZO from reference [75]. When deposited on these substrates, the calculated absorption in thin film Cr and Pt is >70% and >60% when illuminated through air and ≥90% and >84% when illuminated through silicon, respectively. The absorption within the metal is calculated for optimized film thickness at each data point. For illumination through air, the optimized thicknesses ranged from 4 to 12 nm for Cr and 3 to 7 nm for Pt. The 90% absorption contour line for Cr and Pt intersects the n_{INZ} axis at 0.11 and 0.07 and intersects the κ_{INZ} axis at 0.65 and 0.24, respectively. For illumination through silicon, the optimized thicknesses ranged from 17 to 25 nm for Cr and from 11 to 14 nm for Pt. The 90% absorption contour line for Cr and Pt intersects the n_{INZ} axis at 0.38 and 0.19, respectively. For Cr, the 90% absorption contour line does not intersect with the κ_{INZ} axis in this range, however, for Pt, the line intersects the κ_{INZ} axis at 0.66.

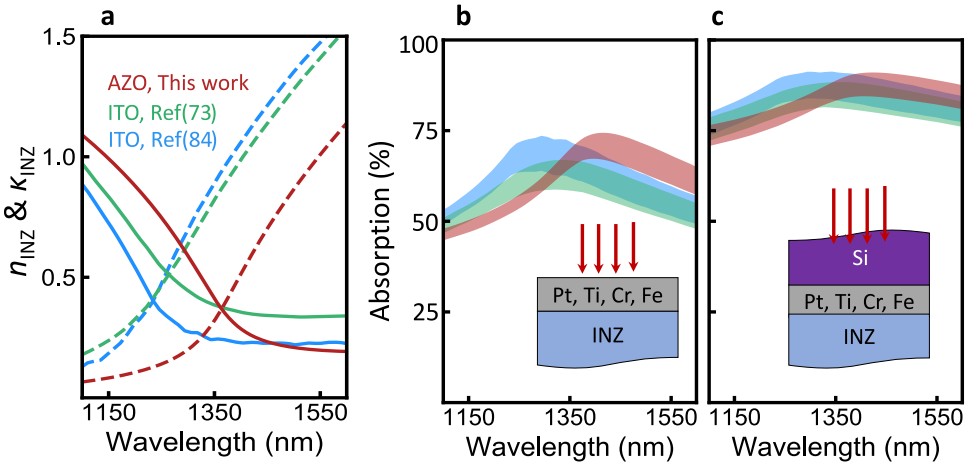

Figure 4.5: Absorption in Pt, Ti, Cr, and Fe on INZ substrates with optical properties found in literature. (a) Optical properties for ITO from reference [84] (blue), ITO from reference [73] (green), and the AZO fabricated for this paper (red). Absorption in Pt, Ti, Cr and Fe was calculated, and the range of absorption obtained using these four metals is shown for (b) illumination from air ($n_{top} = n_{air}$) and (c) illumination from silicon ($n_{top} = n_{Si}$). The shaded regions span the calculated absorption maximized for film thickness in all four metals when placed on the three examples of INZ materials from literature. These metals obtain ~75% absorption on INZ substrates when illuminated through air and ~90% when illuminated through silicon. The absorption reaches maximum at a wavelength 50–70 nm longer than $\lambda_{n=\kappa}$ (*i.e.* the wavelength where $n_{INZ} = \kappa_{INZ}$) and then decreases because κ_{INZ} increases and moves the absorption resonance away from the optical properties of the thin metal films. As expected, the ITO with larger n_{INZ} has lower absorption.

the top surface and Pt was deposited over the entire back surface. Part of the wafer was covered during the AZO deposition so the measurements with and without AZO were made on the same wafer, changing only the area of illumination (see Figure 4.6c for an image of the device).

To characterize the optical properties of AZO on the n–type Si/Pt wafer, we deposited AZO on a separate, bare Si substrate using identical deposition parameters. For absorption calculations, the AZO on Si was assumed to have the same properties as that deposited on the Si/Pt substrate. The thickness and refractive indices of the AZO were determined from ellipsometry fits using a general oscillator model, incorporating both Tauc-Lorentz and Drude models (Figure 4.6d,b). The AZO deposition created a thickness gradient, and the optical properties are dependent on the film thickness [100]. However, we found that the AZO thickness changes do not significantly impact the absorption within the Pt other than to shift the wavelength of maximum absorption because of the changes in the refractive indices of the AZO. Therefore, for the purposes of this work, we only consider the maximum thickness of the AZO on each device (note: the large area size and relative thickness uniformity of the maximum thickness regions allowed for easy laser alignment for absorption and responsivity measurements). After determining the optical properties of the AZO on glass, 5 ± 1 nm of Pt was deposited onto the AZO (note: for the Si substrates, 21 ± 2 nm of Pt was used to achieve the resonance condition).

The measured and calculated absorption of these devices shows a strong enhancement resulting from the INZ substrate (Figure 4.7). Note that the calculated

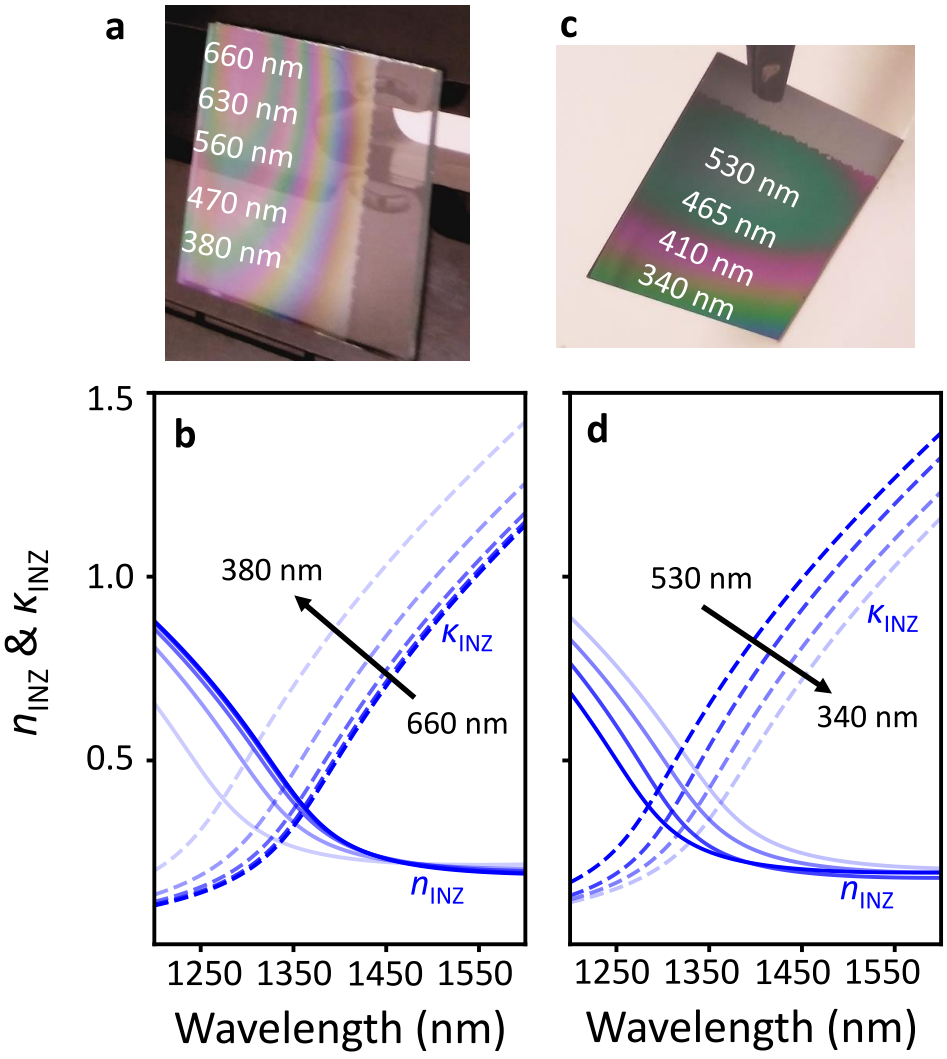

Figure 4.6: AZO has index–near–zero behavior. Images of AZO deposited on (a) glass and (c) silicon show the thickness gradient on each substrate. The real (solid lines) and imaginary (dashed lines) refractive indices of all thicknesses of AZO on (b) glass and (d) silicon as determined from ellipsometry analysis. $\lambda_{n=\kappa}$ is blue shifted for decreasing thickness on glass and red shifted on silicon.

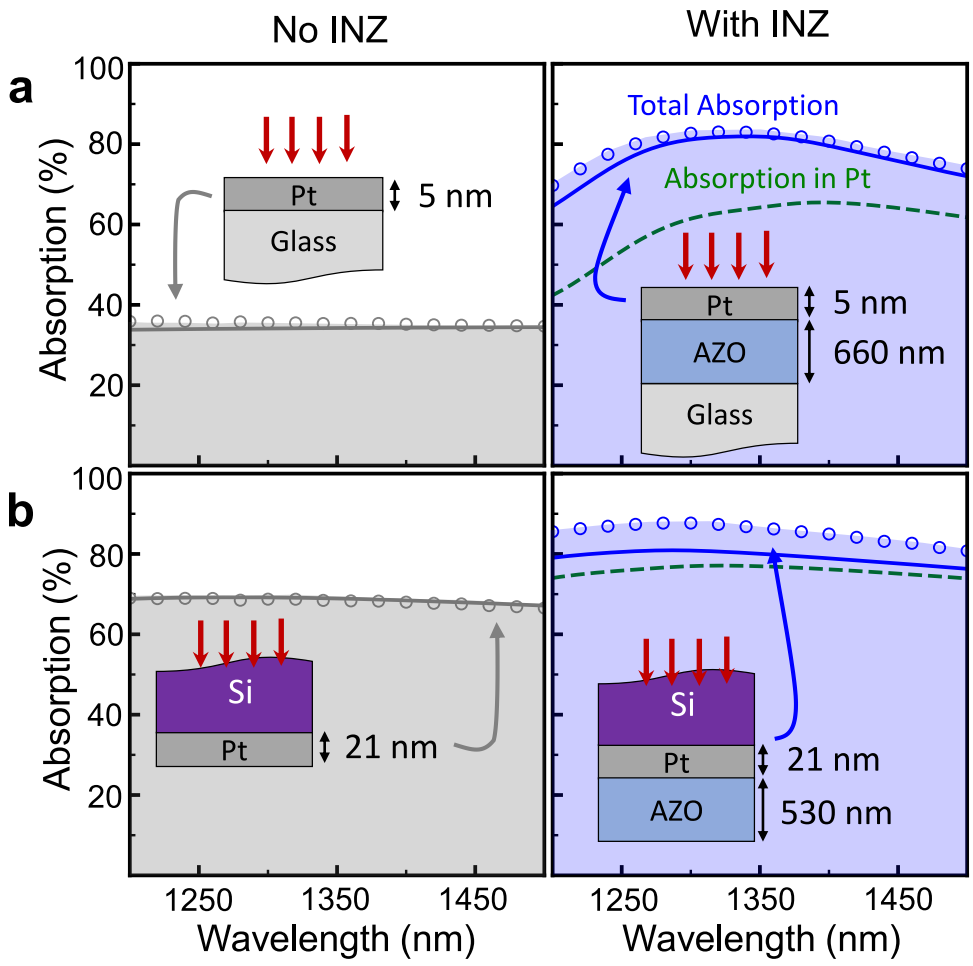

Figure 4.7: Measured (circles) and calculated (lines) absorption enhancement resulting from an index–near–zero substrate. Total absorption in thin film Pt without (left) and with (right) AZO when illuminated from (a) air and (b) silicon. The green dashed lines show absorption expected in only the Pt.

absorption includes the reflection loss from the antireflection coating on the top of the silicon surface. The experimental data (open circles) agree well with the calculated results for the total absorption in the devices both with AZO (blue solid lines) and without AZO (gray solid lines). The green dashed lines represent the calculated absorption within only the Pt for samples with AZO (note: both the glass and Si are transparent to NIR illumination). On average, AZO enhances the total absorption for the thin film Pt on glass by over a factor of 2 and by 26% for the Si/Pt photodiode.

For the sample illuminated from air, the calculations accurately determined the measurement results. However, the measured and calculated results for the n–Si/Pt photodiode have an absolute difference of ∼5% with higher measured absorption. This is likely due to slight differences in the AZO when deposited on Pt. Nevertheless, there is a clear enhancement in absorption within the Pt.

4.3 Enhanced hot electron photodetection with an INZ substrate

Photon absorption within the Pt film can lead to hot carrier generation and injection across the Si/Pt barrier, resulting in photocurrent. NIR radiation passes through the silicon wafer and is absorbed by the Pt contact (Figure 4.7a). The absorbed photons excite hot electrons, which travel to the interface and are injected into the silicon if it has energy larger than the Schottky barrier. The electrons then travel to the Al contact (which only covers a small region of the top surface) and are collected. Likewise, holes are collected through the Pt contact. Because the diodes

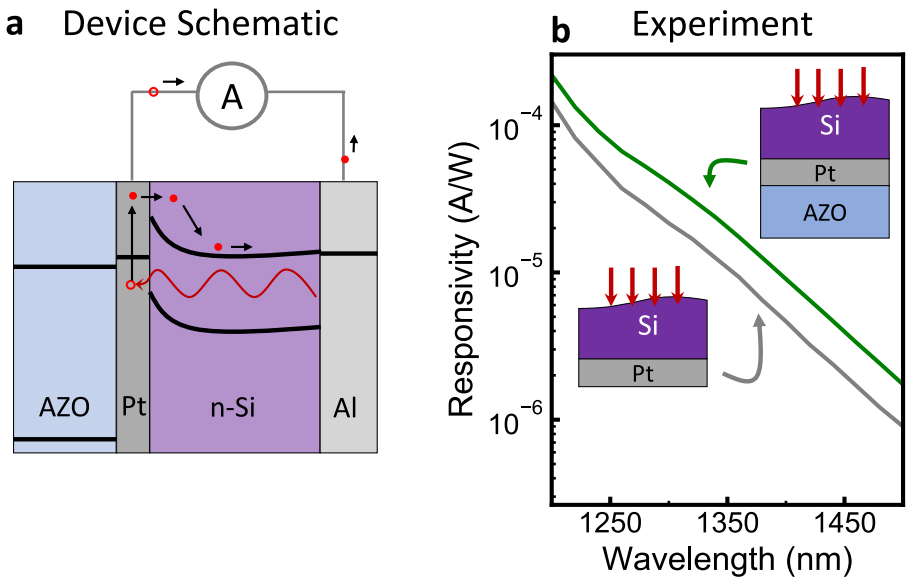

Figure 4.8: Enhanced hot carrier photocurrent with an index–near–zero substrate. (a) Schematic shows the photoresponse mechanism and band diagram for the Pt Schottky junction device. An absorbed photon excites a hot electron. The electron is injected into the silicon and collected through the ohmic Al contact. The hole is collected through the Pt contact. (b) Measured responsivity of the photodiode with (green) and without (gray) AZO. The photoresponse with the AZO is enhanced by >80%.

with and without AZO are on the same device, both measurements use the same contacts for consistency.

While the addition of an AZO layer to the back of the n–Si/ Pt photodiode increases the absorption by 26%, the responsivity is enhanced by >80% (see Figure 4.8b), showing that the AZO layer is also affecting transport and carrier collection. The probability that a photoexcited electron will be collected is given by the internal quantum efficiency (IQE):

$$IQE(h\nu) = A(h\nu)\eta_t(h\nu)Y_f(h\nu), \tag{4.2}$$

where A is the absorption at photon energy $h\nu$, η_t is the probability that the hot

electron will reach the Schottky interface, and Y_f is the probability that the electron will have enough energy to traverse the barrier into the silicon substrate once it reaches the interface. Y_f is known as the Fowler emission probability and is often calculated using a modified version of the Fowler yield equation:

$$Y_f = C_f \frac{(h\nu - \Phi_B)^2}{h\nu}, \tag{4.3}$$

where C_f is the Fowler coefficient and Φ_B is the Schottky barrier height. η_t is dependent on factors such as electron mean free path, film thickness, and probability of multiple reflections from the film interfaces. C_f is a constant dependent on device geometry and Fermi energy. Therefore, the IQE is proportional to $(h\nu - \Phi_B)^2$ and can be used to determine the barrier height (Figure 4.9a), resulting in $\Phi_B = 0.84 \pm 0.01$ eV for both devices with and without the AZO.

A second method is also used to determine the barrier height from the forward current-voltage characteristic using thermionic emission theory, which results in a barrier height of 0.7 eV and an ideality factor of 3.56 (Figure 4.10)[101, 102]. This discrepancy between these two methods (and large ideality factor) along with the reduced barrier height from the expected 0.9 eV for a Pt/n–Si junction suggests that there is an interfacial region of PtSi and Pt_2Si reducing the quality of the junction and, hence, the responsivity[102]. However, the photodiodes with and without AZO will have the same interface because they were fabricated simultaneously on the same substrate. The consistency of the Schottky junctions is verified by their shared measured barrier height in Figure 4.9a.

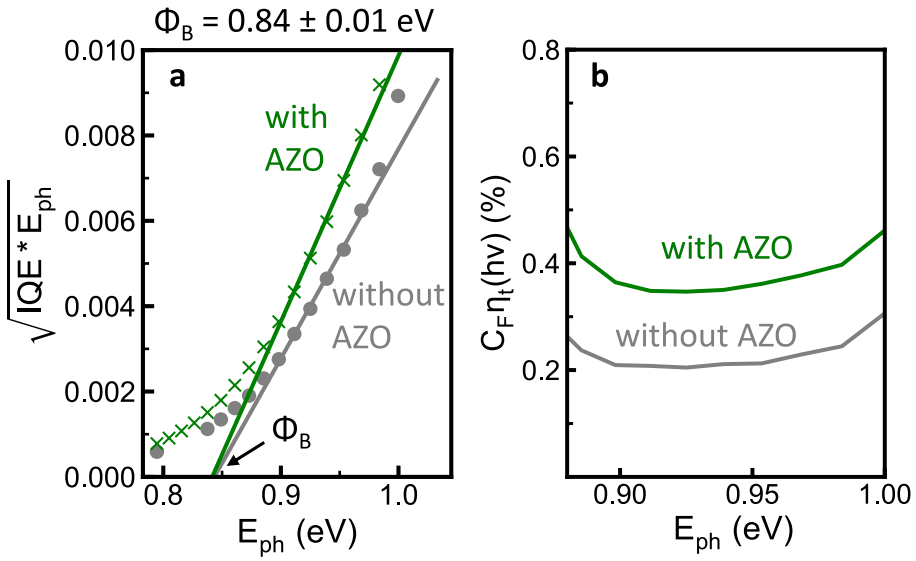

Figure 4.9: Barrier height and transport probability of the Si/Pt photodiode with and without AZO. (a) A barrier height of 0.84 ± 0.01 eV was determined from the linear fit to the Fowler yield (*i.e.*, the square root of internal quantum efficiency). (b) The AZO contact nearly doubles the carrier transport probability.

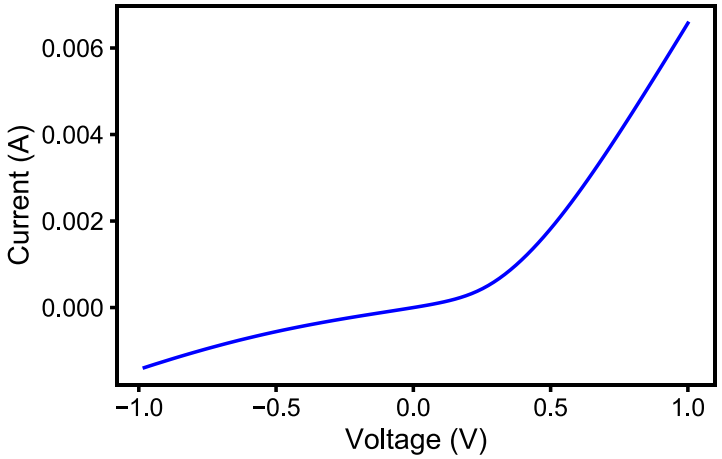

Figure 4.10: Current–voltage relationship for the Si/Pt photodiode. The data was recorded using a Keithley 2400 source meter with a LabView script that swept voltage and read current and resistance. The barrier height extracted from the forward bias region using thermionic emission theory is 0.7 eV with an ideality factor of 3.56. This result suggests that there is a PtSi or Pt_2Si region at the interface reducing the quality of the junction.

We also extract $C_f \times \eta_t(h\nu)$ from the IQE characteristic and find that AZO enhances the probability that electrons will reach the Pt/n–Si Schottky interface by ∼70% on average (Figure 4.9b). Because the Pt film is very thin, the improved transport probability is likely due to a decrease in electron energy loss after reflection from the Pt/AZO interface. The carrier mean free path (MFP) in Pt is expected to be 10-20 nm[42, 103–105]; therefore, our Pt film thickness is approximately equal to the MFP. Without the AZO, the carriers generated closer to the back of the Pt film are unlikely to reach the Si/Pt interface if they lose energy after scattering from absorbates or other contaminants at the Pt/air interface. However, with enhanced elastic scattering from the AZO Schottky barrier, carriers generated at the back of the film are more likely to reach the Si/Pt interface and traverse the barrier, effectively increasing the carrier transport probability[11]. We used heterodyne Kelvin probe force microscopy (H–KPFM) to determine the work function difference between the two materials[106], and we find that AZO has 131 ± 75 mV larger work function than Pt (Figure 4.11). Additional work will be needed to determine the long–term stability of this effect, as the Pt will likely diffuse into the AZO over time[107].

4.4 Methods

This section describes the fabrication, experimental and calculation details for the data displayed in this chapter.

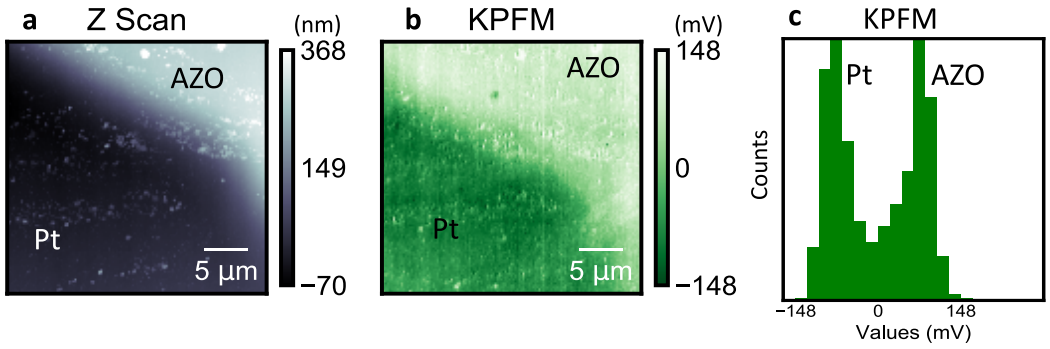

Figure 4.11: Kelvin probe force microscopy scan of Pt and AZO edge. (a) Topography and, (b) work function difference between Pt and AZO. Using a Pt probe, the work function was measured using the H–KPFM method. (c) The histogram of the H–KPFM data showing a 131 ± 75 mV work function difference between Pt and AZO.

4.4.1 Sample fabrication

The platinum/n–type silicon photodiode was fabricated on a 370 μm thick, double–side polished, $< 100 >$ n–type silicon wafer (<1 Ω·cm). Wafers were cleaned in a piranha etch (3:1 sulfuric acid (H_2SO_4) and hydrogen peroxide (H_2O_2)) to remove all organic material, a buffered oxide etch (BOE) to remove the native oxide, and dried under a N_2 stream. Immediately after the cleaning procedure, ohmic contacts were formed by depositing aluminum (Al) through a shadow mask in a thin strip along the top surface of each device, which was annealed at 425 °C in a forming gas of 96% Ar and 4% H_2. A ∼190 nm Al_2O_3 antireflection coating was then deposited using atomic layer deposition, keeping the Al uncoated to enable electrical connection to the device. The native oxide was removed from the back surface of the Si with BOE, and 21 nm of Pt was deposited using an Angstrom electron beam evaporator at a deposition rate of ∼1.4 $\mathring{A}$ s^{-1} and a base pressure of $\sim 2 \times 10^{-6}$ Torr. Finally, 530 nm of AZO was deposited over ∼80% of the Pt area using pulsed

laser deposition. The 2 wt % AZO target were purchased from the Kurt J. Lesker Corp. with purities of 99.99% or higher. The energy density of the laser beam at the target surface was maintained at 1.0 J/cm^2 and the substrate temperature was 400 °C. For illumination from air, 660 nm of AZO was deposited on a standard glass microscope slide using pulsed laser deposition. After optical characterization, 5 nm of Pt was deposited over the top of the AZO using an Angstrom electron beam evaporator at a deposition rate of $\sim$1 $\mathring{A}$ s^{-1} at a base pressure of $\sim$3.7 $\times 10^{-6}$ Torr.

4.4.2 Material characterization

During each Pt deposition, a microscope slide was included in the deposition to determine the thickness and refractive index of the deposited metal. All material refractive indices and thicknesses were determined using a J. A. Woollam M–2000D Spectroscopic Ellipsometer, 8 in. (190-1690 nm).

4.4.3 Optical and electrical measurements

Absorption measurements were performed using a 6 in. integrating sphere (Labsphere RTC–060) with illumination at near–normal incidence of 12°. Two Ge photodiodes were used to measure the light intensity inside the integrating sphere and to monitor power fluctuations of the incident beam. Specific NIR wavelengths were selected from a supercontinuum source (Fianium WhiteLase) using an acousto–optic tunable filter (AOTF), and the incident light was chopped using a rotating disk chopper. The signals from the photodiodes were measured using a SR830 lock–

in amplifier with the reference frequency matched to the frequency of the optical chopper. The uncertainty of the measured absorption is ±0.5%. To determine the responsivity of the fabricated photodiode, the sample was mounted on a vertical stage with copper probes forming electrical contact to the Al ohmic and Pt contacts. The incident light was focused on the sample at normal incidence and the power incident on the sample was determined by a calibrated InGaAs photodiode. The incident power was on the order of 1 μW for all wavelengths. The signals from the sample and each photodiode were measured using a SR830 lock–in amplifier with the reference frequency matched to the frequency of the optical chopper. There is a 2-3% uncertainty in the measured responsivity.

4.4.4 Optical calculations

The theoretical absorption was calculated for near-normal incidence, that is, ∼12°, using the transfer matrix method assuming that the glass and silicon substrates are infinite. To account for the incident reflection from the air/Al_2O_3/silicon interface, the calculated total absorption for the Si/Pt device was corrected to accurately describe the measured absorption using $A_T^{cor} = A_T - R_{ARC}$ where A_T^{cor} is the corrected total absorption, A_T is the total uncorrected absorption of the device assuming illumination through infinitely thick silicon, and R_{ARC} is the reflection from the Al_2O_3 antireflection coating (ARC). R_{ARC} is determined from optical properties of Al_2O_3 measured using ellipsometry. The calculated absorption within the Pt when there is an AZO back contact (green dotted line in Figure 4.7b) is also corrected for

the initial reflection loss using the following equation: $A_{Pt}^{cor} = \frac{A_{Pt}}{A_T} \times A_T^{cor}$, where A_{Pt}^{cor} is the absorption in the thin film Pt corrected for reflection from the ARC coating and A_{Pt} is the uncorrected absorption in Pt calculated with the assumption that it is illuminated through infinitely thick silicon.

4.4.5 KPFM measurements

The heterodyne Kelvin probe force microscopy measurements were performed using a Cypher atomic force microscope with a CSC37/Pt probe. An AC voltage of 3 V was applied to generate a potential difference between the probe and the sample's surface at a frequency of 226.97 kHz. The frequencies at which the H–KPFM signal was detected and the probe was oscillated to control the topography are 195.9 kHz and 31.075 kHz, respectively.

4.5 Conclusion

In summary, we have demonstrated that materials with refractive index–near–zero enhance the subwavelength FP–like resonance in ultrathin metallic films and can lead to increased hot carrier photocurrent. We experimentally verify a $> 2\times$ absorption enhancement in Pt relative to a glass substrate and a 26% increase relative to a Si/Pt photodiode. We also found that the electrical response of the photodiode is enhanced by >80% due to a combination of increased absorption and improved carrier transport. To further enhance the responsivity of silicon–based, NIR hot carrier photodiodes, the diodes should be fabricated with significantly smaller sur-

face area with consideration of edge effects by doping the silicon around the active area with a p–type dopant[108]. Reducing the temperature of the Pt and AZO deposition will also reduce the diffusion of the Pt into the silicon, improving the diode IV characteristics. Finding metals with similar optical properties to Pt, but with a longer mean free path would additionally enhance the photoresponse because of the increased probability of carrier collection after multiple reflections. Further, metals with appropriately chosen or tailored density of electron states can also improve hot carrier generation prior to transport and result in further photocurrent enhancements[49].

Finally, this work further elucidates the physical mechanisms involved in enhancing the device response, which are important for optimal photodiode design. In addition to silicon–based diodes, the $> 2\times$ enhancement in the Pt absorption on an AZO substrate illuminated from air suggests that it may be possible to design high efficiency metal-insulator-metal (MIM) NIR detectors with Pt and AZO. The high absorption also requires significantly thinner Pt (4 nm as opposed to 17-20 nm) for the Si device. Therefore, an MIM device is likely to have higher emission probability after multiple hot carrier reflections because of the dual purposed (improved absorption and carrier transport) effects of the AZO layer[52].

Chapter 5: Near–infrared photoresponse from ultrathin AgAu alloyed films

While the material properties of pure metals are well understood and characterized, they are not necessarily ideal for certain applications, and the ability to tune the mechanical strength, conductivity, and optical response is important for many technologies. For example, absorbing metal contacts at semiconductors junctions, *i.e.* Schottky photodiodes, have an incredible range of uses including solar energy conversion[7, 9, 109], water splitting[110], biosensing[111, 112] and nano–optoelectronics[113], but are limited by the predetermined response of the pure metals. For each of these applications, the metal contact needs to absorb light and subsequently generate photocurrent. Efficient photocurrent generation and collection requires (*i*) high absorption within the metal film, (*ii*) preferential carrier excitation to energy levels above the Schottky barrier (SB) height, (*iii*) lossless transport of the excited carriers to the metal interface, (*iv*) emission of the carriers over the potential barrier at the interface, and (*v*) collection of the excited carriers at an ohmic contact[7, 31, 49, 109, 114]. Unfortunately, pure elemental metals generally have limitations in one or more of the above mentioned criteria, and there is thus a need for improvement through new materials development.

Au and Ag both have long electron transport attenuation lengths on the order of ~ 30 nm and are commonly used to obtain high absorption by exciting plasmonic resonances. However, both metals have a peak electron density of states well below the Fermi energy, which reduces the probability that hot electrons will be excited to energies above a SB height[115]. Further, Ag is unstable in air, and Au is not compatible with commercial semiconductor devices due to its diffusion into surrounding media at room temperature[9, 49, 115, 116]. In addition, high absorption with Au or Ag requires nanotexturing, because their optical properties are not suitable for planar, thin film cavity resonances (see Chapter 2). An alternative metal is needed that can yield more absorption, while maintaining the electrical response.

Fortunately, alloying enables tunability of the material properties ranging from structural and thermal to optical and electrical[49, 66, 115–120]. The parameter space of possible metal alloys is extensive and the resulting material properties cannot be easily predicted. In particular, AgAu alloys have already been thoroughly researched for optimizing both catalytic reactions and plasmonic performance[48, 49, 115, 116, 118, 121–125]. Au and Ag have similar lattice constants, Fermi energy and electron effective mass; however their optical properties and interband transition energies are different, making them prime candidates for alloying to achieve new optical responses without harming their thermal or electrical behavior[115, 123, 124]. Mixing Au and Ag causes a linear transition of the peak plasmon resonance and interband transition energy, but the optical properties cannot be explained by a linear combination of dielectric constants[48, 115, 121, 122, 125, 126]. While the optical properties of Au and Ag have been recently explored, there remains a lack

of understanding of how well these alloys will behave for hot carrier photodetection, particularly for near–infrared (NIR) applications.

In this chapter, we explore the NIR optical properties and, to the best of our knowledge, are the first to characterize the photo-electrical properties of co–sputtered Au and Ag alloys. We find that the alloys have an enhanced thin film absorption with respect to the pure metals, while maintaining similar hot carrier distributions for electrons and holes throughout the NIR spectrum. The d–band transitions significantly impact the hot carrier distributions at visible wavelengths, suggesting that hot carrier photodetectors should be designed to extract hot holes instead of hot electrons for visible photodetection. Finally, we find that the electron attenuation length (EAL) of pure Au outperforms pure Ag as well as all of the alloys investigated here, suggesting that despite low thin film absorption, pure Au remains the highest efficiency metal for hot carrier based photodetection in the NIR.

5.1 Impact of alloying on thin film absorption

Illuminating a metal film through a high index material ($n > 2$) reduces reflectivity and increases absorption in nanoscale films (see Chapter 2). Achieving $>$ 50% absorption requires that the thin metal film have approximately equal real and imaginary parts of the refractive indices (*i.e.* $n_m \sim \kappa_m$, where $\tilde{n} = n_m + i\kappa_m$) in order to satisfy the conditions for a thin film resonance. For example, it is possible to absorb $> 70\%$ in a 10–20 nm metal film with $n_m \sim \kappa_m$ when illuminating the metal through a Si substrate (Figure 5.1(a)). Rioux *et. al.*, developed an analytical expres-

sion to predict the optical properties of AgAu alloys from the atomic percentage of Au based on their band structure[125]. From the predicted optical properties, it appears that while pure Au and Ag do not satisfy the thin film resonance requirements for high absorption, AgAu alloys are likely to have higher absorption than the pure metals at NIR wavelengths because of their increased Drude dampening[48, 125].

To test this hypothesis, we sputtered thin films of Au, Ag and Ag_xAu_{100-x} with $x = 32$, 59, and 77 on Si and glass substrates for characterization (Figure 5.1). Energy–dispersive X–ray spectroscopy (EDS) was used to determine the alloy composition for samples on the glass substrate with an error of $\pm 2\%$ (see Table 5.1). The optical properties were determined from fits to spectroscopic ellipsometry data measured for samples deposited on the glass substrate. Figure 5.1(b) shows the measured optical response of each metal film from the ultraviolent (UV) to NIR. The refractive index minimum in the near–UV shifts from Ag to Au with increasing Au concentration. This result is in agreement with the shift in transmission maximum observed by Gong[48] and is due to the progressive increase in interband transition energy with increasing Au concentration[115, 125, 126]. At NIR wavelengths the optical properties no longer demonstrate this behavior, as the real part of the refractive index, n_m, for all alloys becomes larger than the pure metals beyond ~1000 nm. The optical loss, κ_m, is also non–linear, with Ag having the maximum and $Ag_{32}Au_{68}$ having the minimum values after ~1000 nm. We compared the measured refractive indices with the predicted values from Rioux's model (see Figure 5.2) and found that the measured values of n_m are larger for all the metal films in the NIR. This behavior is most likely due to an increase in Drude dampening from increased

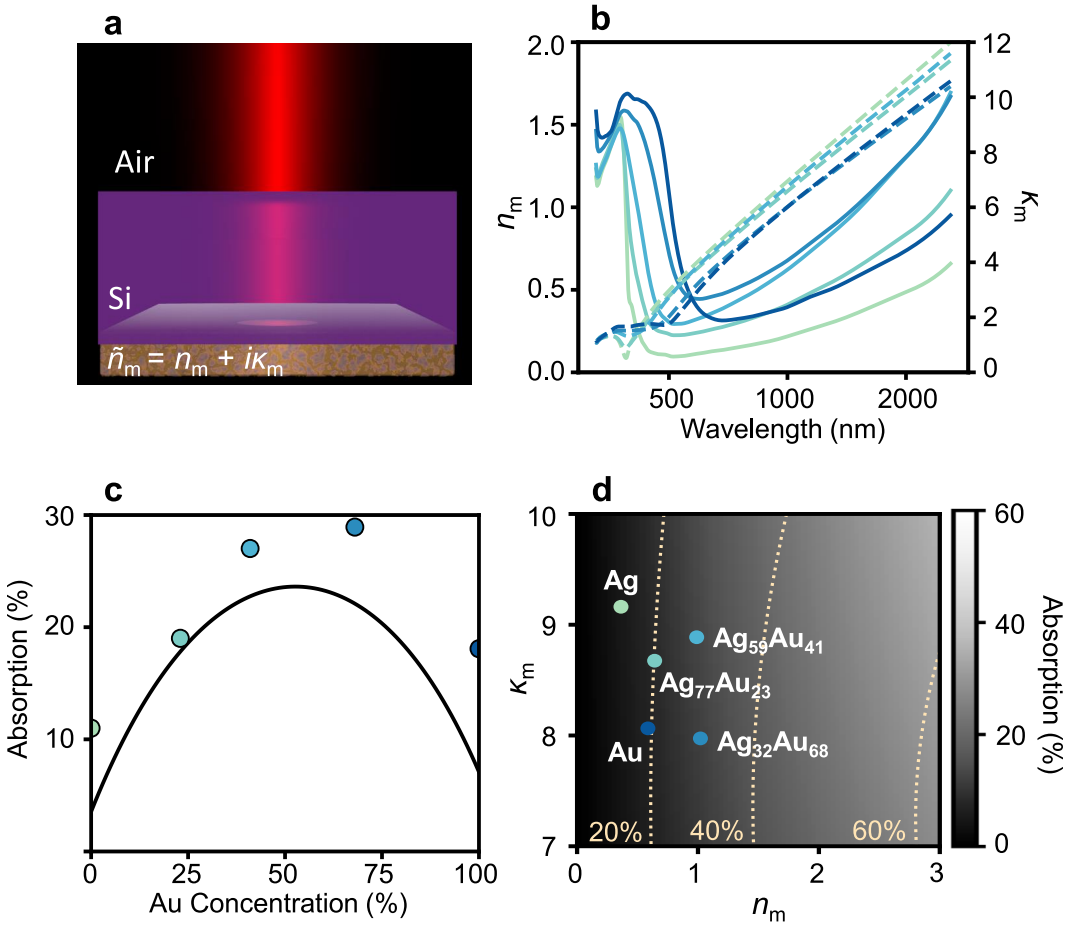

Figure 5.1: Optical response of Ag_xAu_{100-x} alloys compared to the pure metals. (a) Schematic showing illumination of a thin metal film with complex refractive index, $\tilde{n} = n_m + i\kappa_m$, through a Si substrate. (b) The measured refractive indices of each metal film. (c) Calculated absorption for varied gold concentration using optical properties determined from the analytical expression of Ref [125] (black line), and the measured optical properties of the fabricated thin film alloys (circles). (d) Calculated absorption varying the optical properties of a 10 nm thin metal film. The colored dots represent the optical properties of each metal film and the dotted lines show the absorption values of 20%, 40%, and 60%.

Goal composition	Location number	Ag (at.wt.%)	Au (at.wt.%)
$Ag_{75}Au_{25}$	1	77	23
	2	78	22
	3	77	23
$Ag_{50}Au_{50}$	1	59	41
	2	59	41
	3	59	41
$Ag_{25}Au_{75}$	1	31	69
	2	33	67
	3	31	69

Table 5.1: EDS results for the 10 nm thick AuAg alloys. EDS measurements were taken in three different locations across each sample. The composition we report is the average of the three measurements.

grain boundary and surface scattering with decreasing film thickness[127].

We calculated the expected absorption for 10 nm metal films at a wavelength of 1300 nm using the transfer matrix method[99] for illumination through a silicon substrate. Figure 5.1(c) shows the calculated absorption varying Au concentration using the optical properties predicted by Ref[125](black line) and our measured optical properties (circles). Based on this model, the alloy with the maximum absorption is $Ag_{53}Au_{47}$. The measured absorption in the alloys follows a similar trend; however, the absolute difference between the measured and predicted absorption is $\sim$10% for pure Au and $Ag_{77}Au_{23}$. By plotting the absorption versus the optical properties of the metal film (Figure 5.1(d)) we can see that the absorption increases with increasing refractive index, n_m. From Figures 5.1(c) and (d), we find that all the metals absorb $< 30\%$ with Ag having the lowest absorption despite having the

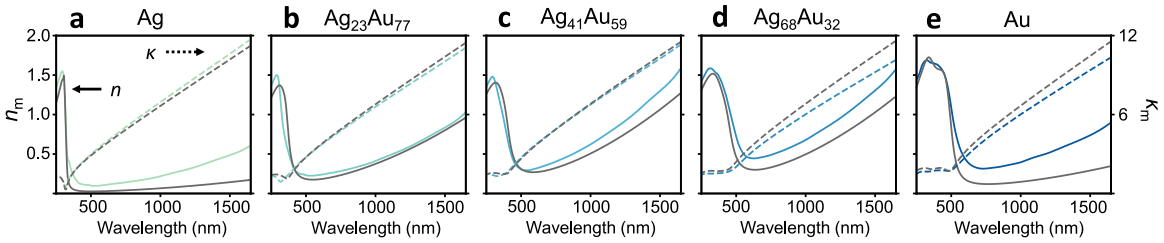

Figure 5.2: Modeled and measured refractive index. Comparison of the measured real (solid) and imaginary (dashed) parts of the refractive indices (green–blue) with the calculated values from Rioux's model[125] (grey).

highest optical loss. $Ag_{59}Au_{41}$ and $Ag_{32}Au_{68}$ absorb ∼20% more than Ag and ∼10% more than Au, with $Ag_{32}Au_{68}$ having the highest absorption. While all the alloys have larger absorption than the pure metals, $Ag_{77}Au_{23}$ has approximately equal absorption to Au with only a 1–2% absolute difference.

5.2 Impact of alloying on hot carrier distribution

Light absorption in the metal excites hot carriers, and the energy distribution of those carriers can be determined from the electron density of states (EDOS) and the wavelength of the incident light. Efficient hot electron collection requires the hot carriers to be excited to an energy level greater than the interfacial potential barrier (*i.e.* Schottky barrier). This means that the metal should have a high electron density close to the Fermi energy[49]. We calculated the reciprocal lattice dependent (*i.e.* k–dependent) EDOS for Au, Ag and alloys assuming an fcc lattice using density functional theory (DFT). The alloys were modeled with a 108–atom super cell with the arrangement of the atoms following the quasi–random structure (SQS, see 5.3)[128]. Au and Ag have nearly identical lattice constants and therefore all AgAu alloys have the same crystal structure[123, 125, 129].

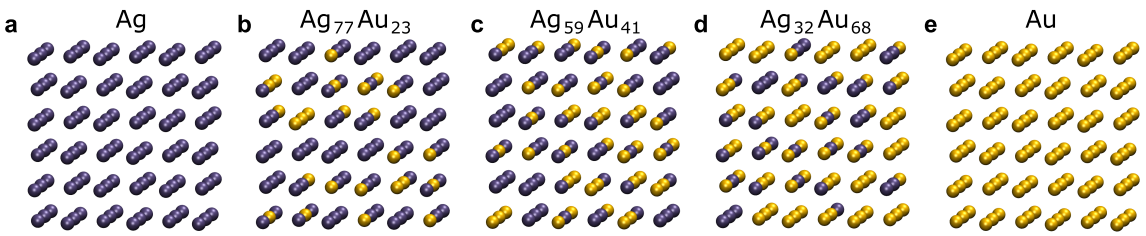

Figure 5.3: Quasi–random super cell arrangement used for DFT calculations. The blue spheres represent Ag atoms and the yellow spheres represent Au atoms.

Figure 5.4(a)–(e) shows the unfolded, k–dependent EDOS along the Γ, X, W, K and L symmetry points of the Brillouin zone. The thicknesses of the lines are correlated with the electron density while the color determines the electron contribution from each element. In agreement with previously reported band structures for AgAu alloys[125, 129], the interband transition energies are determined by the band structure at the X and L symmetry points. States above (below) Fermi energy are vacant (occupied). We find that the energy of the maximum occupied states at the X symmetry points is matched with the onset energy of the high density regions in the total EDOS values in Figure 5.4(f)–(j). We define this onset energy as the energy below the Fermi energy (E_F) where the total EDOS is 5% of its maximum value. The onset energies are 2.86, 2.41, 2.18, 2.01, and 1.78 eV in order of increasing Au molar fraction, which are consistent with the onset binding energy of the $d_{5/2}$ bands measured from the valence band and transmission spectra of AgAu alloys by Gong[129].

The joint density of states, $jDOS$, of electrons in a metal after absorption of

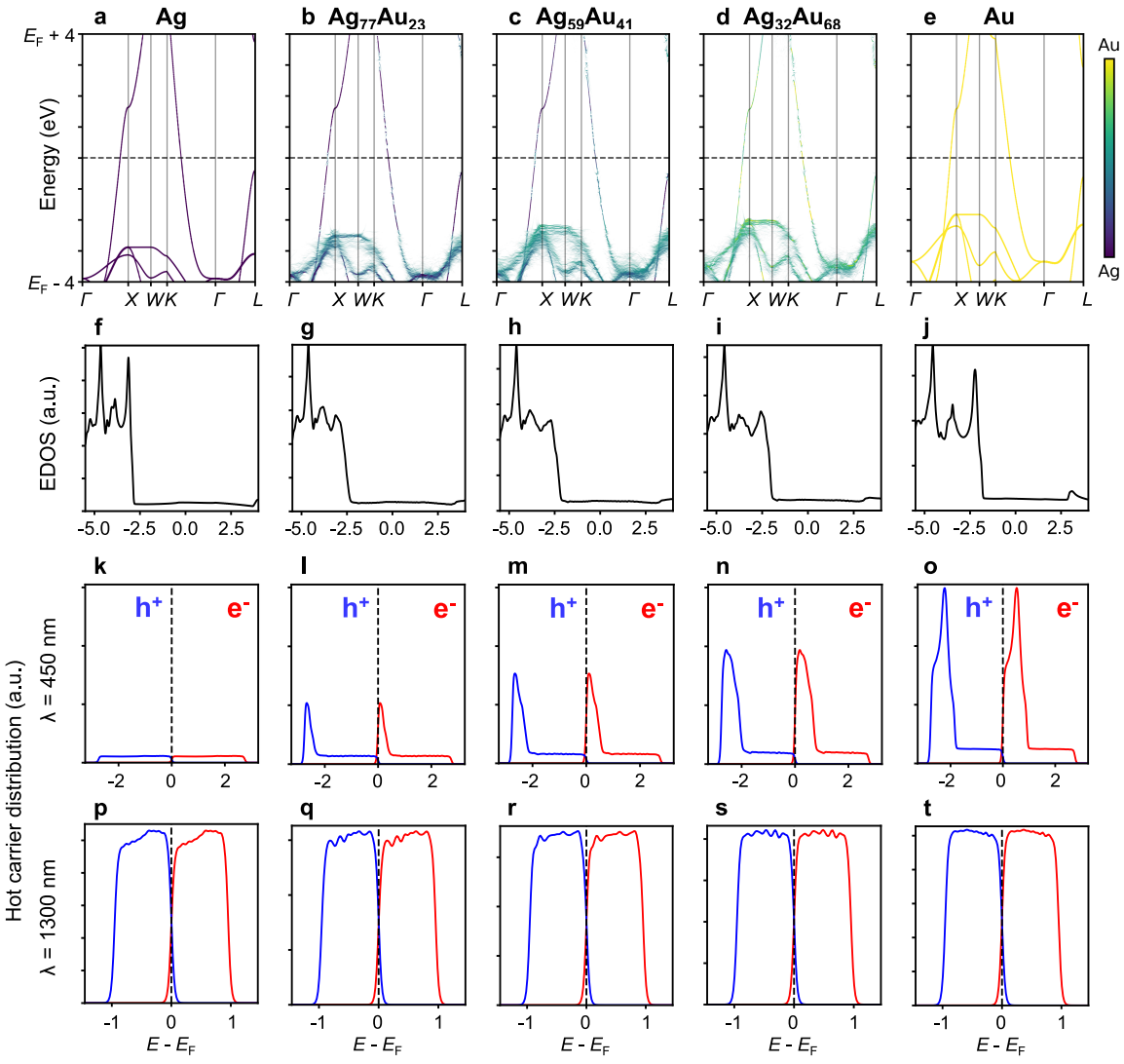

Figure 5.4: Density of states and hot carrier distribution in Ag_xAu_{100-x} alloys. (a)–(e) k–dependent density of states along the X, Γ, and L Brillouin zones for an fcc lattice. The line thicknesses are determined by the density of electrons and the color shows the electron contribution from each element. (f)–(j) Calculated total EDOS for Au, Ag and alloys. Hot carrier distribution for electrons (red) and holes (blue) under (k)–(o) 400 nm and (p)–(t) 1300 nm illumination.

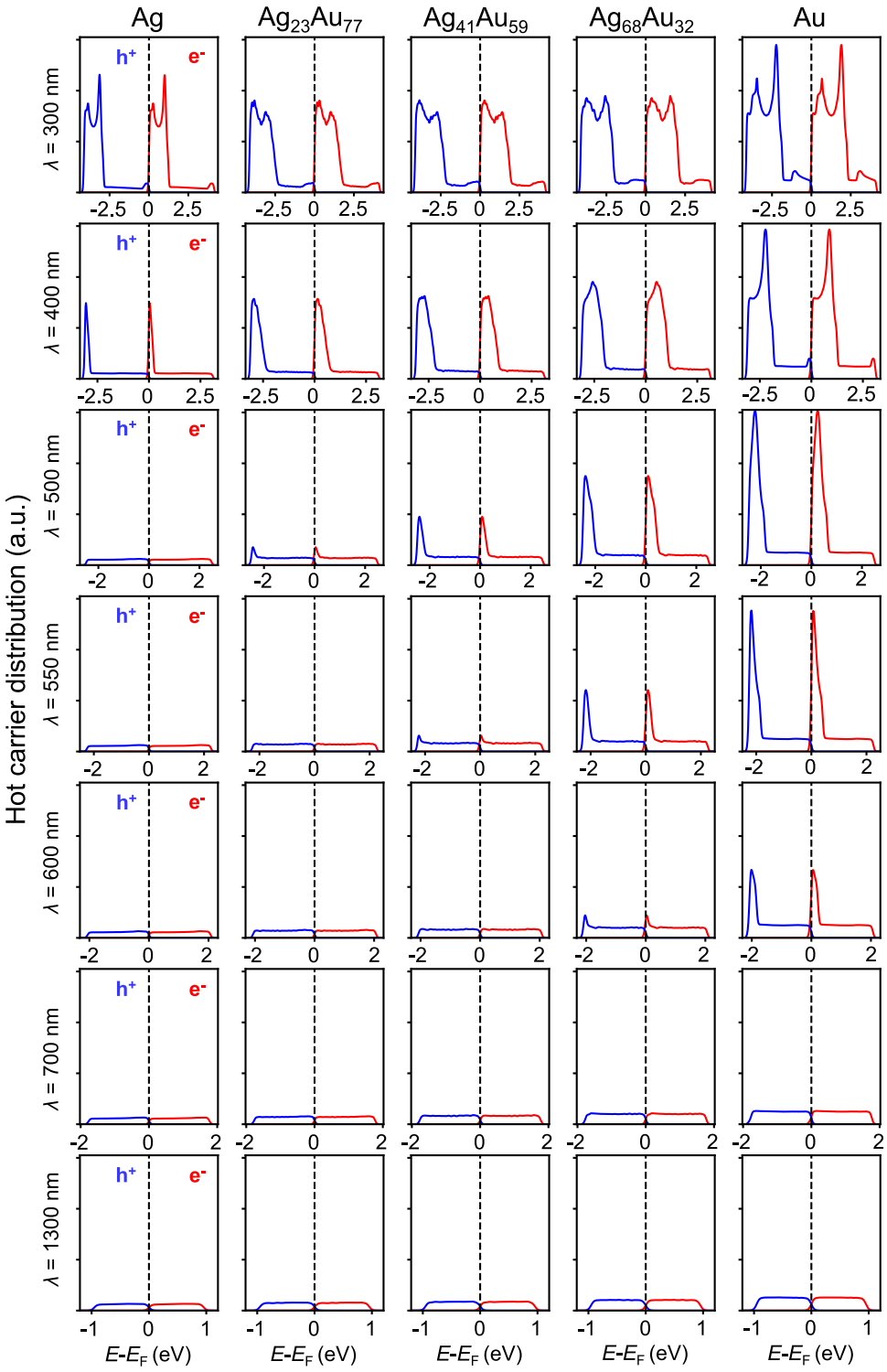

Figure 5.5: Hot carrier distribution for various wavelengths for the alloys and pure metals. The electron distribution peaks from 300 nm - 600 nm are due to d–band transitions. Notice that the d–band transition energies decrease with Au concentration. Below the d–band transition energy there is no significant difference in hot carrier distribution with wavelength as seen by comparing 700 nm and 1300 nm.

a photon with energy E_{ph} is determined by:

$$jDOS(E) \propto D(E - E_{ph})f(E - E_{ph})D(E)[1 - f(E)] \tag{5.1}$$

where $f(E)$ is the Fermi distribution function and $D(E)$ is the total EDOS. Similarly, the hot hole distribution is determined by:

$$jDOS(E) \propto D(E)f(E)D(E + E_{ph})[1 - f(E + E_{ph})] \tag{5.2}$$

The hot carrier distributions, calculated for wavelengths from 300 to 1300 nm (Figure 5.5), for the AgAu metals show peaks in the distribution corresponding to carrier excitation from the *d*–band. Note that the total density of states, $D(E)$, is normalized for these calculations such that the EDOS maximum is equal to 1.

Valenti, *et. al.*, measured the photoresponse of AgAu alloy nanoparticles on a TiO_2 substrate under visible illumination and found that Ag has the highest photoresponse despite having similar maximum absorption to pure Au and an AgAu alloy. They hypothesized that the discrepancy was likely because Ag has a larger interband transition energy and therefore the carriers excited by wavelengths between 400–600 nm are more likely to be excited to energies above the barrier height[115].

To determine how *d*–band excitations impact the probability of hot carrier collection, we calculated the $jDOS$ starting at 450 nm, which corresponds to the absorption maximum for the AgAu alloy nanoparticles in Ref[115], Figure 5.4(k)–(l). The fraction of electrons excited to an energy above the barrier height can be

written as[109]:

$$P(E) = \frac{\int_{\Phi_B}^{E_{ph}} jDOS(E)dE}{\int_{0}^{E_{ph}} jDOS(E)dE} \tag{5.3}$$

where Φ_B is the SB height. Because of the work function difference between Au and Ag, Φ_B for each metal cannot be expected to be the same on similar substrates[102, 130]. However, for the sake of simplicity, we calculate the percentage of electrons that are excited above a barrier height of 0.6 eV for all metals. For 450nm (*i.e.* visible) illumination, the percentage of electrons that will be excited above the barrier height are 78%, 46%, 35%, 33% and 41% for Ag, $Ag_{77}Au_{23}$, $Ag_{59}Au_{41}$, $Ag_{32}Au_{68}$ and Au respectively. This confirms that the *d*–band transitions are parasitic to the photoresponsivity when collecting hot electrons (*i.e.* using an *n*–type substrate). Alternatively, Figure 5.4(k)–(l) shows that *d*–band excitations are beneficial for hot hole collection. The percentage of hot holes excited to an energy above the barrier height are 77%, 87%, 90%, 93% and 93% for Ag, $Ag_{77}Au_{23}$, $Ag_{59}Au_{41}$, $Ag_{32}Au_{68}$ and Au respectively. This suggests that SB photodiodes designed to absorb photons from UV to visible should use *p*–type substrates (as opposed to *n*–type substrates) in order to collect hot holes instead of electrons.

For NIR illumination, the hot carrier distribution is roughly even across $E_F < E < E_{ph}$ for all metals with Ag and Au having a slightly favorable distribution for hot electrons and holes, respectively (Figure 5.4(p)–(t)). For a barrier height of 0.6 eV, under 1300 nm illumination, the probability that hot electrons will be excited to an energy above the barrier is 35–37% for all metals. Similarly, the probability for hot holes ranges from 33–36% for all metals. Because these values are similar, there

is little difference between selecting a p–type or n–type substrate for absorption of light with energy less than the d–band transition.

5.3 Measured device performance

For experimental determination of absorption and photoresponse for NIR illumination, the Au, Ag and alloy films were deposited on an n–type silicon substrate. Prior to depositing the metal films, Al ohmic contacts and a Si_3N_4 anti–reflection coating were deposited on the opposing side of each substrate. The Si_3N_4 thicknesses were 165±5 nm for all samples, except for the pure Au sample, which was 145±5 nm resulting in a shift in the reflection minimum from ∼1350 nm to ∼1200 nm. The metal film thicknesses were calculated from fits to the measured ellipsometry reflection and transmission data and all film thicknesses were 10±2 nm. Because Au does not properly adhere to silicon, a ∼1 nm Ti adhesion layer was deposited prior to the pure Au deposition. The pure Ag and alloys did not require an adhesion layer. This was verified by inspection using a scattering electron microscope (SEM). SEM images for pure Ag and $Ag_{59}Au_{41}$ are shown in Figure 5.6.

While the measured absorption in Figure 5.7 is consistent with the calculations showing that the Au rich ($Au_{68}Ag_{32}$) alloy will have the highest absorption, pure Au has the highest measured responsivity. With the exception of pure Au, the responsivity of the photodiodes follows the trend of their measured absorption with Ag having the lowest and $Au_{68}Ag_{32}$ the highest. This leaves the question of why the Au film has the highest photoresponse when it does not present the highest

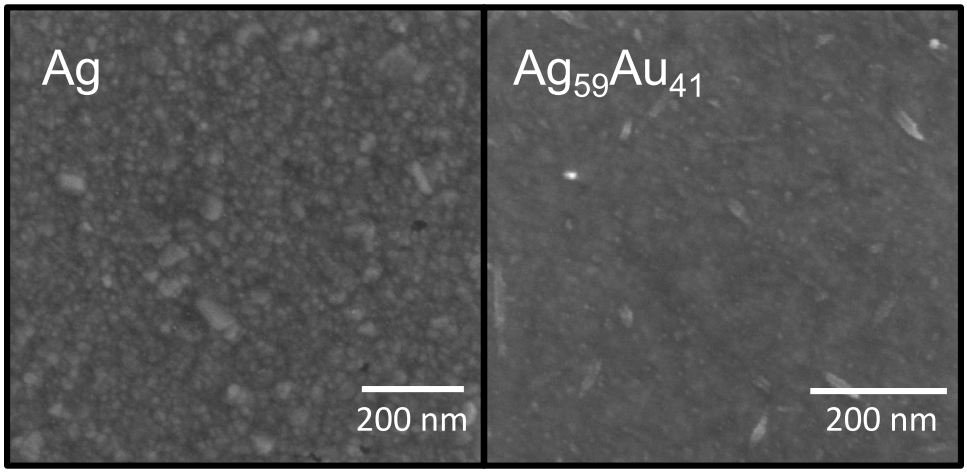

Figure 5.6: SEM images of Ag and $Ag_{59}Au_{41}$ deposited on silicon.

absorption.

Factors that impact the photoresponse, other than absorption, are the SB height, EDOS and hot carrier attenuation length. According to the modified Fowler theory, the internal quantum efficiency (*i.e.* the ratio of extracted carriers to absorbed photons) can be approximated by $IQE \propto (E_{ph} - \phi_B)^2/E_{ph}$, and therefore a decrease in barrier height would lead to an increase in photoresponse[6, 102, 109]. A linear fit to $\sqrt{IQE \times E_{ph}}$ can be used to determine the SB height of each photodiode, and we find that the Au sample has the largest barrier height ($\phi_B = 0.66 \pm 0.02$ eV, see Figure 5.8). As a result, the only likely explanation for the higher measured photoresponse is a greater hot carrier attenuation length in the Au (with respect to Ag and the alloys), because the EDOS distribution in this wavelength region is approximately the same for Au, Ag and all alloys.

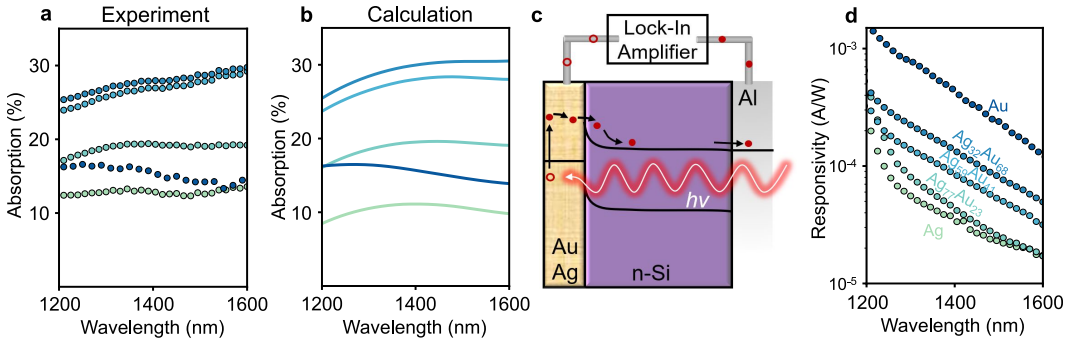

Figure 5.7: Absorption and photoresponse. (a) Measured and (b) calculated absorption of Au, Ag and Ag_xAu_{100-x} metal films when illuminated through a Si substrate. (c) Band diagram of the Ag_xAu_{100-x} Schottky photodiodes. Sub–bandgap photons (*i.e.* $h\nu < E_g$) are absorbed in the back metal contact and excite hot electrons. The electrons travel to the interface, are injected into the n–Si substrate and are collected at the Al ohmic contact. (d) Measured photoresponse of all photodiodes. The photoresponse is measured using a lock–in amplifier.

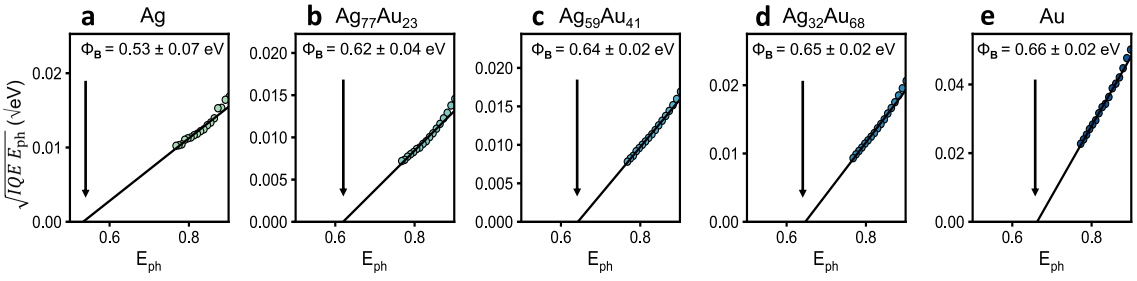

Figure 5.8: Fit to Fowler yield to determine Schottky barrier height for all metals. The barrier height increases with Au concentration.

5.4 Determining the hot carrier attenuation length

Under many circumstances, the EAL can be determined by measuring the *IQE* of a metal film while varying the film thickness, as discussed below. For clarity, we define the EAL as the hot electron decay length as a result of all scattering events including electron–electron and electron–phonon scattering. The EAL should not be confused with the inelastic mean free path, which only considers the average distance between electron–electron collisions. Under front illumination (*i.e.* illuminating the metal directly from air), the *IQE* as a function of film thickness, t, is given by:

$$IQE(t) = C\left(\frac{\alpha L}{\alpha L - 1}\right)\left(\frac{e^{-t/L} - e^{-\alpha L}}{1 - e^{-\alpha L}}\right) \tag{5.4}$$

where α is the optical absorption constant determined by $4\pi\kappa_m/\lambda$, L is the electron attenuation length, and C is a device dependent constant of proportionality that depends on the quality of the Schottky junction. If the film thickness and EAL are greater than the optical penetration depth (*i.e.* $\alpha L > 1$ and $\alpha t > 1$, where $1/\alpha$ is the optical penetration depth), Equation 5.4 reduces to:

$$IQE(t) = C\left(\frac{\alpha L}{\alpha L - 1}\right)e^{-t/L} \quad \text{or} \quad ln(IQE(t)) = ln\left(C\left(\frac{\alpha L}{\alpha L - 1}\right)\right) - \frac{t}{L} \tag{5.5}$$

therefore the slope of $ln(IQE)$ versus thickness yields the EAL. Equations 5.4 and 5.5 have been derived assuming the incident illumination is exponentially attenuated within the metal (*i.e.* the amplitude of the incident EM wave decays as $e^{-\alpha z}$ where

z is the incident axis), the probability of collecting a hot electron that is excited at a distance $(t - z)$ from the Schottky interface is proportional to $e^{-(t-z)/L}$, and that the quality of the SB (*i.e.* the proportionality constant, C) is the same for all films. In addition, it is assumed that the metal film is thick enough that optical reflection from the metal/semiconductor interface and multiple reflections of the hot electrons can be neglected[131, 132].

The EAL of pure Au and Ag have previously been measured using this method, but the results have varied depending upon analysis and deposition conditions. Measurements performed by Crowell *et. al.*[132] obtained $L \sim 74$ nm and 44 nm for Au and Ag respectively. Soshea *et. al.* later pointed out that Crowell determined IQE using absorption measured from glass substrates as opposed to the silicon substrates that were used to measure the photoresponse[133]. Because the substrate can significantly impact the absorption, these values were found to be incorrect. Soshea *et. al.* found that the corrected EAL for Au was $L \sim 33$ nm, but they did not measure the corrected EAL for Ag. Leder *et. al.*[134] claimed to have measured $L \sim 45$ nm for Ag, which is consistent with Crowell's measurements, however, to the best of our knowledge, Leder never officially published their measurements. Gould *et. al.*[135] later measured $L = 20$–30 nm and 30–40 nm for Ag and Au respectively and Bernardi *et. al.*[136] calculated that the EAL for low energy photons is also influenced by the crystallographic direction, with the [110] direction leading to the longest EAL and [111] the lowest.

We measured the EAL of Ag_xAu_{100-x} for $x = 100$, 65, 54, 39, and 0 by depositing multiple thicknesses of each metal on large Si substrates (see Figure

Film thickness (nm)	Atomic Weight (Ag–Au %)	Standard devation(%)
28	64.89 – 35.11	0.53
37	62.84 – 37.16	0.47
46	63.51 – 36.49	0.38
55	63.92 – 36.08	0.58
63	63.47 – 36.53	0.32
79	67.42 – 32.58	4.58
Total Average:	64.55 – 65.45	2.66

Table 5.2: EDS results for all thicknesses of the $Ag_{65}Au_{35}$ alloy. EDS measurements were taken in multiple locations across each sample. Here we show the average and standard deviation of all measurements. The total average is the average of all measurements from every film thickness.

5.9(a–e)). An Al ohmic contact was deposited on the reverse side of each substrate. Because all of the metal films are on the same substrate, we can assume that the carrier collection properties (*i.e.* device resistance, resistance of the ohmic contact, etc) will be consistent. Prior to deposition the substrates were chemically cleaned, and all metals were co–sputtered through a shadow mask without breaking vacuum. Each film was also simultaneously deposited on a glass substrate. Immediately after deposition, the film thicknesses and optical properties were determined from fits to measured reflection and transmission ellipsometry data and the chemical composition was measured using EDS (see Tables 5.2–5.4 and Figure 5.10). Both the ellipsometry and EDS measurements were done on the glass substrate.

The absorption, A, in each metal film was calculated from measured reflection, R, and transmission, T, on the Si substrate using $A = 1 - R - T$, Figure 5.9(f–j). We

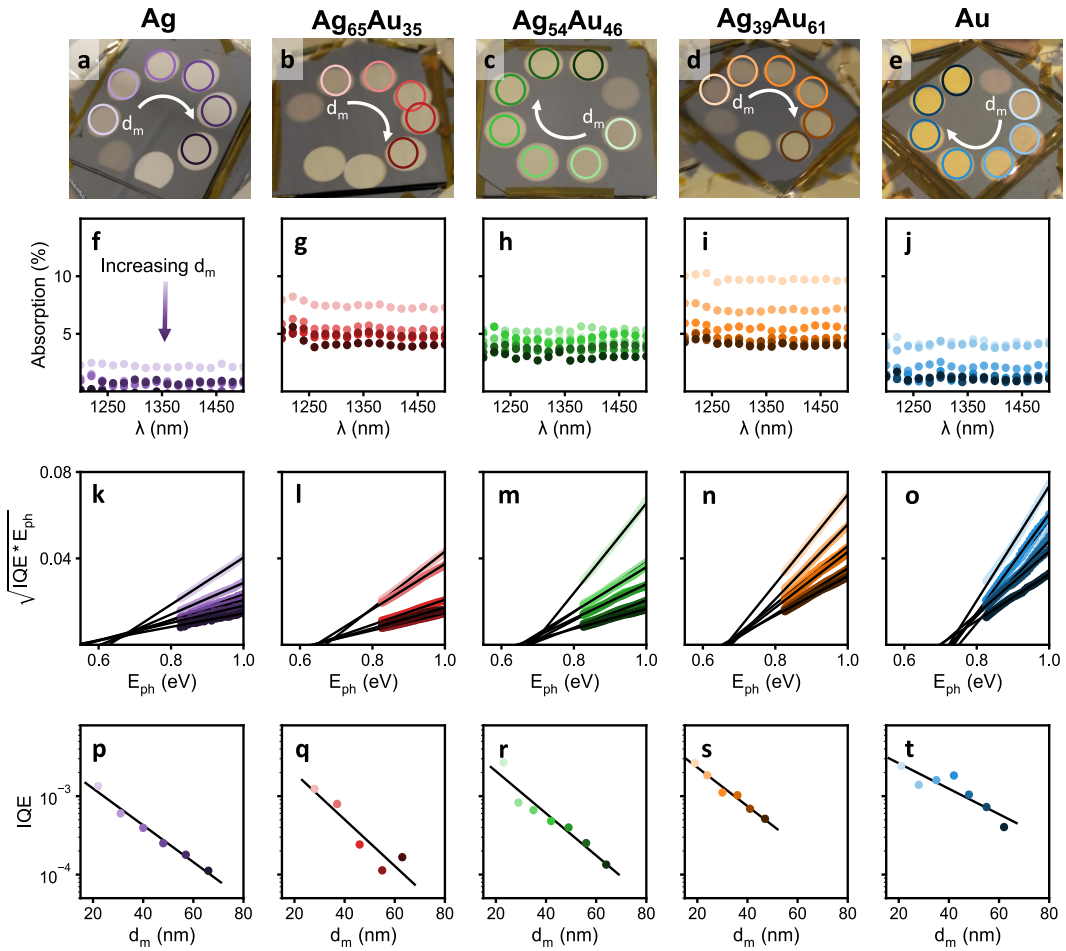

Figure 5.9: Measuring the hot electron attenuation length. (a)–(e) Optical images of the samples taken immediately after deposition. The film thicknesses are color coded from light to dark in order of increasing film thickness, d_m. (f)–(j) Raw data of measured absorption for all film thicknesses. (k)–(o) Calculated Fowler yield (circles) for all film thicknesses and their line fits (black lines) used to determine barrier height. (p)–(t) Logarithmic plot IQE versus film thickness for $E_{ph} = 0.9$ eV. The data was fit to a line (solid, black line) in order to extract the hot electron attenuation length.

Film thickness (nm)	Atomic Weight (Ag–Au %)	Standard devation(%)
16	56.96 – 44.71	1.54
23	55.77 – 44.23	1.06
29	55.48 – 44.52	0.71
35	53.67 – 44.63	0.65
49	53.46 – 44.54	0.87
56	52.53 – 47.47	0.71
64	51.45 – 48.55	1.81
Total Average:	54.39 – 45.61	2.1

Table 5.3: EDS results for all thicknesses of the $Ag_{54}Au_{46}$ alloy. EDS measurements were taken in multiple locations across each sample. Here we show the average and standard deviation of all measurements. The total average is the average of all measurements from every film thickness.

Film thickness (nm)	Atomic Weight (Ag–Au %)	Standard devation(%)
19	38.50 – 61.50	1.25
24	39.95 – 60.05	3.0
30	39.93 – 60.07	1.03
36	36.23 – 63.76	0.74
41	37.77 – 61.23	0.67
47	36.77 – 62.23	0.65
Total Average:	38.62 – 61.38	2.56

Table 5.4: EDS results for all thicknesses of the $Ag_{39}Au_{61}$ alloy. EDS measurements were taken in multiple locations across each sample. Here we show the average and standard deviation of all measurements. The total average is the average of all measurements from every film thickness.

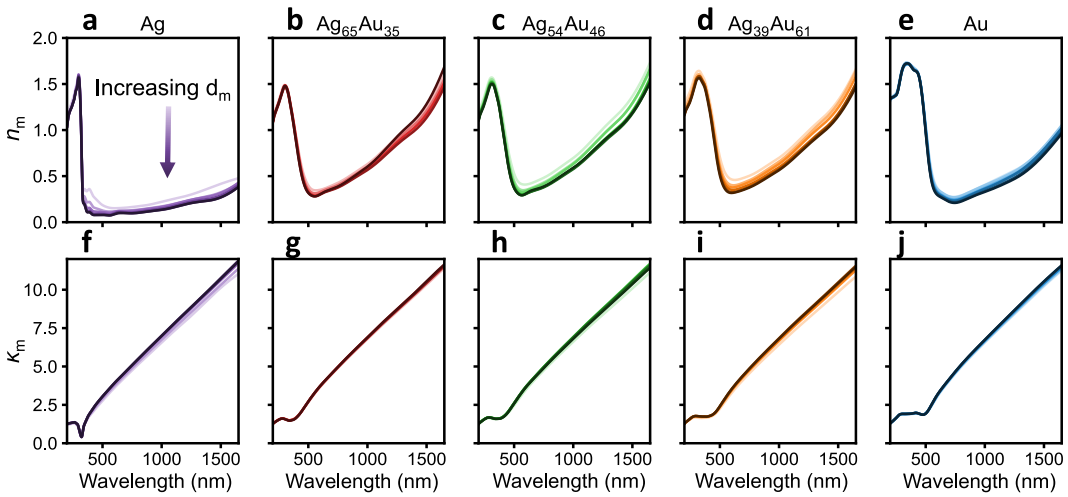

Figure 5.10: Optical properties of all metal films used to determine electron attenuation length. Increasing film thickness, d_m, is represented by increasing color darkness. The film thicknesses range from 20-80 nm.

find that, even for illumination through air, the alloys absorb ∼5–10% more than the pure metals. Note that we exclude the thinnest film thickness on all samples from the measurements because these film thicknesses are below the optical penetration depth (*i.e.* $1/\alpha$) and therefore does not satisfy the $\alpha t > 1$ requirement for Equation 5.5. We also excluded the maximum film thicknesses for Ag, $Ag_{65}Au_{35}$ and $Ag_{39}Au_{61}$ because the films were too thick causing the photoresponse to be too low to measure.

The IQE was calculated from the measured responsivity and absorption, which can be determined by:

$$IQE(E_{ph}) = \frac{E_{ph}}{q} \times \frac{R}{A} \tag{5.6}$$

where E_{ph} is the photon energy, q is the charge of an electron, R is the measured responsivity in units of Ampere/Watt and A is the measured absorption. The measured absorption for the thicker Ag films is below the signal to noise ratio of

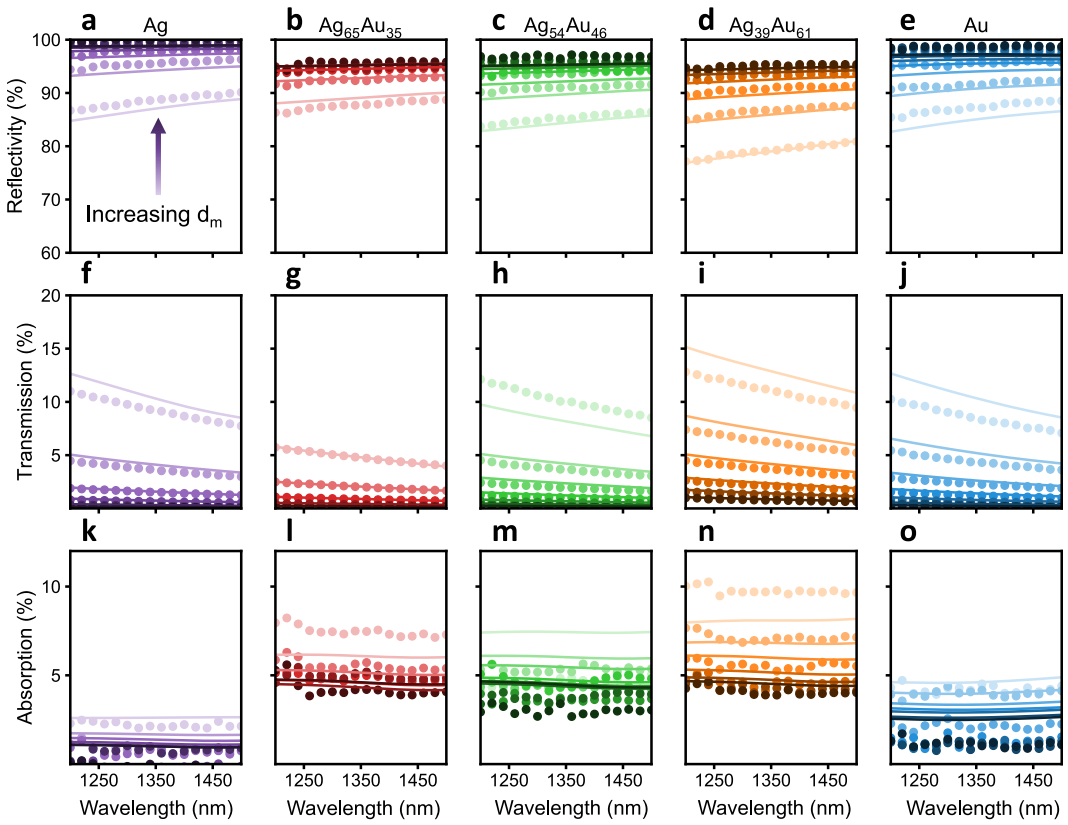

Figure 5.11: Comparing measured (filled circles) and calculated (solid lines) (a–e) reflectivity, (f–j) transmission, and (k–o) absorption for all metal films.

our measurements, however the measured absorption closely matches the expected absorption calculated using the optical properties determined from ellipsometry (see Figure 5.11). We therefore use the calculated absorption for determining the IQE for each Ag film thickness. For all other alloys the IQE was determined from the measured absorption using a Savitzky–Golay filter to reduce the noise in the measurements (see Figure 5.12). The source of the noise in the measurements was predominantly due to laser power fluctuations.

The barrier height for each photodiode was determined using a linear fit to the Fowler yield, $\sqrt{(IQE \times E_{ph})}$, for each photodiode. The variation in the barrier heights can be seen as the x–intercept of the linear fits in Figure 5.9(k–o). The

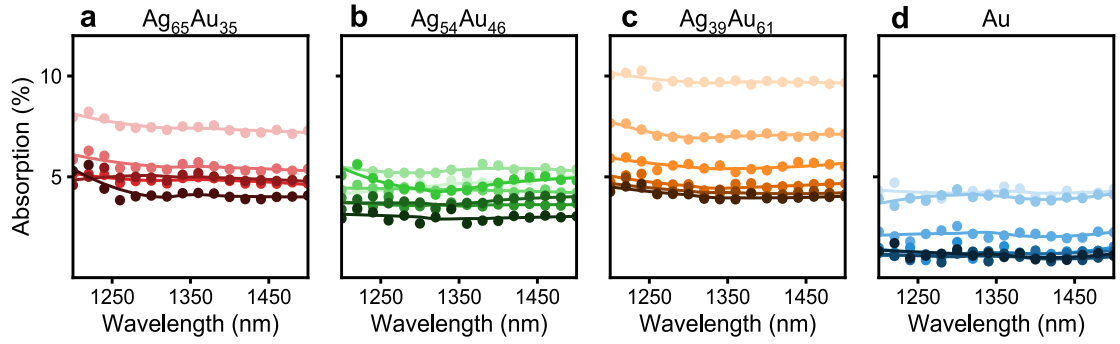

Figure 5.12: Comparing the measured absorption (filled circles) and the smoothed absorption data as a result of applying a Savitzky–Golay filter (solid lines) to reduce noise.

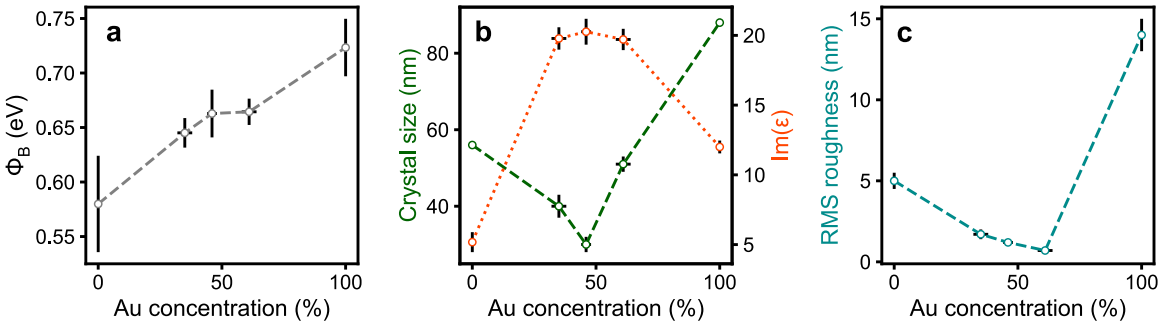

Figure 5.13: Material and thin film properties. (a) Measured barrier heights from a fit to the modified Fowler equation. (b) Crystal size (green, dashed) was measured using X–ray diffraction. The crystal size increases Drude dampening, which increases the imaginary part of the dielectric function of each metal (orange markers and dotted line). (c) The RMS roughness of each metal was measured using an AFM.

barrier heights for each metal are consistent with relative differences $< 5\%$, except for pure Ag which has a larger spread ($< 9\%$). The average barrier height for each metal increases almost linearly from 0.58 eV to 0.72 eV with increasing Au content, Figure 5.13(a).

Maintaining the slope from the linear fits to the Fowler yield, the IQE for each film thickness was determined using the average barrier height for each metal at a photon energy of 0.9 eV, Figure 5.9(p–t). The EAL is determined by the slope

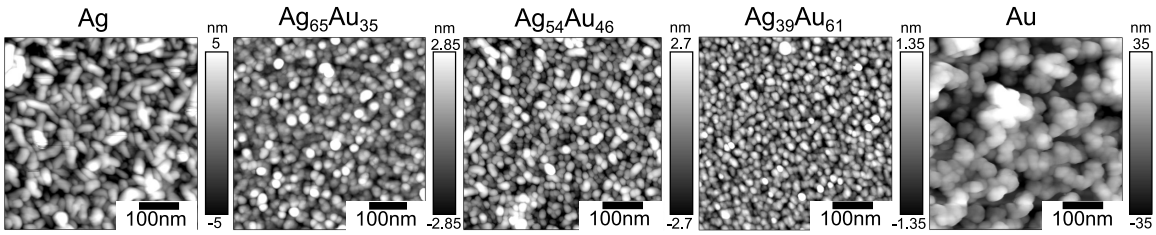

Figure 5.14: AFM z–scan topography images used to determine RMS roughness in Figure 5.13(c)

of the linear fit to $ln(IQE(t))$. The extracted EAL is shown in Figure 5.15. We find that Au has the highest attenuation length and $Ag_{65}Au_{35}$ has the lowest, however $Ag_{65}Au_{35}$ and $Ag_{54}Au_{46}$ have similar EAL's within error. The error is defined as one standard deviation error as determined by the covariance matrix in the linear fit to $ln(IQE(t))$. Au has the largest error because it has poor adhesion to Si resulting in reduced film quality, but the measured EAL is consistent with previously reported results within error. AFM topography scans verified that Au has the largest crystal sizes and surface roughness resulting in poor film quality (see Figures 5.13 and 5.14). The thin film Au device shown in Figure 5.7 has significantly greater performance as a result of improved film quality because of the Ti adhesion layer.

While alloys with $> 70\%$ Au may result in higher EAL compared to pure Ag, all the measured alloys have reduced EAL compared to the pure metals. There are many material dependent factors that impact the EAL, including the Fermi velocity of the electron gas, plasma frequency, atomic radius and crystal orientation; however, most of these factors are similar between the Au and Ag films with the exception of the plasma frequency[44, 137, 138]. (Note that X-ray diffraction (see Figure 5.16) shows that the preferred crystal orientation for all the metals was [111]

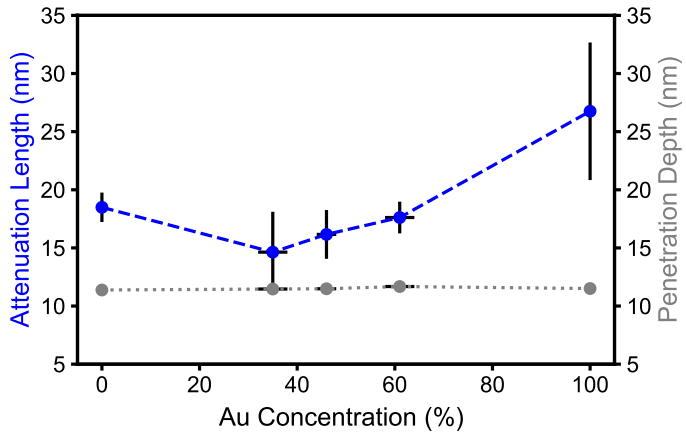

Figure 5.15: Hot electron attenuation length. Measured EAL varying Au concentration compared to the optical penetration depth.

with only Ag showing a small percentage of crystals in the [100] direction.) If only the plasma frequency was impacting the EAL of the alloys, the EAL would likely increase almost linearly with increasing Au concentration. Because this is not the trend that the data shows, the most likely factor impacting the EAL of the AgAu alloys is an increase in scattering sites for the electrons as opposed to an intrinsic electrical property of the metals.

Enhanced electron scattering can arise from grain boundaries and surface roughness. In our case we find that the most significant contributing factor is grain boundary scattering. Using X–ray diffraction we found that $Ag_{54}Au_{46}$ and $Ag_{65}Au_{35}$ have the smallest and second smallest grains, respectively (Figure 5.13(b) and Figure 5.16). Reduced grain sizes result in a shorter path length between electron scattering events resulting in a decrease in electron mean free path. Even the Drude dampening, which is also influenced by electron scattering, follows the trend of the metal grain size (Figure 5.13(b)). In addition, AFM surface scans show that the alloys have lower surface roughness and therefore are less likely to be impacted

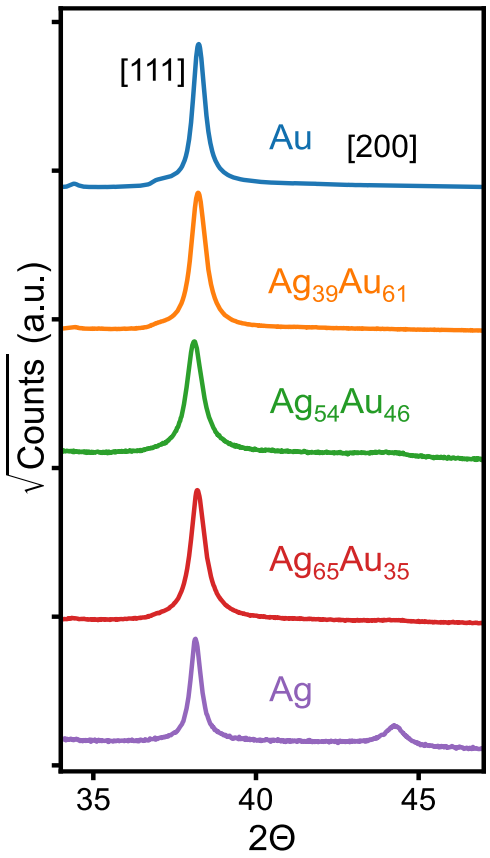

Figure 5.16: X–ray diffraction data for all alloys. Data from $2\Theta = 34 - 47°$ showing the varying peaks from pure Au to Ag. The data was taken using a D8 Advance powder diffractometer. The data was fit using the LeBail method to extract the crystal sizes.

by surface scattering than the pure metals (Figure 5.13(c)).

5.5 Fabrication methods and experimental details

This section contains additional device characterization and information on fabrication methods and experimental design used in this chapter.

5.5.1 Sample Fabrication

All the photodiodes were fabricated on 370 μm thick, double side polished, $< 100 >$ n–type silicon wafers (< 1 Ωcm). The wafers were chemically cleaned using piranha (3:1 sulfuric acid (H_2SO_4) and hydrogen peroxide (H_2SO_4)) and a buffered oxide etch (BOE) prior to depositing a thin Al ohmic contact through a shadow mask using electron beam evaporation (Angstrom). The Al contacts were annealed at 425°C in forming gas (96% Ar and 4% H_2).

All alloys were co–sputtered using pure metal targets with $> 99.99\%$ purity. Immediately prior to deposition, a thick photoresist layer was spin–coated over the entire Si surface with the Al contacts. The opposing side of the substrates were then cleaned with BOE to remove the oxide growth resulting from the Al contact anneal. The metals in Figure 5.7 were sputtered through a shadow mask on 1 cm^2 n–Si wafers using an AJA ATC 1800 sputtering unit. The metals for the EAL (Figures 5.9 and 5.15) were sputtered through a circular shadow mask with 0.3 inch diameter on a 3.2 $\times$ 3.2 cm^2 n–Si substrate using an AJA ATC Orion 8 sputtering unit. The shadow mask was rotated between depositions without breaking vacuum in order to

prevent oxidation.

5.5.2 Material characterization

For each metal deposition, a glass slide was included in the deposition to determine the thickness, refractive index and alloy composition of the deposited metal. All material refractive indices and thicknesses were determined using a J.A. Woollam M–2000D Spectroscopic Ellipsometer, 8–inch (190–1690 nm). The alloy composition was measured in a Hitachi S–3400 variable pressure SEM fitted with an EDS analyzer. The measurements were taken using a 6 kV beam with 75 A current.

Surface roughness measurements were taken in a Cypher Atomic Force Microscope (Asylum Research) under ambient atmosphere. For each metal, three $1 \times 1 \mu$m scans were taken. The reported roughnesses are all root mean square roughnesses (RMS) and are calculated by taking the RMS value of each line of the AFM image and taking the median of these values.

5.5.3 Optical and electrical measurements

Absorption measurements in Figure 5.7 were performed using a 6–inch integrating sphere (Labsphere RTC–060) with illumination at $\sim 12^{\circ}$ incidence. Two Ge photodiodes were used to measure the light intensity inside the integrating sphere and to monitor power fluctuations of the incident beam. Specific NIR wavelengths were selected from a supercontinuum source (Fianium WhiteLase^{TM}) using an acousto–optic tunable filter (AOTF) and the incident light was chopped using

a rotating disk chopper. The signals from the photodiodes were measured using a SR830 lock–in amplifier with the reference frequency matched to the frequency of the optical chopper. The uncertainty of the measured absorption is ±0.5%.

To determine the responsivity of the fabricated photodiodes, the samples were mounted on a vertical stage with copper probes forming electrical contact to the Al ohmic and AgAu contacts. The incident light was focused on the sample at normal incidence and the power incident on the sample was determined by a calibrated Ge photodiode. The signals from the sample and each photodiode were measured using a SR830 lock–in amplifier. There is a 2–3% uncertainty in the measured responsivity.

The absorption of the alloys for the EAL measurements were measured on the same stage used to measure responsivity. The absorption was determined from measuring the transmission and reflection. The transmission was measured by mounting a calibrated Ge photodiode directly behind the sample aligned to the incident beam. The reflection was measured by reflecting the incident light off the sample at a near–normal incident angle of 10±2° into a calibrated Ge photodiode. The reflected and transmitted power was compared to the total power hitting the sample as measured by a reference calibrated Ge photodiode to determine the percent reflection and transmission.

5.5.4 Density functional theory

The DFT calculations were performed on a supercell containing 108 atoms of Au and Ag in different concentrations. The disordered alloys were obtained by

constructing a special quasi–random structure converging the correlation function of the disordered alloy up to third nearest neighbors, using the ATAT package[139]. Using these coordinates the density of states and band structures were obtained calculated with the SIESTA code[140] with a double–ζ atomic basis set with polarization orbitals, norm conserving relativistic pseudo potentials and the PBE–flavor of the generalized gradient approximation (GGA) for the exchange and correlation potential. The structures were fully relaxed to a target pressure of 0 kbar, and a maximum for of 0.01 $eV/\mathring{A}^{-1}$ using a 500 Ry real space mesh cutoff, and a $30\times30\times30$ $(7 \times 7 \times 7)$ k–point grid for the pure metals (alloys). In the case of the density of states the k–point grid was increased threefold. Finally the unfolding of the bands follows a generalization of the work by Mayo *et al.*[141] for orbital–projected bands.

5.6 Discussion and conclusions

Because the EAL appears to be significantly impacted by the grain boundaries, it is likely possible to improve the EAL by finding methods of increasing the grain sizes. The EAL could also be lower in these films because of the preferred crystal orientation[136]. Increasing the grain size and reorienting the crystals to the [110] or [100] directions could be accomplished through thermal evaporation of a pre–alloyed target or exploring other deposition methods such as pulsed laser deposition. However, a decrease in electron scattering will also result in a decrease in Drude dampening and will subsequently reduce the thin film absorption. Rioux's model shows that the alloys will always have higher intrinsic defect scattering com-

pared to the pure metals suggesting that their EAL will not surpass pure Au. In fact, the difference between the expected absorption for the alloys and our measured absorption in Figure 5.1c is likely because of enhanced scattering from grain boundaries resulting from co–sputtered deposition. Therefore, it is reasonable to assume that increasing grain sizes would only reduce the thin film absorption by ∼10%. As a result, it may be possible to increase the EAL of the alloys to lengths longer than pure Ag.

In summary, we have shown that Ag_xAu_{100-x} alloys have 10–20% higher absorption compared to the pure metals in the NIR. Yet, even though their hot carrier distributions are equivalent, pure Au outperforms Ag and the alloys for efficient hot carrier photodetection. The beneficial performance of Au appears to be correlated with electron scattering from grain boundaries; because Au has the largest grain boundaries, it has the lowest volume of scattering sites and therefore the longest EAL. We observe an inverse relationship between the Drude dampening (*i.e.* the imaginary part of the dielectric function) and the EAL, which is expected because both are impacted by electron scattering. Therefore, it may be possible to predict whether alloying will reduce or increase the EAL with respect to pure metals through simply measuring the imaginary part of the dielectric function. Further investigation is required to find an alloy that has high absorption, ideal hot carrier distribution and a long EAL. Because metals such as Pt and Cr have high absorption (see Chapter 2), it may be possible to find alloys with these metals that will increase their EAL. Gong and Munday showed that it is possible to improve the hot hole distribution for efficient carrier injection in Pt through alloying with

Au[49]. Further, alloys involving three or more metals may provide additional opportunities to customize both the material's optical and electrical response and to maximize the hot carrier generation and injection, leading to higher efficiencies and new photodetector architectures.

Chapter 6: Conclusions and outlook

This thesis has described our latest work using ultrathin, planar metal films as a low–cost solution for photodetection below the bandgap of semiconductors that is also compatible with VLSI technology. In Chapter 2, we demonstrated that carefully selecting the optical properties of ultrathin metal films illuminated through a high index superstrate, such as silicon, can result in $> 70\%$ absorption. Metals such as Pt, Fe, Ti and Cr satisfy the optical properties of the FP–like cavity resonance required for high absorption. Using this principle, we realized a room temperature, Si–based NIR imaging detector with photocurrent generated from a $\sim$16 nm back contact of Pt. This device had a photoresponsivity of 0.1–0.001 mA/W for wavelengths 1.2–1.5 μm at zero–bias. Because the maximum absorption is determined by the optical properties of the surrounding media, a thin metal film sandwiched between a high index superstrate and an INZ substrate will have near–perfect absorption, which was shown in Chapter 3. In Chapter 4, we demonstrated that the responsivity of the Pt/Si SB photodiode is enhanced by $> 80\%$ with an INZ substrate because of both an increase in absorption and a doubling of the carrier transport probability. We investigated using metal alloys to modify absorption, hot carrier density of states and carrier transport in Chapter 5. To conclude this thesis, this chapter considers

future improvements for these devices along with considerations for integration with other optical devices.

6.1 Future considerations for improving device IQE

While the FP–like cavity effect greatly improves the absorption of SB photodiodes from the early maximum of 30–40% to near–perfect absorption, there is still room for improvement to increase the IQE. It will be important to further study the effects of INZ substrates on the carrier dynamics in absorbing metals in order to fully utilize the performance enhancement. Schultz, *et. al.* studied the migration of Pt into INZ substrates and their results suggest that the SB photodiode performance enhancement seen in Chapter 4 degrades with time; however, a blocking layer could prevent this migration[107]. Other INZ substrates such as In:SnO or Ga:ZnO, as opposed to AZO, might also be used to explore how the material properties of the INZ substrate impact the carrier dynamics in the absorbing metal film[75, 78, 142].

The IQE of these SB photodiodes could also be further improved by tailoring the optical and electrical properties of metals through alloying for high absorption, optimal EDOS, and long carrier mean free paths (MFPs), as demonstrated in Chapter 5. While alloying Au and Ag did not improve the electron MFP with respect to pure Au, the MFP of the alloys with greater Au content had longer MFPs compared to pure Ag. This suggests that finding the right alloy could lead to improved material properties for SB photodiodes. Considering the extensive parameter space for alloying, there is an exciting opportunity to explore alloys with two or more

elements to find an ideal metal. Alloying metals with long carrier MFPs, such as Au and Ag, with metals that satisfy the optical properties for a FP–like resonance, such as Pt and Fe, would be a good place to start the exploration.

Experimentally exhausting all alloy possibilities may no longer be necessary as advances in machine learning could be incorporated with DFT calculations to accurately predict optical properties, EDOS, and carrier MFPs of any alloy[119, 137, 143]. In addition, there are many methods that have emerged to accurately study hot carrier dynamics in metal films including, but not limited to, ultrafast pump–probe microscopy[144–146], BEEM[104, 147], and heterodyne Kelvin probe force microscopy[106]. The study of materials for hot carrier generation and collection is an exciting topic of interest with entire conferences dedicated to the exploration of novel materials because the applications extend from SB photodetection to photocatalysis, solar energy conversion, and biosensing[148].

It may be noted that the detectivity of the Pt/n–Si diode shown in this manuscript is significantly lower than that of commercial, small bandgap, semiconductor detectors such as InGaAs (Thorlabs - DET05D/M has $D^* = 5.96 \times 10^{10} cmHz^{1/2}/W$). Fortunately, it is possible to increase the detectivity of Schottky photodiodes through applying an external bias to enhance the IQE. An applied bias increases the responsivity by several orders of magnitude, and a Schottky diode device with mA/W responsivity under zero–bias was shown to obtain detectivities on the order of 108 $cmHz^{1/2}/W$ when under bias[16]. While this detectivity is lower than the higher performing, semiconductor commercial IR detectors, it is comparable with commercial photoconductive IR detectors. The early PtSi detec-

tors developed in the 1980s–1990s often operated under an applied bias ranging from 1–10 V when integrated into a focal plane array[4, 12]; a similar read–out scheme will be required for commercial operation of the diodes presented in this manuscript.

6.2 Integrating hot carrier injection into solar cells

While the applications for hot carrier generation and collection are extensive, one further application that we would like to highlight is the integration of hot carrier injection into solar cells. Considering only carrier generation and collection from the metal contact, calculated theoretical efficiency limits show that the maximum obtainable solar conversion efficiency for a SB solar cell is <10%[109, 149]. However, an alternative approach is to incorporate hot carrier diodes into a multi–junction solar cell configuration as shown in Figure 6.1[18]. High energy photons that are commonly lost in a standard solar cell can be absorbed using a metal–insulator–metal (MIM) device. A traditional solar cell can be used to generate power from above bandgap photons. Finally, a SB photodiode can be used to generate power from sub–bandgap photons.

In this device configuration, the FP–like effect can be used for high absorption in both the MIM and SB devices. As shown in Chapter 4, ultrathin metal films can obtain near–perfect absorption using an INZ substrate at any wavelength. Including a thin insulating layer between the metal and INZ films would preserve the optical absorption enhancement while creating a potential barrier for photocurrent collection. It would be beneficial to develop new materials with INZ properties in the UV

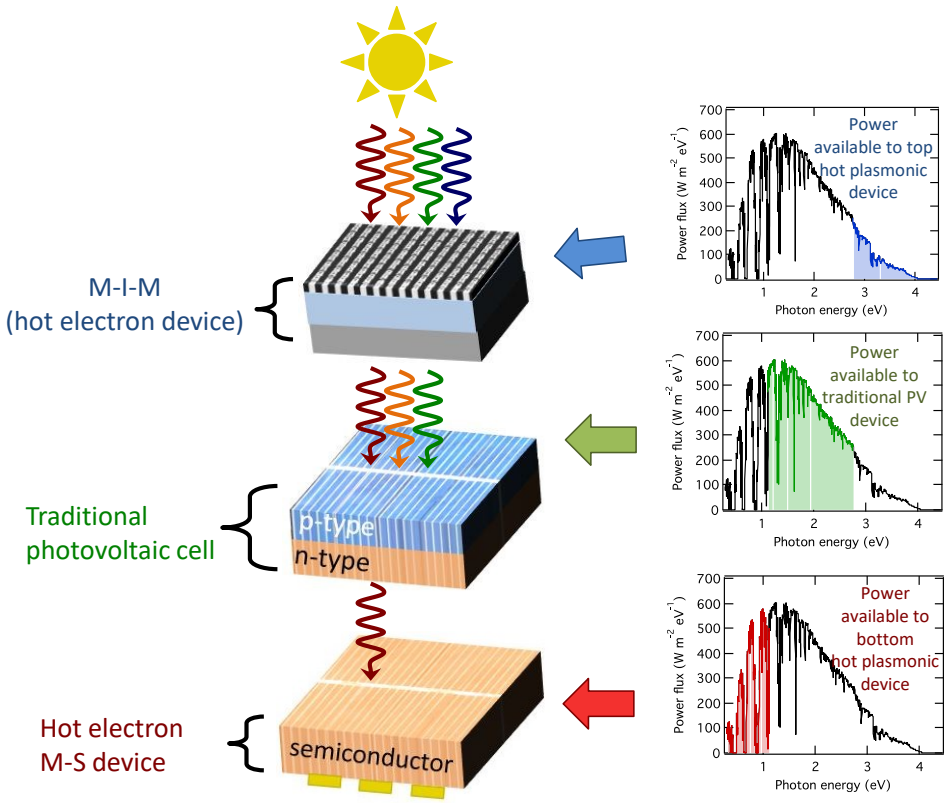

Figure 6.1: A suggested design for incorporating hot carrier generation into a traditional solar cell in order to generate power from the full solar spectrum. This image is taken from reference [18]. High energy photons are absorbed in an MIM device, a tradition solar cell (*i.e.* photovoltaic cell) absorbs the usual bandwidth, and finally all low energy, sub–bandgap photons are collected in the SB photodiode.

to visible wavelength range; however, a few materials already have this property. For example, Ag can be used as an INZ substrate for UV illumination at ∼350 nm (3.5 eV)[40].

There are various methods to split the solar spectrum into each device and connect the device either in series or tandem. Therefore, it would be beneficial to develop a model either using the principles of detailed balance or general device physics to determine the conversion efficiency limits of this and similar device structures[102, 150].

Appendix A: Calculation details

A.1 Fresnel equations for absorption

All analytical calculations for absorption in Chapter 2 were performed using the complex form of the Fresnel equations at normal incidence[99]. The reflection (r) and transmission (t) at an interface with light incident from a material with index $\tilde{n}_u$ to a material of index $\tilde{n}_l$, is determined by:

$$\tilde{r}_{ul} = \frac{\tilde{n}_u - \tilde{n}_l}{\tilde{n}_u + \tilde{n}_l} \tag{A.1}$$

and

$$\tilde{t}_{ul} = \frac{1\tilde{n}_u}{\tilde{n}_u + \tilde{n}_l}. \tag{A.2}$$

The overall reflection and transmission at normal incidence from a homogeneous thin film between two dielectric layers is given by:

$$\tilde{r} = \frac{\tilde{r}_{12} + \tilde{r}_{23} \exp 2i\tilde{\beta}}{1 + \tilde{r}_{12}\tilde{r}_{23} \exp 2i\tilde{\beta}} \tag{A.3}$$

and

$$\tilde{t} = \frac{\tilde{t}_{12}\tilde{t}_{23} \exp i\tilde{\beta}}{1 + \tilde{r}_{12}\tilde{r}_{23} \exp 2i\tilde{\beta}}, \tag{A.4}$$

with

$$\tilde{\beta} = \frac{2\pi}{\lambda_0}\tilde{n}_2 d, \tag{A.5}$$

where λ_0 is the wavelength in air, $\tilde{n}_2$ is the complex refractive index of the ultrathin film, and d is the thin film thickness. The absorption is calculated by subtracting the sum of the thin film's reflectivity and transmissivity from unity:

$$A = 1 - R - T = 1 - |\tilde{r}|^2 - \frac{\tilde{n}_3}{\tilde{n}_1}|\tilde{t}|^2. \tag{A.6}$$

A.2 The transfer matrix method

Maxwell's equations for light traveling through stratified media can be solved using a method called the transfer matrix method[99]. In this method, the characteristic matrix for each layer, $\boldsymbol{M}_j$, is multiplied together to form the characteristic matrix of the full system, $\boldsymbol{M}$. For a TE wave, the characteristic matrix for the jth layer is:

$$\mathbf{M_j} = \begin{bmatrix} cos(\frac{2\pi}{\lambda_0}h_j p_j) & -\frac{i}{p_j}sin(\frac{2\pi}{\lambda_0}h_j p_j) \\ -ip_j sin(\frac{2\pi}{\lambda_0}h_j p_j) & cos(\frac{2\pi}{\lambda_0}h_j p_j) \end{bmatrix}, \tag{A.7}$$

where $p_j = \tilde{n}_j cos\theta_j$, $\tilde{n}_j$ is the complex refractive index of the jth layer, θ_j is the angle that the electromagnetic wave makes with the normal axis as determined by Snell's law, λ_0 is the optical wavelength in free space, and h_j is the film thickness of the jth layer. The total characteristic matrix, $\boldsymbol{M}$, that describes all N distinct

layers can then be calculated as:

$$\mathbf{M} = \prod_{\mathbf{j=1}}^{\mathbf{N}} \mathbf{M_j} = \begin{bmatrix} m_{11} & m_{12} \\ m_{21} & m_{22} \end{bmatrix}, \tag{A.8}$$

and the amplitudes of the reflected, E_r, and transmitted, E_t, waves can be obtained from:

$$\begin{bmatrix} E_0 + E_r \\ p_1(E_0 - E_r) \end{bmatrix} = \mathbf{M} \begin{bmatrix} E_t \\ p_N E_t \end{bmatrix}, \tag{A.9}$$

where 1 and N represent the first and last media in the stratified stack, and E_0, E_r and E_t are the amplitudes of the incident, reflected, and transmitted waves, respectively. This system can then be solved to find the reflection, r, and transmission, t, coefficients:

$$r = \frac{E_r}{E_0} = \frac{(m'_{11} + m'_{12}p_N)p_1 - (m'_{21} + m'_{22}p_N)}{(m'_{11} + m'_{12}p_N)p_1 + (m'_{21} + m'_{22}p_N)} \tag{A.10}$$

and

$$t = \frac{E_t}{E_0} = \frac{2p_1}{(m'_{11} + m'_{12}p_N)p_1 + (m'_{21} + m'_{22}p_N)}. \tag{A.11}$$

Finally, the reflectivity, R, and transmittivity, T, are determined by:

$$R = |r|^2 \quad \text{and} \quad T = \frac{p_N}{p_1}|t|^2. \tag{A.12}$$

For a TM wave, a simple modification is made to the above equations by replacing p_j with $q_j = \frac{cos\theta_j}{\tilde{n}_j}$.

A.3 Thermionic emission model

The barrier height, Φ_B, of a SB device can be calculated from the dark current–voltage characteristics using the thermionic emission model[101]:

$$I = A_{eff}A^{**}T_a^2 exp\left(\frac{-q\Phi_B}{kT_a}\right) exp\left(\frac{q(V - IR_s)}{mkT_a}\right), \tag{A.13}$$

where A_{eff} is the effective area of the device, A^{**} is the Richardson constant (110 $\text{Acm}^{-2}\text{K}^{-2}$ for n–Si[102]), k is the Boltzmann constant, T_a is the absolute temperature, V is the applied voltage, m is the ideality factor, and R_s is the diode series resistance. Solving for V, we have:

$$V = R_s A_{eff} J + m\Phi_B + \frac{m}{\beta} ln(\frac{J}{A^{**}T_a^2}), \tag{A.14}$$

where $\beta = q/kT_a$. Taking the derivative with respect to J and making use of a variable substitution, we can write:

$$\frac{d(V)}{dlnJ} = R_s A_{eff} J + \frac{m}{\beta}, \tag{A.15}$$

which is independent of Φ_B and is linear with J. The intercept then gives the ideality factor, m. Alternatively, we can rewrite Eq A.14 as:

$$V - \frac{n}{\beta} ln(\frac{J}{A^{**}T_a^2}) = R_s A_{eff} J + m\Phi_B \tag{A.16}$$

and define the right side of the equation as $H(J) \equiv V - \frac{n}{\beta} ln(\frac{J}{A^{**}T_a^2})$. Knowing m, we can determine Φ_B from:

$$H(J) = R_s A_{eff} J + m\Phi_B. \tag{A.17}$$

Appendix B: Optical properties of commercial transparent conductive oxide substrates

In this appendix, I document the optical properties of four transparent conductive substrates purchased from MSE Supplies LLC and SPI Supplies. The optical properties and material thicknesses were calculated from the reflection intensity at three different angles as well as the measured transmission using a J. A. Woollam M–2000D Spectroscopic Ellipsometer. These measurements were made in a search for commercially available index–near–zero (INZ) materials with low refractive index in the 1100–1700 nm wavelength range. Only one of these materials had favorable INZ properties in this wavelength range, however this film was too thin to obtain the INZ absorption enhancement effect. To achieve the complete absorption enhancement from an INZ substrate, the INZ material must be > 300 nm thick.

The four films measured here are In:SnO (ITO), Al:ZnO (AZO), and F:SnO (FTO) from MSE Supplies LLC and ITO from SPI Supplies. The optical data for each of the films were fit using a Tauc–Lorentz and Drude model using the CompleteEASE software by J.A. Woollam Ellipsometry Solutions. The full equation used for the fit to the dielectric function is as follows:

$$\epsilon(E_{ph}) = \epsilon_{\text{inf}} + \epsilon_{pole}(E_{ph}) + \epsilon_{T-L}(E_{ph}) + \epsilon_{Drude(RT)}(E_{ph}), \tag{B.1}$$

where E_{ph} is the photon energy, ϵ_{inf} is the macroscopic or background permittivity, ϵ_{pole} is a Lorentz oscillator with zero broadening used to describe the real part of the dielectric function, ϵ_{T-L} is the Tauc–Lorentz oscillator function and $\epsilon_{Drude(RT)}$ is the Drude function determined by the resistivity, R, and mean scattering time, T. More specifically, ϵ_{pole} is defined by the equation:

$$\epsilon_{pole}(E_{ph}) = \frac{Amp}{E_n^2 - E_{ph}^2}, \tag{B.2}$$

where E_n is the central energy of the oscillator and Amp is the oscillator amplitude. The fitting parameters are therefore E_n and Amp. The four fitting parameters for the Tauc–Lorentz oscillator model are the amplitude, Amp, central energy, E_o, broadening, Br, and optical bandgap, E_g, of the oscillator. The equation used to define this oscillator is:

$$\epsilon_{T-L}(E_{ph}) = \epsilon_1 + i\epsilon_2, \tag{B.3}$$

where

$$\epsilon_2(E_{ph}) = \epsilon_2(E_{ph}) = \begin{cases} \left[\frac{AmpE_oBr(E_{ph}-E_g)^2}{(E_{ph}^2-E_o^2)^2+Br^2E_{ph}^2} \cdot \frac{1}{E_{ph}}\right] & E_{ph} > E_g \\ 0 & E_{ph} \leq E_g \end{cases} \tag{B.4}$$

and

$$\epsilon_1(E_{ph}) = \frac{2}{\pi}\int_{E_g}^{\infty} \frac{\zeta\epsilon_2(\zeta)}{\zeta^2 - E_{ph}^2} d\zeta. \tag{B.5}$$

Finally, the Drude model is calculated using:

$$\epsilon_{Drude(RT)}(E_{ph}) = \frac{-\hbar^2}{\epsilon_0\rho(\tau \cdot E_{ph}^2 + i\hbar E_{ph})}, \tag{B.6}$$

where the fitting parameters are the scattering time, τ (in units of fs), and resistivity ρ (in units of $\Omega \cdot cm$). The constants are the reduced Planck's constant, $\hbar$, and the vacuum dielectric constant, ϵ_0.

The other fitting parameters used to obtain the optical properties of these films are the film thickness, roughness, and the average number of reflections through the substrate in order to account for depolarization of the reflected intensity. Below are the results from the fits for each measured film. Note that the thicker films have higher margins of error. This is common when fitting thick films. The error is likely due to thickness dependent optical defects or other inconsistencies in the film that become more significant as the film thickness increases.

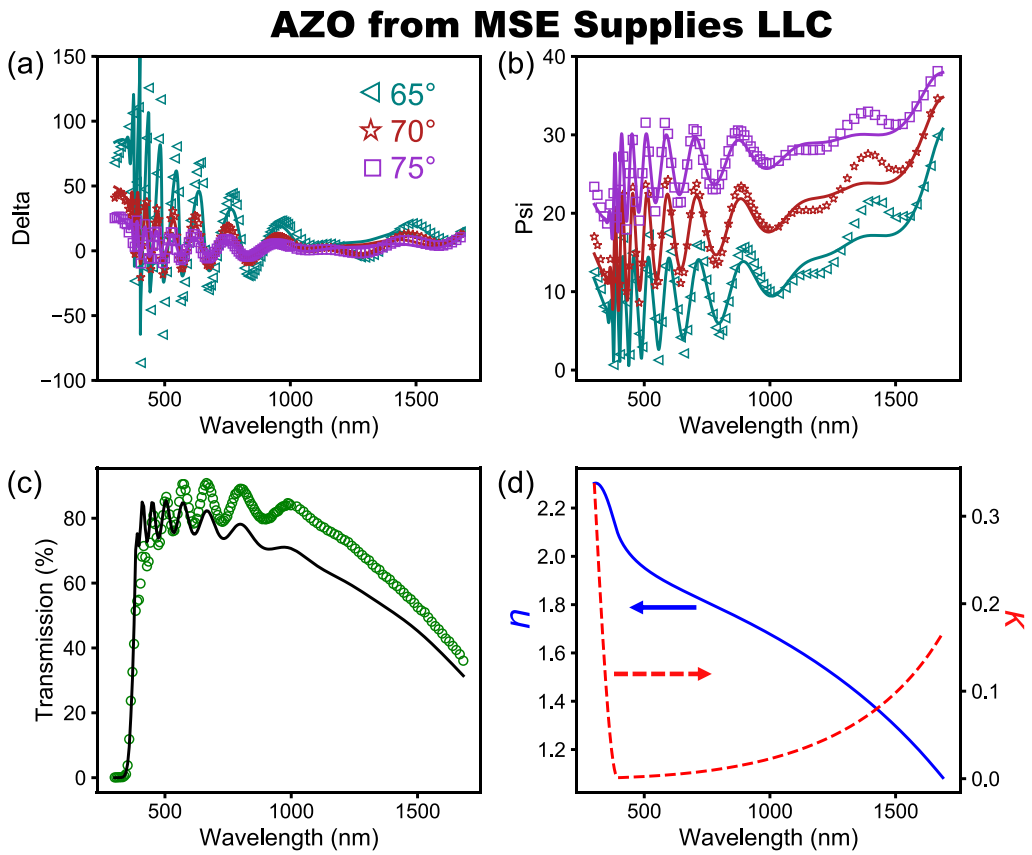

Figure B.1: The fit results for AZO from MSE Supplies, LLC. (a) Delta and (b) Psi values extracted from the reflected intensity measured at angles of 65° (teal triangles), 70° (maroon stars), and 75° (purple squares). The markers indicate the measured results and the solid lines indicate the fit results. (c) The measured (green circles) and fit (black line) transmission. (d) The real (blue solid) and imaginary (red dashed) parts of the refractive indices extracted from the fit. The thickness determined from the optical fit is $\sim$ 904 nm with $\sim$ 13.5 nm roughness. The mean squared error of the fit is 34.35.

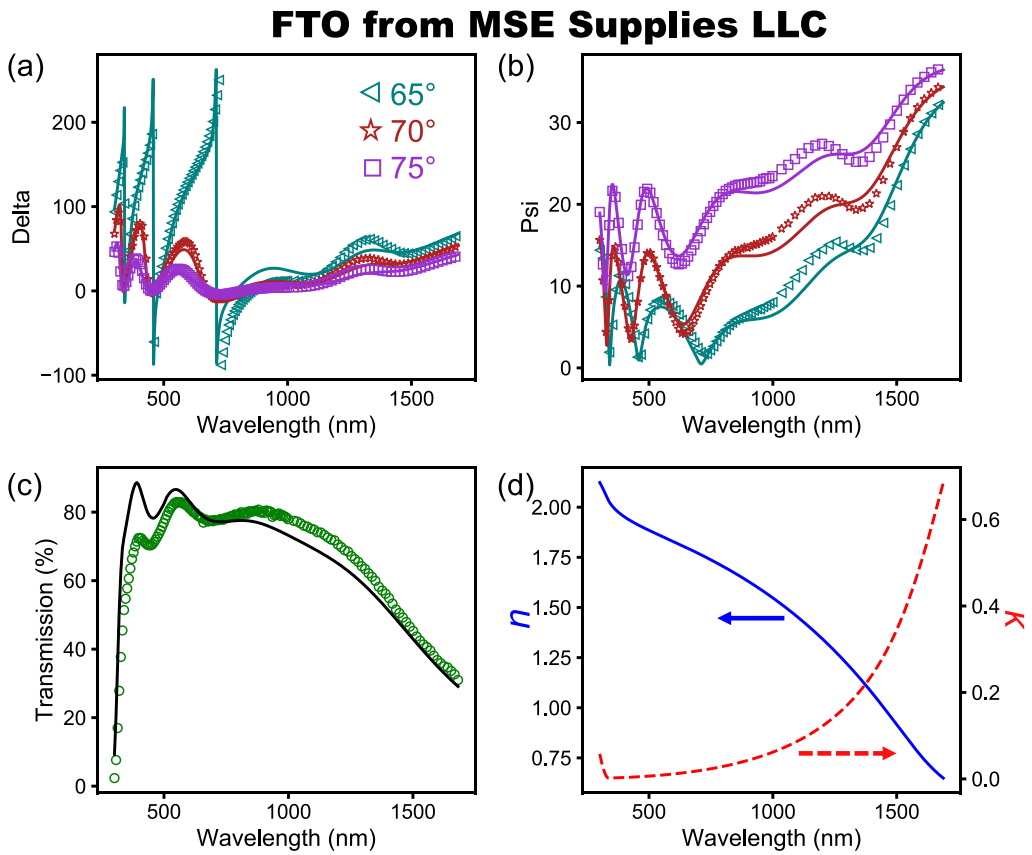

Figure B.2: The fit results for FTO from MSE Supplies, LLC. (a) Delta and (b) Psi values extracted from the reflected intensity measured at angles of 65° (teal triangles), 70° (maroon stars), and 75° (purple squares). The markers indicate the measured results and the solid lines indicate the fit results. (c) The measured (green circles) and fit (black line) transmission. (d) The real (blue solid) and imaginary (red dashed) parts of the refractive indices extracted from the fit. The thickness determined from the optical fit is $\sim$ 300 nm with $\sim$ 21 nm roughness. The mean squared error of the fit is 25.94.

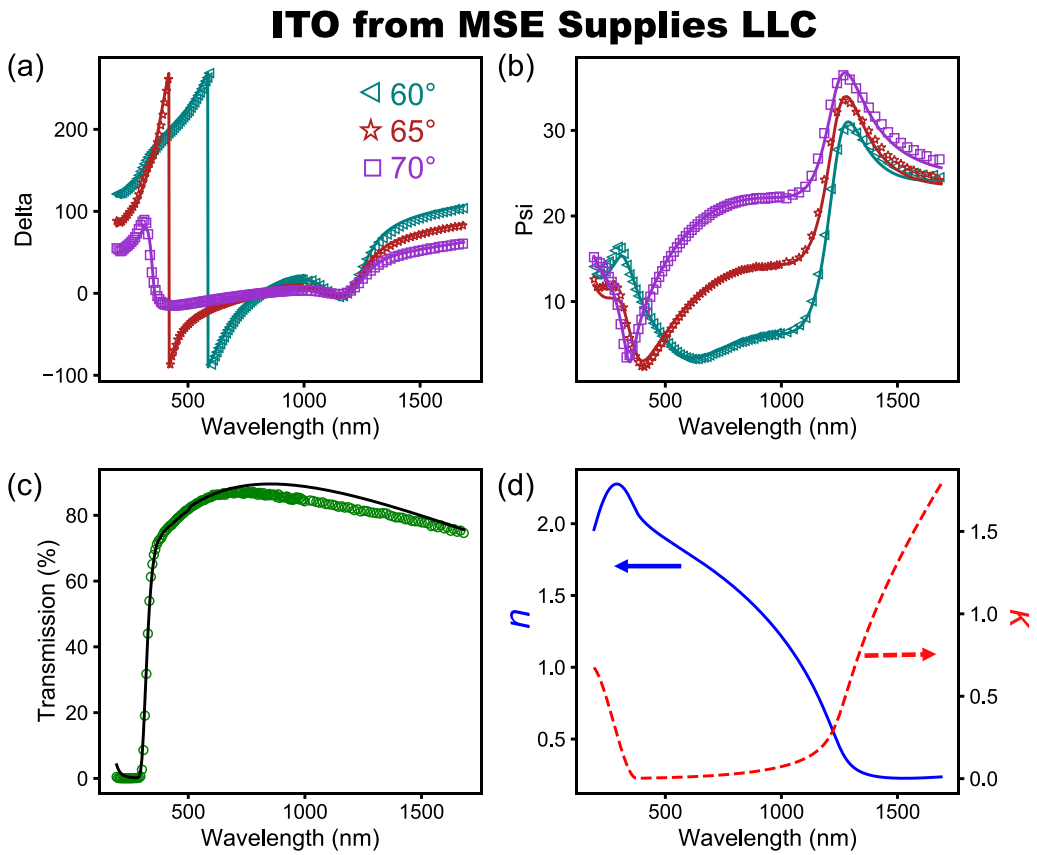

Figure B.3: The fit results for ITO from MSE Supplies, LLC. (a) Delta and (b) Psi values extracted from the reflected intensity measured at angles of 60° (teal triangles), 65° (maroon stars), and 70° (purple squares). The markers indicate the measured results and the solid lines indicate the fit results. (c) The measured (green circles) and fit (black line) transmission. (d) The real (blue solid) and imaginary (red dashed) parts of the refractive indices extracted from the fit. The thickness determined from the optical fit is $\sim$ 45 nm and no roughness was used in this fit. The mean squared error of the fit is 13.083.

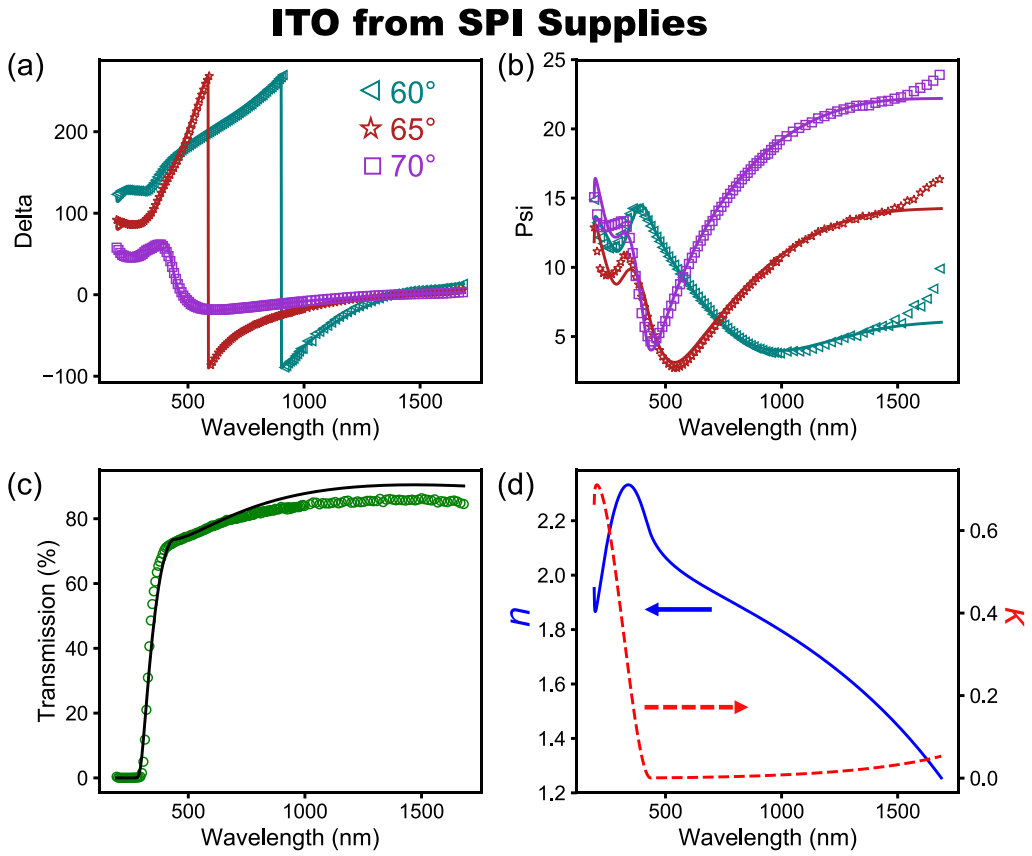

Figure B.4: The fit results for ITO from SPI Supplies. (a) Delta and (b) Psi values extracted from the reflected intensity measured at angles of 60° (teal triangles), 65° (maroon stars), and 70° (purple squares). The markers indicate the measured results and the solid lines indicate the fit results. (c) The measured (green circles) and fit (black line) transmission. (d) The real (blue solid) and imaginary (red dashed) parts of the refractive indices extracted from the fit. The thickness determined from the optical fit is ~ 61 nm and no roughness was used in this fit. The mean squared error of the fit is 13.664.

ϵ_∞	1.485	# Reflections	1
$\epsilon_{pole}Amp$	0.1101	$\epsilon_{pole}E_n$	15
$\epsilon_{T-L}Amp$	246.26	$\epsilon_{T-L}Br$	14.80
$\epsilon_{T-L}E_o$	3.145	$\epsilon_{T-L}E_g$	3.145
$\epsilon_{Drude}\rho$ (Ω cm)^2	0.0005709	$\epsilon_{Drude}\tau$ (fs)^2	6.21

Table B.1: The fit parameters for AZO from MSE Supplies, LLC.

ϵ_∞	2.434	# Reflections	34.5
$\epsilon_{pole}Amp$	1.8417	$\epsilon_{pole}E_n$	11.127
$\epsilon_{T-L}Amp$	172.9074	$\epsilon_{T-L}Br$	22.218
$\epsilon_{T-L}E_o$	3.674	$\epsilon_{T-L}E_g$	4.292
$\epsilon_{Drude}\rho$ (Ω cm)^2	0.00059074	$\epsilon_{Drude}\tau$ (fs)^2	3.810

Table B.2: The fit parameters for FTO from MSE Supplies, LLC.

ϵ_∞	2.105	# Reflections	20
$\epsilon_{pole}Amp$	0.7213	$\epsilon_{pole}E_n$	7.189
$\epsilon_{T-L}Amp$	216.7835	$\epsilon_{T-L}Br$	6.99
$\epsilon_{T-L}E_o$	3.294	$\epsilon_{T-L}E_g$	3.348
$\epsilon_{Drude}\rho$ (Ω cm)^2	0.00016874	$\epsilon_{Drude}\tau$ (fs)^2	7.486

Table B.3: The fit parameters for ITO from MSE Supplies, LLC.

ϵ_∞	2.108	# Reflections	44.646
$\epsilon_{pole}Amp$	0.5136	$\epsilon_{pole}E_n$	6.498
$\epsilon_{T-L}Amp$	195.5116	$\epsilon_{T-L}Br$	5.899
$\epsilon_{T-L}E_o$	2.848	$\epsilon_{T-L}E_g$	3.32
$\epsilon_{Drude}\rho$ (Ω cm)^2	0.00022402	$\epsilon_{Drude}\tau$ (fs)^2	16.452

Table B.4: The fit parameters for ITO from SPI Supplies.

Appendix C: Useful Python code

In this appendix, I present some useful code for calculations made throughout this thesis.

C.1 Python code for calculating absorption using Fresnel equations

```
1  import numpy as np
2
3  def thm(nm, th):
4      return np.arcsin(np.sin(th)/nm)
5
6  def pm(nm, th):
7      return nm * np.cos(thm(nm, th))
8
9  def rmn(nm, nn, th):
10     return (pm(nm, th) - pm(nn, th)) / (pm(nm, th) + pm(nn, th))
11
12 def tmn(nm, nn, th):
13     return (2 * pm(nm, th)) / (pm(nm, th) + pm(nn, th))
14
15 class AnalyticalThinFilmAbs:
16     # Calculates the analytical solution in thin film between
         two mediums.
17     # AnalyticalThinFilmAbs(n1, n2, n3, lam, th1, h)
18
19     def __init__(self, n1, n2, n3, lam, th1, h):
20         self.n1 = n1
21         self.n2 = n2
22         self.n3 = n3
23         self.th1 = th1
24         self.h = h
25         self.lam = lam
26
27     def beta(self):
```

```
28          ratio = ((2 * np.pi)/ self.lam)
29          return ratio * self.n2 * self.h * np.cos(thm(self.n2,
                self.th1))
30
31      def r12(self):
32          return rmn(self.n1, self.n2, self.th1)
33
34      def r21(self):
35          return rmn(self.n2, self.n1, self.th1)
36
37      def r23(self):
38          return rmn(self.n2, self.n3, self.th1)
39
40      def t12(self):
41          return tmn(self.n1, self.n2, self.th1)
42
43      def t23(self):
44          return tmn(self.n2, self.n3, self.th1)
45
46      def t21(self):
47          return tmn(self.n2, self.n1, self.th1)
48
49      def randt(self):
50          num_r = self.r12() + (self.r23() * np.exp(2*1j*self.beta
                ()))
51          num_t = self.t12() * self.t23() * np.exp(1j*self.beta())
52          den = 1 + (self.r12() * self.r23() * np.exp(2*1j*self.
                beta()))
53          return [num_r / den, num_t / den]
54
55      def rm(self, m):
56          exponent = np.exp(2*m*1j*self.beta())
57          return self.t12()*(self.r23()**m)*(self.r21()**(m-1))*
                self.t21()*exponent
58
59      def tm(self, m):
60          exponent = np.exp(1j*(2*m-1)*self.beta())
61          return self.t12()*(self.r23()**(m-1))*(self.r21()**(m-1)
                )*self.t23()*exponent
62
63      def R(self):
64          return (np.abs(self.randt()[0]))**2
65
66      def T(self):
67          pratio = (pm(self.n3, self.th1)/pm(self.n1, self.th1))
68          return pratio*(np.abs(self.randt()[1])**2)
69
```

```
70      def A(self):
71          return 1 - self.R() - self.T()
```

C.2 Python code for calculating absorption using the transfer matrix method

Python has a pre-written package for calculating absorption using the transfer matrix method. See *https://pypi.org/project/tmm* to install the source code and for documentation. As a brief example of how to use this package, the source code for Figure 4.1 is shown below.

```
1  import numpy as np
2  import matplotlib.pyplot as plt
3  import tmm
4  import matplotlib.gridspec as gridspec
5
6  from matplotlib.ticker import (MultipleLocator,
       FormatStrFormatter,
7                                 AutoMinorLocator)
8
9  import sys
10 sys.path.append('Z:/Lisa/Material Data')
11 import LoadMatData as lmd # Database with material data
       extracted from refractiveindex.info
12
13 #%% IMPORT OPTICAL INDICES
14
15 nenz1 = 0.01
16 nenz2 = 0.1
17
18 nsi = lmd.nsi
19 npt = lmd.npt
20 nfe = lmd.nfe
21 ncr = lmd.ncr
22 nti = lmd.nti
23
24 nair = 1.0
```

```
th0 = 0.0

lam_calc= np.linspace(1100, 1600, 250)


#%% SET UP PARAMETERS FOR ABSORPTION CALCULATION

metals = ['Ti', 'Cr', 'Fe', 'Pt']
dmax_air = [6, 5, 6, 3]
dmax_si = [22, 16, 19, 11]

n_index = {'Pt': npt, 'Ti': nti, 'Fe': nfe, 'Cr': ncr, 'Air': nair,
           'ENZ': nenz1, 'Si': nsi}

Abs_calc = {}

def stack_types(m):
    Air_woENZ = 'Air/' + m + '/Air'
    Air_wENZ = 'Air/' + m + '/ENZ'
    Si_woENZ = 'Si/' + m + '/Air'
    Si_wENZ = 'Si/' + m + '/ENZ'
    return [Air_woENZ, Air_wENZ, Si_woENZ, Si_wENZ]

def create_nlist(stack, lam):
    materials = stack.split('/')
    nlist = []
    for material in materials:
        n = n_index[material]
        if callable(n):
            n = n(lam)
        nlist.append(n)
    return nlist

def create_dlist(stack):
    materials = stack.split('/')
    if materials[0] == 'Air':
        dmetal = dmax_air[metals.index(materials[1])]
    elif materials[0] == 'Si':
        dmetal = dmax_si[metals.index(materials[1])]
    else:
        print('Material error: ', materials[0])
    return [np.inf, dmetal, np.inf]

#%% CALCULATE ABSORPTION

# Initiate Abs_calc
```

```
for m in metals:
    Abs_calc[m] = {}
    for stack in stack_types(m):
        Abs_calc[m][stack] = np.array([])

for metal in metals:
    for lam in lam_calc:
        for stack in stack_types(metal):
            nlist = create_nlist(stack, lam)
            dlist = create_dlist(stack)
            tmm_calc = tmm.coh_tmm('p', nlist, dlist, th0, lam)
            Abs = tmm.absorp_in_each_layer(tmm_calc)[1]
            Abs_calc[metal][stack] = np.append(Abs_calc[metal][
                stack], Abs)

#%% PLOT

lamplt = lam_calc*1e-3
cdict = {'Cr': 1.0, 'Pt': 0.75, 'Ti': 0.5, 'Fe': 0.25}

fig = plt.figure(1)
ax = fig.add_subplot(121)
ax.tick_params(which='major', direction='in', length=5.5, width
    =2)
ax.tick_params(which='minor', direction='in', length=3, width
    =1.0)

lgd = []
for m in metals:
    ax.plot(lamplt*1e3, Abs_calc[m]['Air/' + m + '/ENZ']*100, 'b
        ', alpha=cdict[m], lw = 2 )
    ax.plot(lamplt*1e3, Abs_calc[m]['Air/' + m + '/Air']*100, 'k
        ', alpha=cdict[m],
            linestyle = '--', lw = 2)
    lgd.append(m)

plt.ylabel('Absorption (%)')
plt.xlabel('Wavelength (nm)')
plt.xlim([1100, 1600])
plt.ylim([0, 100])
plt.yticks([0, 50, 100])
ax.yaxis.set_minor_locator(MultipleLocator(10))
ax.xaxis.set_minor_locator(MultipleLocator(100))

ax2 = fig.add_subplot(122)
ax2.tick_params(which='major', direction='in', length=5.5, width
    =2)
```

```
ax2.tick_params(which='minor', direction='in', length=3, width
    =1.3)
lgd = []
for m in metals:
    ax2.plot(lamplt*1e3, Abs_calc[m]['Si/' + m + '/ENZ']*100, 'b
        ', alpha=cdict[m], lw = 2)
    ax2.plot(lamplt*1e3, Abs_calc[m]['Si/' + m + '/Air']*100, 'k
        ', alpha=cdict[m] ,
             linestyle = '--', lw = 2)
    lgd.append(m)


plt.xlabel('Wavelength (nm)')
plt.xlim([1100, 1600])
plt.ylim([0, 100])
plt.yticks([0, 50, 100])
ax2.yaxis.set_minor_locator(MultipleLocator(10))
ax2.xaxis.set_minor_locator(MultipleLocator(100))

frame = plt.gca()
for ylabel_i in frame.axes.get_yticklabels():
    ylabel_i.set_fontsize(0.0)
    ylabel_i.set_visible(False)

plt.tight_layout()
```

C.3 Automated IV fit to thermionic emission model for barrier height extraction

This script sets up the function IV_Extract, which takes a .csv file with I–V data and the device active area and returns the Schottky barrier height, ideality factor, and series resistance of the device.

```
## File Purpose: Automate fitting to IV curves for barrier
    height extraction.


import numpy as np
import matplotlib.pyplot as plt
```

```
6  from scipy.optimize import curve_fit
7
8
9  class DarkIV:
10
11     # This class fits IV measured data to thermionic emission
           theory equations
12
13     A2s = 110       # Richardson constant [A/(cm^2 K^2)]
14     T = 293          # temperature [K]
15     k = 1.381e-23    # Boltzmann's constant [J/K]
16     q = 1.602e-19    # charge of an electron [C]
17
18     def __init__(self, V, I, A, Jmin, Jmax=None):
19         self.A = A # Device area
20         self.V = V[V>0] # Voltage
21         self.I = I[V>0] # Current
22         self.J = self.I / self.A
23         self.Jmin = Jmin # Current limit for fit
24         if Jmax:
25             self.Jmax = Jmax
26             self.Jlim = np.logical_and(self.Jmin < self.J, self.
                   J < self.Jmax)
27         else:
28             self.Jlim = self.J > self.Jmin
29         self.kTdq = (DarkIV.k * DarkIV.T)/DarkIV.q
30
31     def lnJ(self):
32         return np.log(self.J)
33
34     def dVdlnJ(self):
35         dV = np.gradient(self.V)
36         dlnJ = np.gradient(self.lnJ())
37         return dV / dlnJ
38
39     def dVdlnJ_fitparams(self):
40
41         def dvdj_fiteq(Jf, RA, ndb):
42             return RA*Jf + ndb
43
44         fitp, error = curve_fit(dvdj_fiteq, self.J[self.Jlim],
               self.dVdlnJ()[self.Jlim])
45
46         return fitp, error
47
48     def dVdlnJ_fit(self):
49         fitparams, err = self.dVdlnJ_fitparams()
```

```
50          return fitparams[0]*self.J + fitparams[1]
51
52      def eta_and_R1(self):
53          fitparams, pcov = self.dVdlnJ_fitparams()
54          eta = fitparams[1] / self.kTdq
55          R1 = fitparams[0] / self.A
56          err = np.sqrt(np.diag(pcov))
57          etaerr = err[1] / self.kTdq
58          R1err = err[0] / self.A
59          return eta, R1, etaerr, R1err
60
61      def H(self):
62          eta, R1, err1, err2 = self.eta_and_R1()
63          nb = (eta*self.kTdq)
64          AT = (DarkIV.A2s*(DarkIV.T**2))
65          return self.V - nb * np.log(self.J/ AT)
66
67      def H_fitparams(self):
68
69          def H_fit(Jf, RA, nphi):
70              return RA*Jf + nphi
71
72          fitp, error = curve_fit(H_fit, self.J[self.Jlim], self.H
                ()[self.Jlim])
73
74          return fitp, error
75
76      def Hfit(self):
77          fitparams, err = self.H_fitparams()
78          return fitparams[0]*self.J + fitparams[1]
79
80      def phiB_and_R2(self):
81          fitparams, pcov = self.H_fitparams()
82          eta, R1, err1, err2 = self.eta_and_R1()
83          phiB = fitparams[1] / eta
84          R2 = fitparams[0] / self.A
85          err = np.sqrt(np.diag(pcov))
86          phiBerr = phiB*np.sqrt(((err[1]/fitparams[1])**2) + ((
                err1 / eta)**2))
87          R2err = err[0] / self.A
88          return phiB, R2, phiBerr, R2err
89
90      def J0(self):
91          phiB, R2, err3, err4 = self.phiB_and_R2()
92          con = self.A*(DarkIV.A2s*(DarkIV.T**2))
93          ex = np.exp(-phiB()/self.kTdq)
94          return con * ex
```

```
95
96  def plot_IV_params(I, V, DIV, Name=None, color='r', fignum=None,
        SaveFolder=None):
97      # This function plots the neceesary IV params for the
            purpose of
98      # degubbing when using the function: IV_Extract
99      if fignum is None:
100         plt.figure(figsize=(12,4))
101     else:
102         plt.figure(fignum, figsize=(12,4))
103     plt.subplot(131)
104     plt.plot(V, I, color=color, marker='o', lw=0)
105     plt.title(Name)
106     plt.ylabel('Current (A)')
107     plt.xlabel('Voltage (V)')
108
109     plt.subplot(132)
110     plt.plot(DIV.J, DIV.dVdlnJ(), color=color, marker='o', lw=0)
111     plt.plot(DIV.J, DIV.dVdlnJ_fit(), 'k', lw=2)
112     plt.title('Eta: {:0.2f}, R1: {:0.2f}'.format(DIV.eta_and_R1
            ()[0],DIV.eta_and_R1()[1]))
113     plt.xlabel('J (A/$cm^2$)')
114     plt.ylabel(r'$ \frac{\delta V}{\delta (ln(J))} $')
115
116     plt.subplot(133)
117     plt.plot(DIV.J, DIV.H(), color=color, marker='o', lw=0)
118     plt.plot(DIV.J, DIV.Hfit(), 'k', lw=2)
119     plt.title('PhiB: {:0.2f}, R2: {:0.2f}'.format(DIV.
            phiB_and_R2()[0], DIV.phiB_and_R2()[1]))
120     plt.xlabel('J (A/$cm^2$)')
121     plt.ylabel(r'$ V - \frac{\eta kT}{q} Log(J/AT) $')
122
123     plt.tight_layout()
124
125     if SaveFolder is not None:
126         plt.savefig(SaveFolder+Name+' IV Analysis.jpg', dpi=500)
127         plt.savefig(SaveFolder+Name+' IV Analysis.svg', format='
                svg')
128     return
129
130 def print_IV_params(D):
131     # This function prints the fit parameters for the purpose of
132     # degubbing when using the function: IV_Extract
133     print('PhiB: %0.2f, Eta: %0.2f' %(D.phiB_and_R2()[0], D.
            eta_and_R1()[0]))
134     print('PhiB Err: %0.2f, Eta Err: %0.2f' %(D.phiB_and_R2()
            [2], D.eta_and_R1()[2]))
```

```
135
136     print('R2: %0.2f, R1: %0.2f' %(D.phiB_and_R2()[1], D.
            eta_and_R1()[1]))
137     print('R2 Err: %0.2f, R1 Err: %0.2f' %(D.phiB_and_R2()[3],D.
            eta_and_R1()[3]))
138     return
139
140
141 def IV_Extract(filename, devicearea, debugMode=False):
142
143     # Extract current and voltage from data file
144     V, I = np.loadtxt(filename, delimiter=',', usecols=(0,1),
            unpack=True,
145                       skiprows=1)
146
147     # We only use forward bias for extracting barrier height
148     V_f = V[V>0] # Forward voltage
149     I_f = I[V>0] # Forward current
150     J_f = I_f/devicearea # Forward current density
151
152     ##First we want to find Jmin. Removing the current around V
            =0 from the fit.
153
154     min_index = 0 # Test index
155     dIV_no_fit_region = DarkIV(V_f, I_f, devicearea, 0)
156
157     dVdlnJ_grad = np.gradient(dIV_no_fit_region.dVdlnJ(),
            dIV_no_fit_region.J)
158     dVdlnJ_grad_diff = np.diff(dVdlnJ_grad)
159
160     while np.abs(dVdlnJ_grad_diff[min_index]) > 1:
161         min_index += 1
162
163         if min_index > len(V_f)-3:
164             print('Jmin not found.')
165             print('IV curve does not follow Schottky behavior.')
166             break
167
168     min_index += 2
169     Jmin = J_f[min_index]
170     if debugMode:
171         print(r'Jmin found: %0.4f' %(Jmin, dVdlnJ_grad[min_index
                ]))
172
173
174     ##Then we to progressively fit the remaining data until the
            slope
```

```
175     ##deviates by 2%.
176
177     max_index = min_index+5
178
179     dVdlnJ_plus2perc = dVdlnJ_grad[max_index] + dVdlnJ_grad[
            max_index]*0.2
180     dVdlnJ_minus2perc = dVdlnJ_grad[max_index] - dVdlnJ_grad[
            max_index]*0.2
181
182     if debugMode:
183         print('dVdlnJ slope at start: %0.4f' %(dVdlnJ_grad[
                max_index]))
184
185     while (dVdlnJ_grad[max_index] < dVdlnJ_plus2perc and
186             dVdlnJ_grad[max_index] > dVdlnJ_minus2perc):
187
188         max_index += 1
189
190         if max_index > len(V_f)-3:
191             break
192
193
194     dIV_final = DarkIV(V_f, I_f, devicearea, Jmin, Jmax = J_f[
            max_index])
195
196     if debugMode:
197         print('Fit Complete with Jmax: %0.5f' %(J_f[max_index]))
198         print('dVdlnJ slope %0.4f' %(dVdlnJ_grad[max_index]))
199         print_IV_params(dIV_final)
200         plot_IV_params(I, V, dIV_final)
201
202     return {'I': I, 'V': V, 'DIV': dIV_final,
203             'PhiB': dIV_final.phiB_and_R2()[0],
204             'Eta': dIV_final.eta_and_R1()[0],
205             'PhiB Error': dIV_final.phiB_and_R2()[2],
206             'Eta Error': dIV_final.eta_and_R1()[2],
207             'R1': dIV_final.eta_and_R1()[1],
208             'R1 Error': dIV_final.eta_and_R1()[3],
209             'R2': dIV_final.phiB_and_R2()[1],
210             'R2 Error': dIV_final.phiB_and_R2()[3],
211             'Jmin': Jmin, 'Jmax': J_f[max_index]}
```

C.4 Code used for data analysis used to determine electron attenuation length in Chapter 5

```
import tmm, os, sys

import numpy as np
import scipy.interpolate as interpolate
import matplotlib.pyplot as plt
import scipy.optimize as opt
import scipy.signal as sg

sys.path.append('Z:/Lisa/UsefulScripts')
import PlotFuncs as pf
from Automate_IV_Fit import plot_IV_params, print_IV_params,
    IV_Extract

sys.path.append('Z:/Lisa/Material Data')
import LoadMatData as lmd # Database with optical data extracted
     from refractiveindex.info

prop_cycle = plt.rcParams['axes.prop_cycle']
colors = prop_cycle.by_key()['color']

#%% ELLIPSOMETRY DATA

REFERENCEFOLDER = 'Z:/Lisa/Au_Ag_films/
    AttenuationLengthMeasurements/'


class Load_Ellipsometry_Data():

    ## Load and plot ellipsometry data for a given MetalName at
        each
    ## film thickness in FilmNames.
    ##
    ## MetalName: Name of pure metal or alloy
    ## FilmNames: List of film names (ex. ['10s', '15s'])

    def __init__(self, MetalName, FilmNames):
        self.MetalName = MetalName
        self.FilmNames = FilmNames


    def LoadFileData(self, FilmName):
```

```
38          ReferenceFolder = REFERENCEFOLDER + '/' + self.MetalName
                +'/' + 'Ellipsometry/'
39          FileName = ReferenceFolder + self.MetalName + '_' +
                FilmName +'_nk.csv'
40          wavelength, n, k = np.loadtxt(FileName, delimiter=',',
                usecols=(0,1,2),
41                                        skiprows=2, unpack=True)
42          return wavelength, n, k
43
44
45      def LoadNKData2Dict(self):
46
47          nk_raw_data = {}
48
49          for filmname in self.FilmNames:
50              wavelength, n, k = self.LoadFileData(filmname)
51              nk_raw_data[filmname] = {'lam': wavelength, 'n': n,
                    'k': k}
52
53          nk_interp_data = {}
54
55          for filmname in self.FilmNames:
56              n_interpolated = interpolate.interp1d(nk_raw_data[
                    filmname]['lam'],
57                                                    nk_raw_data[
                                                          filmname]['
                                                          n'])
58              k_interpolated = interpolate.interp1d(nk_raw_data[
                    filmname]['lam'],
59                                                    nk_raw_data[
                                                          filmname]['
                                                          k'])
60              nk_interp_data[filmname] = {'n': n_interpolated, 'k'
                    : k_interpolated}
61
62          return nk_interp_data
63
64
65      def PlotAllNKData(self, WavelengthList, SaveImage=False,
66                        FigureNumber=None, ImageName=None):
67
68          nk_data = self.LoadNKData2Dict()
69
70          pf.init_plotting()
71
72          plt.figure(FigureNumber, figsize=(8,4))
73          plt.subplot(121)
```

```
74
75          for index, key in enumerate(self.FilmNames):
76              plt.plot(WavelengthList, nk_data[key]['n'](
                    WavelengthList),
77                       color=colors[index], lw=2)
78
79          plt.ylabel('n')
80          plt.xlabel('Wavelength (nm)')
81
82
83          plt.subplot(122)
84
85          for index, key in enumerate(self.FilmNames):
86              plt.plot(WavelengthList, nk_data[key]['k'](
                    WavelengthList),
87                       color=colors[index], lw=2)
88
89          plt.ylabel('$\kappa$')
90          plt.xlabel('Wavelength (nm)')
91          plt.legend(self.FilmNames)
92
93          plt.tight_layout()
94
95          if SaveImage:
96              if ImageName == None:
97                  print('No image name given. Image name set to: "
                        Unknown"')
98                  ImageName='Unknown'
99              plt.savefig(ImageName+'.jpg', dpi = 500)
100             plt.savefig(ImageName+'.svg', format='svg')
101
102         return
103
104
105     def PlotOneFilmNKData(self, FilmName, WavelengthList,
            SaveImage=False,
106                           FigureNumber=None, ImageName=None):
107
108         nk_data = self.LoadNKData2Dict()
109
110         pf.init_plotting()
111
112         plt.figure(FigureNumber, figsize=(4,3))
113         plt.plot(WavelengthList, np.real(nk_data[FilmName](
                WavelengthList)),
114                  color='b', lw=2)
```

```
115         plt.plot(WavelengthList, np.imag(nk_data[FilmName](
                WavelengthList)),
116                 color='orange', linestyle='--', lw=2)
117         plt.xlabel('Wavelength (nm)')
118         plt.ylabel('n (solid) & $\kappa$ (dashed)')
119         plt.title(FilmName)
120 
121         if SaveImage:
122             if ImageName == None:
123                 print('No image name given. Image name set to: "
                        Unknown"')
124                 ImageName='Unknown'
125             plt.savefig(ImageName+'.jpg', dpi = 500)
126             plt.savefig(ImageName+'.svg', format='svg')
127 
128         return
129 
130 
131 def Calculate_ATR_FromEllipsometry(MetalName, ThicknessDict,
132                                    WavelengthList, PlotData=False,
                                           FileName=None):
133 
134     ## Calculate Absorption, Transmission, or Reflection from
            Ellipsometry data
135 
136     FilmNames = list(ThicknessDict.keys())
137 
138     metal_load_nk_data = Load_Ellipsometry_Data(MetalName,
            FilmNames)
139     MetalNK = metal_load_nk_data.LoadNKData2Dict()
140 
141     Reflectivity = {}
142     Transmission = {}
143     Absorption = {}
144 
145     for FilmName in FilmNames:
146         Reflectivity_List = []
147         Transmitivity_List = []
148 
149         nmetal = lambda wave: MetalNK[FilmName]['n'](wave) + 1j*
                MetalNK[FilmName]['k'](wave)
150         dlist = [np.inf, ThicknessDict[FilmName], np.inf]
151         n_list = lambda wave: [1.0, nmetal(wave), lmd.nsi(wave)]
152         th0 = 0 # Angle of incidence is 0
153 
154         for wave in WavelengthList:
155             nlist = n_list(wave)
```

```
156
157                 SolveTMM = tmm.coh_tmm('p', nlist, dlist, th0, wave)
158                 Transmitivity_List.append(SolveTMM['T'])
159                 Reflectivity_List.append(SolveTMM['R'])
160
161             Reflectivity[FilmName] = np.array(Reflectivity_List)
162             Transmission[FilmName] = np.array(Transmitivity_List)
163             Absorption[FilmName] = 1 - Reflectivity[FilmName] -
                    Transmission[FilmName]
164
165     return {'A': Absorption, 'R': Reflectivity, 'T':
            Transmission}
166
167 #%% FUNCTIONS NEEDED FOR MEASURING ABSORPTION
168
169 def PercentPowerMeasured(fb, fsamp):
170     lam_b, PsPr_b = np.loadtxt(fb, delimiter=',', usecols=(0,5),
171                                skiprows=1, unpack=True)
172     PsPr_b_interp = interpolate.interp1d(lam_b, PsPr_b,
173                                          fill_value='
                                                extrapolate')
174     lam_s, PsPr_s = np.loadtxt(fsamp, delimiter=',', usecols
            =(0,5),
175                                skiprows=1, unpack=True)
176     RT = PsPr_s*(1/PsPr_b_interp(lam_s))
177     return lam_s, RT
178
179
180
181 def QuickCheckMeasuredData(FileName, BaselineFileName, MetalName
        , FilmName,
182                    FilmThickness, WavelengthList,
183                    isTransmission=False, isReflection=False):
184
185
186     ## Check if data you just took matches the ellipsometry data
            .
187
188
189     Abs_Ref_Trans = Calculate_ATR_FromEllipsometry(MetalName, {
            FilmName:
190                                                    FilmThickness},
                                                        WavelengthList)
191
192     Wavelengths, Measured = PercentPowerMeasured(
            BaselineFileName, FileName)
193
```

```
194         plt.figure(figsize=(4,3))
195         plt.plot(Wavelengths, Measured*100, color='r', marker='o',
                lw=0)
196         plt.xlim([1200,1500])
197         plt.xlabel('Wavelength (nm)')
198         plt.title(FilmName)
199 
200         if isTransmission:
201             plt.plot(WavelengthList, Abs_Ref_Trans['T'][FilmName
                    ]*100, 'r', lw=2)
202             plt.ylim([0, 30])
203             plt.ylabel('Transmission (%)')
204         if isReflection:
205             plt.plot(WavelengthList, Abs_Ref_Trans['R'][FilmName
                    ]*100, 'r', lw=2)
206             plt.ylim([60, 100])
207             plt.ylabel('Reflection (%)')
208 
209         return Wavelengths, Measured
210 
211 
212 #%% ABSORPTION ANALYSIS
213 
214 class Absorption_Analysis():
215 
216         def __init__(self, MetalName, ThicknessDict):
217 
218             ## MetalName: Name given to the folders of each metal
                    type.
219             ## ThicknessDict: Dictionary with measured thicknesses
                    for each film.
220 
221             self.MetalName = MetalName
222             self.ThicknessDict = ThicknessDict
223             self.FilmNames = list(ThicknessDict.keys())
224             self.Absorption_dir = REFERENCEFOLDER+self.MetalName+'/
                    Absorption/FinalData/'
225 
226         def LoadDataFromFiles(self):
227 
228             ## Load data into dictionary where key 'R' is
                    reflectivity,
229             ## 'T' is transmission and 'A' is absorption.
230 
231 
232             ListFileNames = os.listdir(self.Absorption_dir)
233 
```

```
234         Baseline = [file for file in ListFileNames if 'Baseline'
                in file][0]
235         Baseline = self.Absorption_dir+Baseline
236 
237         RawOpticalData = {'R': {}, 'T': {}, 'A': {}}
238 
239         for filmname in self.FilmNames:
240 
241             FileSearch = self.MetalName+'_'+filmname
242             ReflectivityData = [file for file in ListFileNames
                    if
243                                 'Reflectivity_'+FileSearch in
                                        file][0]
244             ReflectivityData = self.Absorption_dir+
                    ReflectivityData
245             TransmissionData = [file for file in ListFileNames
                    if
246                                 'Transmission_'+FileSearch in
                                        file][0]
247             TransmissionData = self.Absorption_dir+
                    TransmissionData
248 
249             lam_R_data, R_data = PercentPowerMeasured(Baseline,
                    ReflectivityData)
250             lam_T_data, T_data = PercentPowerMeasured(Baseline,
                    TransmissionData)
251 
252             RawOpticalData['R'][filmname] = [lam_R_data, R_data]
253             RawOpticalData['T'][filmname] = [lam_T_data, T_data]
254             RawOpticalData['A'][filmname] = [lam_T_data, 1 -
                    R_data - T_data]
255 
256         return RawOpticalData
257 
258     def ProcessAndInterpolate(self):
259 
260         ## Filter the raw data using a Savitzy-Golay filter.
261 
262 
263         RawOpticalData = self.LoadDataFromFiles()
264 
265         ProcessedData = {'R': {}, 'T': {}}
266 
267         Abs_Interp = {}
268 
269         for filmname in self.FilmNames:
270 
```

```
271             def FixExtremes(TorRlist):
272                 # Make sure Reflectivity is not > 1 and
                        Transmission is not < 0
273                 outlist = []
274                 for index, item in enumerate(TorRlist):
275                     if item > 1:
276                         outlist.append(1)
277                     elif item < 0:
278                         outlist.append(0)
279                     else:
280                         outlist.append(item)
281                 return np.array(outlist)
282
283             T_savgol = sg.savgol_filter(RawOpticalData['T'][
                    filmname][1],11,2)
284             ProcessedData['T'][filmname] = [RawOpticalData['T'][
                    filmname][0],
285                                             FixExtremes(
                                                    T_savgol)]
286
287
288             R_savgol = sg.savgol_filter(RawOpticalData['R'][
                    filmname][1],11,2)
289             ProcessedData['R'][filmname] = [RawOpticalData['R'][
                    filmname][0],
290                                             FixExtremes(
                                                    R_savgol)]
291
292             T_interp = interpolate.interp1d(RawOpticalData['T'][
                    filmname][0],
293                                             ProcessedData['T'][
                                                    filmname][1],
294                                             fill_value='
                                                    extrapolate')
295             R_interp = interpolate.interp1d(RawOpticalData['R'][
                    filmname][0],
296                                             ProcessedData['R'][
                                                    filmname][1],
297                                             fill_value='
                                                    extrapolate')
298             Abs_Interp[filmname] = {'R': R_interp, 'T': T_interp
                    }
299
300         return {'Interpolated': Abs_Interp, 'Processed':
                ProcessedData}
301
302     def PlotAllIndividual(self, WavelengthList, SaveFig=False):
```

```
303
304         pf.init_plotting()
305         RawOpticalData = self.LoadDataFromFiles()
306         FromEllipsometry = Calculate_ATR_FromEllipsometry(self.
                MetalName,
307                                                           self.ThicknessDict,
                                                              WavelengthList)
308
309         for index, filmname in enumerate(self.FilmNames):
310             plt.figure(index, figsize=(12,4))
311             plt.subplot(131)
312             plt.plot(WavelengthList, FromEllipsometry['T'][
                    filmname]*100,
313                      color=colors[index], lw=2)
314             plt.plot(RawOpticalData['T'][filmname][0],
                    RawOpticalData['T'][filmname][1]*100,
315                      color=colors[index], marker='o', lw=0)
316             plt.xlabel('Wavelength (nm)')
317             plt.ylabel('Transmission (%)')
318             plt.xlim([1200, 1500])
319             plt.ylim([0, 30])
320
321             plt.subplot(132)
322             plt.plot(WavelengthList, FromEllipsometry['R'][
                    filmname]*100,
323                      color=colors[index], lw=2)
324             plt.plot(RawOpticalData['R'][filmname][0],
                    RawOpticalData['R'][filmname][1]*100,
325                      color=colors[index], marker='o', lw=0)
326             plt.title(filmname)
327             plt.xlabel('Wavelength (nm)')
328             plt.ylabel('Reflectivity (%)')
329             plt.xlim([1200, 1500])
330             plt.ylim([60, 100])
331
332             plt.subplot(133)
333             plt.plot(WavelengthList, FromEllipsometry['A'][
                    filmname]*100,
334                      color=colors[index], lw=2)
335             plt.plot(RawOpticalData['A'][filmname][0],
                    RawOpticalData['A'][filmname][1]*100,
336                      color=colors[index], marker='o', lw=0)
337             plt.xlabel('Wavelength (nm)')
338             plt.ylabel('Absorption (%)')
339             plt.xlim([1200, 1500])
340             plt.ylim([0,20])
341
```

```
342             plt.tight_layout()
343
344             if SaveFig:
345                 plt.savefig(self.Absorption_dir+filmname+'.jpg',
                        dpi = 500)
346                 plt.savefig(self.Absorption_dir+filmname+'.svg',
                        format='svg')
347
348         return
349
350     def PlotAllRawData(self, FileName=None):
351
352         pf.init_plotting()
353         RawOpticalData = self.LoadDataFromFiles()
354
355         plt.figure(figsize=(12,4))
356
357         plt.subplot(131)
358         plt.xlabel('Wavelength (nm)')
359         plt.ylabel('Transmission (%)')
360         plt.title(r'Normal Incidence')
361         plt.xlim([1200, 1500])
362         plt.ylim([0, 30])
363
364         for index, filmname in enumerate(self.FilmNames):
365             plt.plot(RawOpticalData['T'][filmname][0],
                    RawOpticalData['T'][filmname][1]*100,
366                     color=colors[index], marker='o', lw=0)
367
368         plt.subplot(132)
369         plt.xlabel('Wavelength (nm)')
370         plt.ylabel('Reflectivity (%)')
371         plt.title(r'10$\degree$ Incidence')
372         plt.xlim([1200, 1500])
373         plt.ylim([50, 100])
374
375         for index, filmname in enumerate(self.FilmNames):
376             plt.plot(RawOpticalData['R'][filmname][0],
                    RawOpticalData['R'][filmname][1]*100,
377                     color=colors[index], marker='o', lw=0)
378
379         plt.subplot(133)
380         plt.xlabel('Wavelength (nm)')
381         plt.ylabel('Absorption (%)')
382         plt.xlim([1200, 1500])
383         plt.ylim([0, 20])
384
```

```
385             for index, filmname in enumerate(self.FilmNames):
386                 plt.plot(RawOpticalData['A'][filmname][0],
                        RawOpticalData['A'][filmname][1]*100,
387                             color=colors[index], marker='o', lw=0)
388
389             plt.tight_layout()
390
391             if FileName is not None:
392                 plt.savefig(self.Absorption_dir+FileName+'.jpg', dpi
                        = 500)
393                 plt.savefig(self.Absorption_dir+FileName+'.svg',
                        format='svg')
394
395             return
396
397
398         def PlotAllEllipsometry(self, WavelengthList, FileName=None)
            :
399
400             pf.init_plotting()
401             FromEllipsometry = Calculate_ATR_FromEllipsometry(self.
                    MetalName,
402                                                 self.ThicknessDict,
                                                        WavelengthList)
403
404             plt.figure(figsize=(12,4))
405
406             plt.subplot(131)
407             plt.xlabel('Wavelength (nm)')
408             plt.ylabel('Transmission (%)')
409             plt.title(r'Normal Incidence')
410             plt.xlim([1200, 1500])
411             plt.ylim([0, 30])
412
413             for index, filmname in enumerate(self.FilmNames):
414                 plt.plot(WavelengthList, FromEllipsometry['T'][
                        filmname]*100,
415                             color=colors[index], lw=2)
416
417             plt.subplot(132)
418             plt.xlabel('Wavelength (nm)')
419             plt.ylabel('Reflectivity (%)')
420             plt.title(r'10$\degree$ Incidence')
421             plt.xlim([1200, 1500])
422             plt.ylim([50, 100])
423
424             for index, filmname in enumerate(self.FilmNames):
```

```
425             plt.plot(WavelengthList, FromEllipsometry['R'][
                    filmname]*100,
426                     color=colors[index], lw=2)
427
428         plt.subplot(133)
429         plt.xlabel('Wavelength (nm)')
430         plt.ylabel('Absorption (%)')
431         plt.xlim([1200, 1500])
432         plt.ylim([0, 20])
433
434         for index, filmname in enumerate(self.FilmNames):
435             plt.plot(WavelengthList, FromEllipsometry['A'][
                    filmname]*100,
436                     color=colors[index], lw=2)
437
438         plt.tight_layout()
439
440         if FileName is not None:
441             plt.savefig(self.Absorption_dir+FileName+'.jpg', dpi
                    = 500)
442             plt.savefig(self.Absorption_dir+FileName+'.svg',
                    format='svg')
443
444         return
445
446 #%% CURRENT-VOLTAGE ANALYSIS
447
448 class IV_Analysis():
449
450     def __init__(self, MetalName, ThicknessDict):
451
452         ## MetalName: Name given to the folders of each metal
                type.
453         ## ThicknessDict: Dictionary with measured thicknesses
                for each film.
454
455         self.MetalName = MetalName
456         self.ThicknessDict = ThicknessDict
457         self.FilmNames = list(ThicknessDict.keys())
458         self.IV_dir = REFERENCEFOLDER+self.MetalName+'/IV/
                FinalData/'
459
460
461     def Fit_Extract_All(self):
462
463         ListFileNames = os.listdir(self.IV_dir)
464         DeviceArea = np.pi*((0.762/2)**2) # cm^2
```

```
465
466             FitResults = {}
467
468             for filmname in self.FilmNames:
469                 FileName = [file for file in ListFileNames if
                        filmname and '.csv' in file][0]
470                 FitResults[filmname] = IV_Extract(self.IV_dir+
                        FileName, DeviceArea)
471
472             return FitResults
473
474
475         def PlotAllIndividual(self, SaveFig=False):
476
477             pf.init_plotting()
478
479             if SaveFig:
480                 SaveFolder = self.IV_dir
481             else:
482                 SaveFolder = None
483
484             FitResults = self.Fit_Extract_All()
485
486             for index, filmname in enumerate(self.FilmNames):
487                 plot_IV_params(FitResults[filmname]['I'], FitResults
                        [filmname]['V'],
488                                FitResults[filmname]['DIV'], filmname
                                    , fignum=index,
489                                color=colors[index], SaveFolder=
                                    SaveFolder)
490
491                 print_IV_params(FitResults[filmname]['DIV'])
492
493             return
494
495         def PlotAllIV(self, SaveFig=False):
496
497             pf.init_plotting()
498             FitResults = self.Fit_Extract_All()
499
500             plt.figure(figsize=(8,4))
501
502             plt.subplot(121)
503             plt.xlabel('V (V)')
504             plt.ylabel('I (A)')
505             plt.xlim([-1,1])
506
```

```
507         for index, filmname in enumerate(self.FilmNames):
508             plt.plot(FitResults[filmname]['V'], FitResults[
                    filmname]['I'],
509                      color=colors[index], lw=2)
510 
511         plt.subplot(122)
512         plt.xlabel('V (V)')
513         plt.ylabel('I (A)')
514         plt.xlim([-1,1])
515 
516         for index, filmname in enumerate(self.FilmNames):
517             plt.semilogy(FitResults[filmname]['V'], np.abs(
                    FitResults[filmname]['I']),
518                      color=colors[index], lw=2)
519 
520         plt.tight_layout()
521 
522         if SaveFig:
523             plt.savefig(self.IV_dir+self.MetalName+' All IV.jpg'
                        , dpi=500)
524             plt.savefig(self.IV_dir+self.MetalName+' All IV.svg'
                        , format='svg')
525 
526         return
527 
528 #%% RESPONSIVITY ANALYSIS
529 
530 class Responsivity_Analysis():
531 
532     def __init__(self, MetalName, ThicknessDict,
            ThicknessCalibrated):
533 
534         ## MetalName: Name given to the folders of each metal
                type.
535         ## ThicknessDict: Dictionary with measured thicknesses
                for each film.
536         ## ThicknessCalibrated: Dict to verify that the data in
                files are
537         ## properly calibrated. Ex. {'10s': True, '20s': False}
538 
539         self.MetalName = MetalName
540         self.ThicknessCalibrated = ThicknessCalibrated
541         self.ThicknessDict = ThicknessDict
542         self.FilmNames = list(ThicknessDict.keys())
543         self.Resp_dir = REFERENCEFOLDER+self.MetalName+'/
                Responsivity/FinalData/'
544 
```

```
545     def LoadRespDataFromFiles(self):
546         ListFileNames = os.listdir(self.Resp_dir)
547 
548         # If one of the files is not calibrated correctly, load
                calibration.
549         if False in self.ThicknessCalibrated.values():
550             PsPrCalibrationFile = [file for file in
                    ListFileNames if
551                                    'PsPrCal' in file][0]
552             PsPrCalibrationFile = self.Resp_dir+
                    PsPrCalibrationFile
553             lam_pspr, pspr_cal = np.loadtxt(PsPrCalibrationFile,
                     delimiter=',',
554                                             usecols=(0,1), skiprows=1,
                                                unpack=True)
555             PsPr_Calibration = interpolate.interp1d(lam_pspr,
                    pspr_cal,
556                                                     fill_value='
                                                        extrapolate
                                                        ')
557 
558             PrCalibrationFile = 'Z:/Lisa/
                    Ge_Calibration_FDG03_16030141.csv'
559             lam_pr, eta_cal = np.loadtxt(PrCalibrationFile,
                    delimiter=',',
560                                          usecols=(0,1), skiprows=1,
                                             unpack=True)
561             Pr_Calibration = interpolate.interp1d(lam_pr,
                    eta_cal,
562                                                   fill_value='
                                                      extrapolate
                                                      ')
563 
564         Responsivity_data = {}
565 
566         for index, filmname in enumerate(self.FilmNames):
567             FileName = [file for file in ListFileNames if
                    filmname in file][0]
568             FileName = self.Resp_dir + FileName
569 
570             Responsivity_data[filmname] = {}
571             if self.ThicknessCalibrated[filmname]:
572                 lam_data, R_data = np.loadtxt(FileName,
                        delimiter=',',
573                                               usecols=(0,5), skiprows=1,
                                                  unpack=True)
```

```
574                 Responsivity_data[filmname] = {'lam': lam_data,
                        'R': R_data}
575             else:
576                 lam_data, Iref_data, Isamp_data = np.loadtxt(
                        FileName, unpack=True,
577                                     delimiter=',', usecols=(0,1,4),
                                            skiprows=1)
578
579                 Pref = Iref_data/Pr_Calibration(lam_data)
580                 Psamp = Pref*PsPr_Calibration(lam_data)
581                 R = Isamp_data / Psamp
582                 Responsivity_data[filmname] = {'lam': lam_data,
                        'R': R}
583
584         return Responsivity_data
585
586     def PlotAllResponsivity(self):
587         Responsivity_data = self.LoadRespDataFromFiles()
588
589         pf.init_plotting()
590         plt.figure()
591         plt.legend(self.FilmNames)
592         plt.xlabel('Wavelength (nm)')
593         plt.ylabel('Responsivity (A/W)')
594
595         for index, filmname in enumerate(self.FilmNames):
596             plt.semilogy(Responsivity_data[filmname]['lam'],
597                          Responsivity_data[filmname]['R'], color
                                =colors[index],
598                          marker='o', lw=0)
599
600         return
601
602     def Calculate_Sqrt_IQE(self):
603
604
605         ## A/W = (C/s)/(J/s) = C/J
606         ## To convert from A/W to response per photon:
607         ## A/W*(E_photon / # of photons) = [C/J]*[J/photons] = C
                /photon
608         ## [C/photon]*[electron/C] = electrons / photon
609
610         hc = (1.23984193)*1e3 # [eV*nm]
611
612         def photon_energy(lam):
613
614             ## Calculates the photon energy given wavelength.
```

```
615
616             return (hc/lam)
617
618         def FowlerDist(lam, R, A):
619
620             ## Calculates the Fowler distribution: Sqrt(charge/
                    absorbed photon)
621
622             return np.sqrt((photon_energy(lam)**2)*(R/A))
623
624         Responsivity_data = self.LoadRespDataFromFiles()
625         Absorption_Extract = Absorption_Analysis(self.MetalName,
                self.ThicknessDict)
626         Absorption = Absorption_Extract.ProcessAndInterpolate()[
                'Interpolated']
627
628         Sqrt_EphIQE = {}     # Square root of IQE a.k.a. Fowler
                Distribution
629
630         for filmname in self.FilmNames:
631             Sqrt_EphIQE[filmname] = {}
632             if self.MetalName == 'PureAg':
633                 ATR = Calculate_ATR_FromEllipsometry(self.
                        MetalName,
634                                                      self.ThicknessDict,
                                                            Responsivity_data[filmname]['lam'
                                                            ])
635                 A = ATR['A'][filmname]
636             else:
637                 R = Absorption[filmname]['R'](Responsivity_data[
                        filmname]['lam'])
638                 T = Absorption[filmname]['T'](Responsivity_data[
                        filmname]['lam'])
639                 A = 1-R-T
640             Sqrt_EphIQE[filmname]['Eph'] = photon_energy(
                    Responsivity_data[filmname]['lam'])
641             Sqrt_EphIQE[filmname]['SqR'] = FowlerDist(
                    Responsivity_data[filmname]['lam'],
642                  Responsivity_data[filmname]['R'], A)
643
644         return Sqrt_EphIQE
645
646     def PlotSqrtIQE(self):
647
648         Sqrt_IQE = self.Calculate_Sqrt_IQE()
649
650         pf.init_plotting()
```

```
651             plt.figure()
652             plt.xlabel('Photon energy (eV)')
653             plt.ylabel('Sqrt(IQE)')
654             plt.xlim([0.83, 1.0])
655 
656             for index, filmname in enumerate(self.FilmNames):
657                 plt.plot(Sqrt_IQE[filmname]['Eph'], Sqrt_IQE[
                        filmname]['SqR'],
658                          color=colors[index], marker='o', lw=0)
659 
660             return
661 
662         def Fowler_Fit(self):
663 
664             Sqrt_IQE = self.Calculate_Sqrt_IQE()
665 
666             def line_eq(Ep, m, phiB):
667                 return m*Ep + phiB
668 
669             def find_barrier_height(Eph, SqR):
670 
671                 ## Fit a line to the linear region of the Fowler
                        distribution and solve
672                 ## for the barrier height (aka the x intercept).
673 
674 
675                 # Linear fit region
676                 Fit_Region = np.logical_and(Eph > 0.85, Eph < 0.98)
677                 Eph_fit = Eph[Fit_Region]
678                 SqR_fit = SqR[Fit_Region]
679 
680                 # Fit data
681                 fitvals, err = opt.curve_fit(line_eq, Eph_fit,
                        SqR_fit)
682 
683                 phiB_calc = -fitvals[1]/fitvals[0]
684 
685                 return phiB_calc, fitvals
686 
687             Fowler_Fit_Vals = {'PhiB': {}, 'FitValues': {}}
688 
689             for index, filmname in enumerate(self.FilmNames):
690                 phib, fitvals = find_barrier_height(Sqrt_IQE[
                        filmname]['Eph'],
691                                                     Sqrt_IQE[filmname]['
                                                        SqR'])
692                 Fowler_Fit_Vals['PhiB'][filmname] = phib
```

```
693             Fowler_Fit_Vals['FitValues'][filmname] = fitvals
694
695         return Fowler_Fit_Vals
696
697
698     def PlotAllFowlerFit(self):
699
700         Sqrt_IQE = self.Calculate_Sqrt_IQE()
701         FowlerFitValues = self.Fowler_Fit()
702
703         plt.figure(figsize=(4,6))
704         plt.xlim([0.8, 1.0])
705         plt.ylim([0.00, 0.08])
706         plt.xlabel('Photon energy (eV)')
707         plt.ylabel('Sqrt(IQE)')
708
709         def line_eq(Ep, m, phiB):
710             return m*Ep + phiB
711
712         Eph_fit_list = np.linspace(0.1, 1.0, 100)
713
714         for index, filmname in enumerate(self.FilmNames):
715             plt.plot(Sqrt_IQE[filmname]['Eph'],
716                      Sqrt_IQE[filmname]['SqR'], color=colors[
                             index],
717                      marker='o', lw=0)
718             plt.plot(Eph_fit_list, line_eq(Eph_fit_list,
719                        *FowlerFitValues['FitValues'][filmname]),
                               'k', lw=2)
720
721         return
722
723     def Extract_R_v_Th(self, Eph_select):
724
725         FowlerFitValues = self.Fowler_Fit()
726
727         def line_eq(Ep, m, phiB):
728             return m*Ep + phiB
729
730         phiB_avg = np.average(list(FowlerFitValues['PhiB'].
                values()))
731
732         R_v_T = {}
733         for filmname in self.FilmNames:
734             R_v_T[filmname] = (1/Eph_select)*(line_eq(Eph_select
                    ,
735                      FowlerFitValues['FitValues'][filmname][0],
```

```
736                 -FowlerFitValues['FitValues'][filmname][0]*
                        phiB_avg))**2.0
737
738         return R_v_T
739
740     def Plot_R_v_Th(self, Eph_select):
741
742         R_v_T = self.Extract_R_v_Th(Eph_select)
743
744         pf.init_plotting()
745         plt.figure()
746         plt.xlabel('Metal thickness (nm)')
747         plt.ylabel('IQE')
748
749         for index, filmname in enumerate(self.FilmNames):
750             plt.semilogy(self.ThicknessDict[filmname], R_v_T[
                    filmname],
751                          color=colors[index], marker='o', lw=0)
752
753         return
754
755     def Extract_Attenuation_Length_Linear(self, Eph_select,
            printVal=False):
756
757         R_v_T = self.Extract_R_v_Th(Eph_select)
758
759         R_fit = np.array([])
760         th_fit = np.array([])
761         for filmname in self.FilmNames:
762             R_fit = np.append(R_fit, R_v_T[filmname])
763             th_fit = np.append(th_fit, self.ThicknessDict[
                    filmname])
764
765         def logR_fit(t, m, b):
766             return m*t + b
767
768         fitlR1, errlR1 = opt.curve_fit(logR_fit, th_fit, np.log(
                R_fit))
769
770         Atten_Length = {}
771
772         perr = np.sqrt(np.diag(errlR1))
773         Atten_Length['L'] = -1/fitlR1[0]
774         Atten_Length['Error'] = Atten_Length['L']*perr[0]/np.abs
                (fitlR1[0])
775         Atten_Length['FitValues'] = fitlR1
776
```

```
777         if printVal:
778             print('Attenuation Length: '+str(Atten_Length['L']))
779             print('Attenuation Length Error: '+str(Atten_Length[
                    'Error']))
780 
781         return Atten_Length
782 
783 
784     def Plot_R_v_Th_LinearFit(self, Eph_select):
785 
786         R_v_T = self.Extract_R_v_Th(Eph_select)
787         Atten_Length = self.Extract_Attenuation_Length_Linear(
                Eph_select)
788         thicknesses = self.ThicknessDict.values()
789 
790         def logR_fit(t, m, b):
791             return m*t + b
792 
793         thfit = np.linspace(min(thicknesses)-5, max(thicknesses)
                +5,100)
794 
795         pf.init_plotting()
796         plt.figure()
797         plt.ylabel('IQE')
798         plt.xlabel('Metal thickness (nm)')
799 
800         plt.semilogy(thfit, np.exp(logR_fit(thfit, *Atten_Length
                ['FitValues'])),
801                      'k', lw = 2)
802 
803         for index, filmname in enumerate(self.FilmNames):
804             plt.semilogy(self.ThicknessDict[filmname], R_v_T[
                    filmname],
805                          color=colors[index], marker='o', lw=0)
806 
807         return
```

Bibliography

[1] A. A. Huurdeman, in *The Worldwide History of Telecommunications* (John Wiley & Sons, Inc., Hoboken, NJ, USA, 2003) Chap. Optical Fiber Transmission, pp. 445–479.

[2] S. E. Miller, Bell System Technical Journal **48**, 2059 (1969).

[3] F. Shepherd and A. Yang, in *1973 International Electron Devices Meeting* (IEEE, 1973) pp. 310–313.

[4] A. Rogalski, *Infrared Detectors*, 2nd ed. (Taylor & Francis Group, 2011).

[5] J. Cohen, J. Vilms, and R. J. Archer, *Investigation of semiconductor Schottky arriers for Optical Detection and Cathodic Emission*, Tech. Rep. (Hewlett-Packard Laboratories, Palo Alto, CA, 1968).

[6] R. H. Fowler, Physical Review **38**, 45 (1931).

[7] V. L. Dalal, Journal of Applied Physics **42**, 2274 (1971).

[8] M. W. Knight, H. Sobhani, P. Nordlander, and N. J. Halas, Science **332**, 702 (2011).

[9] W. Li and J. Valentine, Nano Letters **14**, 3510 (2014).

[10] V. E. Vickers, Applied Optics **10**, 2190 (1971).

[11] C. Scales and P. Berini, IEEE Journal of Quantum Electronics **46**, 633 (2010).

[12] W. F. Kosonocky, Proceedings of SPIE **1308**, 2 (1990).

[13] H. Elabd, T. Villani, and W. Ko, IEEE Electron Device Letters **3**, 89 (1982).

[14] H. Kocer, S. Butun, Z. Li, and K. Aydin, Scientific Reports **5**, 8157 (2015).

[15] V. Giannini, A. I. Fernandez-Dominguez, S. C. Heck, and S. A. Maier, Chemical Reviews **111**, 3888 (2011).

[16] M. Tanzid, A. Ahmadivand, R. Zhang, B. Cerjan, A. Sobhani, S. Yazdi, P. Nordlander, and N. J. Halas, ACS Photonics **5**, 3472 (2018).

[17] S. A. Maier, *Plasmonics: Fundamentals and Applications* (2007).

[18] T. Gong, L. Krayer, and J. N. Munday, Journal of Photonics for Energy **6**, 042510 (2016).

[19] M. A. Kats, R. Blanchard, P. Genevet, and F. Capasso, Nature Materials **12**, 20 (2013).

[20] R. Soref, Nature Photonics **4**, 495 (2010).

[21] M. Asghari and A. V. Krishnamoorthy, Nature Photonics **5**, 268 (2011).

[22] G. T. Reed, G. Mashanovich, F. Y. Gardes, and D. J. Thomson, Nature Photonics **4**, 518 (2010).

[23] D. Liang and J. E. Bowers, Nature Photonics **4**, 511 (2010).

[24] J. Michel, J. Liu, and L. C. Kimerling, Nature Photonics **4**, 527 (2010).

[25] Y. Kang, H.-D. Liu, M. Morse, M. J. Paniccia, M. Zadka, S. Litski, G. Sarid, A. Pauchard, Y.-H. Kuo, H.-W. Chen, W. S. Zaoui, J. E. Bowers, A. Beling, D. C. Mcintosh, X. Zheng, and J. C. Campbell, Nature Photonics **3**, 59 (2008).

[26] N. Ye, M. R. Gleeson, M. U. Sadiq, B. Roycroft, C. Robert, H. Yang, H. Zhang, P. E. Morrissey, N. Mac Suibhne, K. Thomas, A. Gocalinska, E. Pelucchi, R. Phelan, B. Kelly, J. OCarroll, F. H. Peters, F. C. Garcia Gunning, and B. Corbett, Journal of Lightwave Technology **33**, 971 (2015).

[27] S. Wirths, R. Geiger, N. Von Den Driesch, G. Mussler, T. Stoica, S. Mantl, Z. Ikonic, M. Luysberg, S. Chiussi, J. M. Hartmann, H. Sigg, J. Faist, D. Buca, and D. Grützmacher, Nature Photonics **9**, 88 (2015).

[28] H. S. Mączko, R. Kudrawiec, and M. Gladysiewicz, Scientific Reports **6**, 34082 (2016).

[29] J. J. Ackert, D. J. Thomson, L. Shen, A. C. Peacock, P. E. Jessop, G. T. Reed, G. Z. Mashanovich, and A. P. Knights, Nature Photonics **9**, 393 (2015).

[30] R. R. Grote, K. Padmaraju, B. Souhan, J. B. Driscoll, K. Bergman, and R. M. Osgood Jr., IEEE Photonics Technology Letters **25**, 67 (2013).

[31] C. Scales, I. Breukelaar, and P. Berini, Optics Letters **35**, 529 (2010).

[32] C. Chen, B. Nechay, and B.-Y. Tsaur, IEEE Transactions on Electron Devices **38**, 1094 (1991).

[33] C. Hägglund, S. P. Apell, and B. Kasemo, Nano Letters **10**, 3135 (2010).

[34] J. M. Llorens, J. Buencuerpo, and P. A. Postigo, Applied Physics Letters **105**, 231115 (2014).

[35] S. S. Mirshafieyan, H. Guo, and J. Guo, IEEE Photonics Journal **8**, 1 (2016).

[36] H. Song, L. Guo, Z. Liu, K. Liu, X. Zeng, D. Ji, N. Zhang, H. Hu, S. Jiang, and Q. Gan, Advanced Materials **26**, 2737 (2014).

[37] H. Dotan, O. Kfir, E. Sharlin, O. Blank, M. Gross, I. Dumchin, G. Ankonina, and A. Rothschild, Nature Materials **12**, 158 (2012).

[38] E. F. C. Driessen and M. J. A. de Dood, Applied Physics Letters **94**, 171109 (2009).

[39] J. Park, J.-H. Kang, A. P. Vasudev, D. T. Schoen, H. Kim, E. Hasman, and M. L. Brongersma, ACS Photonics **1**, 812 (2014).

[40] E. D. Palik, *Handbook of Optical Constants of Solids, I-III* (Elsevier Inc, Amsterdam, 1998).

[41] J. H. Weaver, E. Colavita, D. W. Lynch, and R. Rosei, Physical Review B **19**, 3850 (1979).

[42] V. P. Zhukov, E. V. Chulkov, and P. M. Echenique, Physical Review B **73**, 125105 (2006).

[43] P. Dey, W. Weber, K. Inomata, N. Ikeda, N. Tezuka, F. Offi, S. Iacobucci, L. Petaccia, P. D. Johnson, M. S. Altman, M. Yasuda, K. Tamura, H. Kawata, R. Zdyb, and E. Bauer, J. Phys.: Condens. Matter **25**, 272201 (2013).

[44] Z.-J. Ding and R. Shimizu, Scanning **18**, 92 (1996).

[45] W. Mönch, Surface Science **21**, 443 (1970).

[46] B. Y. Zheng, H. Zhao, A. Manjavacas, M. McClain, P. Nordlander, and N. J. Halas, Nature Communications **6**, 7797 (2015).

[47] M. Casalino, G. Coppola, M. Gioffre, M. Iodice, L. Moretti, I. Rendina, and L. Sirleto, Journal of Lightwave Technology **28**, 3266 (2010).

[48] C. Gong and M. S. Leite, ACS Photonics **3**, 507 (2016).

[49] T. Gong and J. N. Munday, Optical Materials Express , 2501,.

[50] K. Luke, Y. Okawachi, M. R. E. Lamont, A. L. Gaeta, and M. Lipson, Optics Letters **40**, 4823 (2015).

[51] F. Wang and N. A. Melosh, Nano Letters **11**, 5426 (2011).

[52] T. Gong and J. N. Munday, Nano Letters **15**, 147 (2015).

[53] T. Gong and J. N. Munday, Applied Physics Letters **110** (2017), 10.1063/1.4973814.

[54] K.-H. Kim and Q.-H. Park, Scientific Reports **3**, 1062 (2013).

[55] H. Macleod, *Thin-Film Optical Filters*, 3rd ed., Vol. 20010719 (Taylor & Francis Group, 2001).

[56] Y.-J. Jen, C.-C. Lee, K.-H. Lu, C.-Y. Jheng, and Y.-J. Chen, Optics Express **23**, 33008 (2015).

[57] C. Pinheiro, J. Rocha, L. Goncalves, S. Lanceros-Mendez, and G. Minas, in *2006 IEEE International Symposium on Industrial Electronics*, Vol. 4 (IEEE, 2006) pp. 2778–2783.

[58] L. A. Weinstein, W.-C. Hsu, S. Yerci, S. V. Boriskina, and G. Chen, Journal of Optics **17**, 55901 (2015).

[59] S. W. Corzine, R. S. Geels, J. W. Scott, R. Yan, and L. A. Coldren, IEEE Journal of Quantum Electronics **25**, 1513 (1989).

[60] Y. O. Barmenkov, D. Zalvidea, S. Torres-Peiró, J. L. Cruz, and M. V. Andrés, Optics Express **14**, 6394 (2006).

[61] Y. Yamamoto, IEEE Journal of Quantum Electronics **16**, 1047 (1980).

[62] M. A. Kats, D. Sharma, J. Lin, P. Genevet, R. Blanchard, Z. Yang, M. M. Qazilbash, D. N. Basov, S. Ramanathan, and F. Capasso, Applied Physics Letters **101**, 221101 (2012).

[63] S. S. Mirshafieyan and J. Guo, Optics Express **22**, 31545 (2014).

[64] J. Park, S. J. Kim, and M. L. Brongersma, Optics Letters **40**, 1960 (2015).

[65] J. Rensberg, Y. Zhou, S. Richter, C. Wan, S. Zhang, P. Schöppe, R. Schmidt-Grund, S. Ramanathan, F. Capasso, M. A. Kats, and C. Ronning, Physical Review Applied **8**, 014009 (2017).

[66] M. R. S. Dias, C. Gong, Z. A. Benson, and M. S. Leite, Advanced Optical Materials **6**, 1700830 (2018).

[67] E. F. C. Driessen, F. R. Braakman, E. M. Reiger, S. N. Dorenbos, V. Zwiller, and M. J. A. de Dood, The European Physical Journal Applied Physics **47**, 10701 (2009).

[68] C. Hilsum, Journal of the Optical Society of America **44**, 188 (1954).

[69] P. B. Johnson and R. W. Christy, Physical Review B **6**, 4370 (1972).

[70] A. Ciesielski, L. Skowronski, W. Pacuski, and T. Szoplik, Materials Science in Semiconductor Processing **81**, 64 (2018).

[71] M. A. Green, Solar Energy Materials and Solar Cells **92**, 1305 (2008).

[72] A. D. Rakić, Applied Optics **34**, 4755 (1995).

[73] A. Capretti, Y. Wang, N. Engheta, and L. Dal Negro, Optics Letters **40**, 1500 (2015).

[74] C. Chen, Z. Wang, K. Wu, and H. Ye, Science and Technology of Advanced Materials **19**, 174 (2018).

[75] J. Kim, G. V. Naik, A. V. Gavrilenko, K. Dondapati, V. I. Gavrilenko, S. M. Prokes, O. J. Glembocki, V. M. Shalaev, and A. Boltasseva, Physical Review X **3**, 041037 (2013).

[76] J. Kim, G. V. Naik, N. K. Emani, U. Guler, and A. Boltasseva, IEEE Journal of Selected Topics in Quantum Electronics **19**, 4601907 (2013).

[77] J. Kim, A. Dutta, G. V. Naik, A. J. Giles, F. J. Bezares, C. T. Ellis, J. G. Tischler, A. M. Mahmoud, H. Caglayan, O. J. Glembocki, A. V. Kildishev, J. D. Caldwell, A. Boltasseva, and N. Engheta, Optica **3**, 339 (2016).

[78] M. Z. Alam, I. De Leon, and R. W. Boyd, Science **352**, 795 (2016).

[79] Y. Wang, A. C. Overvig, S. Shrestha, R. Zhang, R. Wang, N. Yu, and L. Dal Negro, Optical Materials Express **7**, 2727 (2017).

[80] J. Yoon, M. Zhou, M. A. Badsha, T. Y. Kim, Y. C. Jun, and C. K. Hwangbo, Scientific Reports **5**, 12788 (2015).

[81] W. D. Newman, C. L. Cortes, J. Atkinson, S. Pramanik, R. G. DeCorby, and Z. Jacob, ACS Photonics **2**, 2 (2015).

[82] E. J. R. Vesseur, T. Coenen, H. Caglayan, N. Engheta, and A. Polman, Physical Review Letters **110**, 013902 (2013).

[83] K. J. Palm, J. B. Murray, T. C. Narayan, and J. N. Munday, ACS Photonics **5**, 4677 (2018).

[84] I. Liberal and N. Engheta, Nature Photonics **11**, 149 (2017).

[85] B. Edwards, A. Alù, M. E. Young, M. Silveirinha, and N. Engheta, Physical Review Letters **100**, 033903 (2008).

[86] D. C. Adams, S. Inampudi, T. Ribaudo, D. Slocum, S. Vangala, N. A. Kuhta, W. D. Goodhue, V. A. Podolskiy, and D. Wasserman, Physical Review Letters **107**, 1 (2011).

[87] K. Halterman and S. Feng, Physical Review A **78**, 021805 (2008).

[88] V. C. Nguyen, L. Chen, and K. Halterman, Physical Review Letters **105**, 1 (2010).

[89] C. Argyropoulos, P.-Y. Chen, G. D'Aguanno, N. Engheta, and A. Alù, Physical Review B **85**, 045129 (2012).

[90] D. Traviss, R. Bruck, B. Mills, M. Abb, and O. L. Muskens, Applied Physics Letters **102**, 121112 (2013).

[91] S. Feng and K. Halterman, Physical Review B **86**, 165103 (2012).

[92] S. Vassant, A. Archambault, F. Marquier, F. Pardo, U. Gennser, A. Cavanna, J. L. Pelouard, and J. J. Greffet, Physical Review Letters **109**, 237401 (2012).

[93] A. P. Vasudev, J.-H. Kang, J. Park, X. Liu, and M. L. Brongersma, Optics Express **21**, 26387 (2013).

[94] H. Zhao, Y. Wang, A. Capretti, L. D. Negro, and J. Klamkin, IEEE Journal of Selected Topics in Quantum Electronics **21**, 192 (2015).

[95] Y. C. Jun, J. Reno, T. Ribaudo, E. Shaner, J.-J. Greffet, S. Vassant, F. Marquier, M. Sinclair, and I. Brener, Nano Letters **13**, 5391 (2013).

[96] N. A. Güsken, A. Lauri, Y. Li, T. Matsui, B. Doiron, R. Bower, A. Regoutz, A. Mihai, P. K. Petrov, R. F. Oulton, L. F. Cohen, and S. A. Maier, ACS Photonics **6**, 953 (2019).

[97] M. A. Kats, R. Blanchard, S. Ramanathan, and F. Capasso, Optics and Photonics News **25**, 40 (2014).

[98] N. Ahmad, J. Stokes, N. Fox, M. Teng, and M. Cryan, Nano Energy , 777.

[99] M. Born and E. Wolf, *Optics & Laser Technology*, 7th ed. (Cambridge University Press, Cambridge, 1999) pp. 64–67.

[100] G. V. Naik, J. Kim, and A. Boltasseva, Optical Materials Express **1**, 1090 (2011).

[101] S. K. Cheung and N. W. Cheung, Applied Physics Letters **49**, 85 (1986).

[102] S. M. Sze and K. K. Ng, *Physics of Semiconductor Devices*, 3rd ed. (John Wiley & Sons, Inc.; NJ, 2007).

[103] R. Vlutters, O. M. J. van 't Erve, R. Jansen, S. D. Kim, J. C. Lodder, A. Vedyayev, and B. Dieny, Physical Review B **65**, 024416 (2001).

[104] P. Niedermann, L. Quattropani, K. Solt, I. Maggio-Aprile, and O. Fischer, Physical Review B **48**, 8833 (1993).

[105] G. Fischer, H. Hoffmann, and J. Vancea, Physical Review B **22**, 6065 (1980).

[106] J. L. Garrett and J. N. Munday, Nanotechnology **27**, 245705 (2016).

[107] T. Schultz, S. Vogt, P. Schlupp, H. von Wenckstern, N. Koch, and M. Grundmann, Physical Review Applied **9**, 064001 (2018).

[108] P. Tove, S. Hyder, and G. Susila, Solid-State Electronics **16**, 513 (1973).

[109] A. J. Leenheer, P. Narang, N. S. Lewis, and H. A. Atwater, Journal of Applied Physics **115**, 134301 (2014).

[110] A. Tanaka, K. Teramura, S. Hosokawa, H. Kominami, and T. Tanaka, Chemical Science **8**, 2574 (2017).

[111] A. G. Brolo, Nature Photonics **6**, 709 (2012).

[112] J. N. Anker, W. P. Hall, O. Lyandres, N. C. Shah, J. Zhao, and R. P. Van Duyne, Nature Materials **7**, 442 (2008).

[113] S. Lal, S. Link, and N. J. Halas, Nature Photonics **1**, 641 (2007).

[114] R. Sundararaman, P. Narang, A. S. Jermyn, W. A. Goddard III, and H. A. Atwater, Nature Communications **5**, 5788 (2014).

[115] M. Valenti, A. Venugopal, D. Tordera, M. P. Jonsson, G. Biskos, A. Schmidt-Ott, and W. A. Smith, ACS Photonics **4**, 1146 (2017).

[116] P. West, S. Ishii, G. Naik, N. Emani, V. Shalaev, and A. Boltasseva, Laser & Photonics Reviews **4**, 795 (2010), arXiv:arXiv:1108.0993v1 .

[117] L. F. Mondolfo, *Aluminum alloys : structure and properties* (Butterworth & Co Ltd, 1979) p. 986.

[118] M. B. Cortie and A. M. McDonagh, Chemical Reviews **111**, 3713 (2011).

[119] J. P. McClure, J. Boltersdorf, D. R. Baker, T. G. Farinha, N. Dzuricky, C. E. P. Villegas, A. R. Rocha, and M. S. Leite, ACS Applied Materials & Interfaces **11**, 24919 (2019).

[120] C. Gong, M. R. S. Dias, G. C. Wessler, J. A. Taillon, L. G. Salamanca-Riba, and M. S. Leite, Advanced Optical Materials **5**, 1600568 (2017).

[121] S. Link, Z. L. Wang, and M. A. El-Sayed, The Journal of Physical Chemistry B **103**, 3529 (1999).

[122] M. P. Mallin and C. J. Murphy, Nano Letters **2**, 1235 (2002).

[123] J. Rivory, Physical Review B **15**, 3119 (1977).

[124] J. Sinzig, U. Radtke, M. Quinten, and U. Kreibig, Zeitschrift fr Physik D Atoms, Molecules and Clusters **26**, 242 (1993).

[125] D. Rioux, S. Vallières, S. Besner, P. Muñoz, E. Mazur, and M. Meunier, Advanced Optical Materials **2**, 176 (2014).

[126] M. Gaudry, J. Lermé, E. Cottancin, M. Pellarin, J. L. Vialle, M. Broyer, B. Prével, M. Treilleux, and P. Mélinon, Physical Review B **64**, 085407 (2001).

[127] D. I. Yakubovsky, A. V. Arsenin, Y. V. Stebunov, D. Y. Fedyanin, and V. S. Volkov, Optics Express **25**, 25574 (2017).

[128] A. Zunger, S.-H. Wei, L. G. Ferreira, and J. E. Bernard, Physical Review Letters **65**, 353 (1990).

[129] C. Gong, A. Kaplan, Z. A. Benson, D. R. Baker, J. P. McClure, A. R. Rocha, and M. S. Leite, Advanced Optical Materials **6**, 1800218 (2018).

[130] H. B. Michaelson, Journal of Applied Physics **48**, 4729 (1977).

[131] C. Crowell and S. Sze, in *Physics of Thin Films, Volume 4*, edited by G. Hass and R. E. Thun (Academic Press, New York, New York, 1967) pp. 325–371.

[132] C. R. Crowell, W. G. Spitzkr, L. E. Howarth, and E. E. Labate, PHYSICAL REVIEW **127** (1962).

[133] R. W. Soshea and R. C. Lucas, **138** (1965).

[134] L. B. Leder, M. E. Lasser, and D. C. Rudolph, Applied Physics Letters **5**, 215 (1964).

[135] R. Gould and C. Hogarth, International Journal of Electronics **64**, 283 (1988).

[136] M. Bernardi, J. Mustafa, J. B. Neaton, and S. G. Louie, Nature Communications **6**, 7044 (2015).

[137] D. Gall, Journal of Applied Physics **119**, 085101 (2016).

[138] J. J. Quinn, Physical Review **126**, 1453 (1962).

[139] A. van de Walle, P. Tiwary, M. de Jong, D. Olmsted, M. Asta, A. Dick, D. Shin, Y. Wang, L.-Q. Chen, and Z.-K. Liu, Calphad **42**, 13 (2013).

[140] J. M. Soler, E. Artacho, J. D. Gale, A. García, J. Junquera, P. Ordejón, and D. Sánchez-Portal, Journal of Physics: Condensed Matter **14**, 2745 (2002).

[141] S. G. Mayo, F. Yndurain, and J. M. Soler, (2018), arXiv:1812.03925 .

[142] M. A. Noginov, L. Gu, J. Livenere, G. Zhu, A. K. Pradhan, R. Mundle, M. Bahoura, Y. A. Barnakov, and V. A. Podolskiy, Applied Physics Letters **99**, 021101 (2011).

[143] D. Krishnamurthy, H. Weiland, A. Barati Farimani, E. Antono, J. Green, and V. Viswanathan, ACS Energy Letters **4**, 187 (2019).

[144] M. C. Downer, R. L. Fork, and C. V. Shank, Journal of the Optical Society of America B **2**, 595 (1985).

[145] M. Domke, S. Rapp, M. Schmidt, and H. P. Huber, Optics Express **20**, 10330 (2012).

[146] M. C. Fischer, J. W. Wilson, F. E. Robles, and W. S. Warren, Review of Scientific Instruments **87**, 031101 (2016).

[147] R. P. Lu, B. A. Morgan, K. L. Kavanagh, C. J. Powell, P. J. Chen, F. G. Serpa, and W. F. Egelhoff, Journal of Applied Physics **87**, 5164 (2000).

[148] A. Zaleska and D. Glass, Chemical Communications **55**, 7127 (2019).

[149] T. P. White and K. R. Catchpole, Applied Physics Letters **101**, 073905 (2012).

[150] W. Shockley and H. J. Queisser, Journal of Applied Physics **32**, 510 (1961).